Amorphous $Nb_{0.7}Ge_{0.3}$, a high-κ type-II superconductor with very low pinning, allows for measurements in the flux-flow regime over large parts of the B-T-phase diagram. When a transport current is driven through a narrow wire (width 250 nm) connected to remote voltage probes via a perpendicular channel (length 2 μm) in presence of an external (out-of-plane) magnetic field, the Transversal Flux Transformer Effect can be used to produce a nonlocal voltage drop on the remote contacts caused by vortex motion in the channel. In the simplest picture, the Lorentz force acting on the vortices in the local wire creates a pressure on the vortices in the channel, such that the mutual vortex repulsion can explain the nonlocal vortex motion. However, detailed measurements of nonlocal DC voltage-current characteristics taken across the whole B-T-plane show several new aspects, including abrupt sign reversals of the vortex motion. This can be understood in terms of an interplay between Lorentz force (low currents) and Nernst effect via local electron heating (high currents) for $T \ll T_c$, and between the Lorentz force (low currents) and a force due to the local suppression of the superconducting gap (high currents) for T close to T_c.

Universitätsverlag Regensburg

ISBN 978-3-86845-022-4

gefördert von:

Alumni der physikalischen Fakultät der Universität Regensburg e.V.

Universität Regensburg

Florian Otto

Dissertationsreihe Physik - Band 03

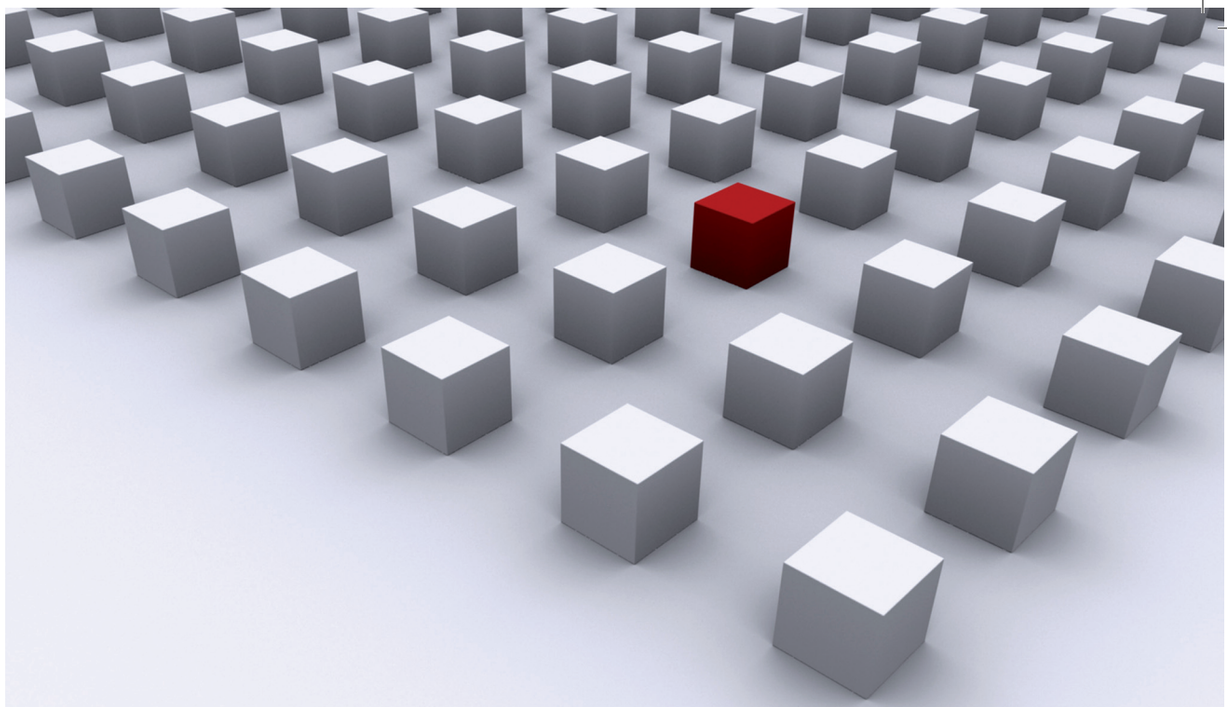

Florian Otto

Nonlinear vortex transport in mesoscopic channels of amorphous NbGe

Universitätsverlag Regensburg

03

Dissertationsreihe Physik

Florian Otto

Nonlinear vortex transport in mesoscopic channels of amorphous NbGe

Nonlinear vortex transport in mesoscopic channels of amorphous NbGe

Dissertation zur Erlangung des Doktorgrades der Naturwissenschaften (Dr. rer. nat.)
der naturwissenschaftlichen Fakultät II - Physik der Universität Regensburg
vorgelegt von

Florian Otto

aus Regensburg
im Jahr 2008

Die Arbeit wurde von Prof. Dr. Ch. Strunk angeleitet.
Das Promotionsgesuch wurde am 3.12.2008 eingereicht.
Das Kolloquium fand am 21.1.2009 statt.

Prüfungsausschuss:	Vorsitzender:	Prof. Dr. Matthias Brack
	1. Gutachter:	Prof. Dr. Christoph Strunk
	2. Gutachter:	Prof. Dr. Rudolf Gross
	weiterer Prüfer:	Prof. Dr. Franz Giessibl

Dissertationsreihe der Fakultät für Physik der Universität Regensburg, Band 3

Herausgegeben vom Präsidium des Alumnivereins der Physikalischen Fakultät:
Klaus Richter, Andreas Schäfer, Werner Wegscheider

Florian Otto

Nonlinear vortex transport in mesoscopic channels of amorphous NbGe

Universitätsverlag Regensburg

Bibliografische Informationen der Deutschen Bibliothek.
Die Deutsche Bibliothek verzeichnet diese Publikation
in der Deutschen Nationalbibliografie. Detailierte bibliografische Daten
sind im Internet über http://dnb.ddb.de abrufbar.

1. Auflage 2009

Leibnitzstraße 13, 93055 Regensburg

Konzeption: Thomas Geiger
Umschlaggestaltung: Franz Stadler, Designcooperative Nittenau eG
Layout: Florian Otto
Druck: Docupoint, Magdeburg
ISBN: 978-3-86845-022-4

Weitere Informationen zum Verlagsprogramm erhalten Sie unter:
www.univerlag-regensburg.de

Nonlinear vortex transport in mesoscopic channels of amorphous NbGe

Dissertation
zur Erlangung des Doktorgrades der Naturwissenschaften
(Dr. rer. nat.)
der naturwissenschaftlichen Fakultät II - Physik
der Universität Regensburg
vorgelegt von
Florian Otto
aus Regensburg

Dezember 2008

Die Arbeit wurde von Prof. Dr. Ch. Strunk angeleitet.
Das Promotionsgesuch wurde am 03.12.2008 eingereicht.
Das Kolloquium fand am 21.01.2009 statt.

Prüfungsausschuss:	Vorsitzender:	Prof. Dr. Matthias Brack
	1. Gutachter:	Prof. Dr. Christoph Strunk
	2. Gutachter:	Prof. Dr. Rudolf Gross
	weiterer Prüfer:	Prof. Dr. Franz Giessibl

Für Susanne

Contents

Chapter 1

Introduction

In 1908, exactly 100 years ago, Heike Kammerlingh-Onnes established the basis for a whole new branch of physics by the successful liquefaction of the last of the noble gases, helium [1]. The extremely low boiling point of 4,2 K opened up the door for a centenary of low temperature research across the world. Only three years later, Kammerlingh-Onnes discovered the sudden drop of resistance to unmeasurably small values of a purified sample of Hg below a certain threshold temperature, which inspired him to coin the term 'superconductivity' to this new phase of matter [2]. Already in 1913, he was awarded the Nobel Prize in Physics for the above achievements. The birth of type-II superconductivity was in 1957, when Abrikosov theoretically predicted this second type of superconductors [3], which allows for flux penetration in the form of single vortices, each carrying a flux quantum $\Phi_0 = h/(2e) = 2.07\,\mathrm{Tm}^2$, due to the negative wall energy associated with such flux-lines. This groundbreaking paper built the basis for huge amounts of both experimental and theoretical works. In 2003, Abrikosov together with Ginzburg and Leggett received the Nobel prize for the development of the Ginzburg-Landau-Abrikosov-Gor'kov (GLAG) theory of the superconducting state.

Type-II superconductors are very important for applications, where their high critical currents allow for the production of large magnetic fields, used for example for magnetic resonance imaging (MRI). While in that case, high pinning is desirable in order to maximize critical currents, fundamental research on unhindered flux flow requires materials with very low pinning.

As will be described in the next chapter, vortex motion is usually caused by the Lorentz force due to an applied transport current in the material. Without pinning, which originates from material inhomogeneities and imperfections, the vortices move perpendicular to the current, which causes an electric field and thus dissipation (=resistance) parallel to the current. This was extensively studied and well confirmed by many experiments already 40 years ago. Giaever showed in 1965 that the magnetic coupling between two superconducting layers (provided by flux lines) separated by an insulating film can cause

dissipation in the secondary film when sending current through the primary one [4]. This flux transformer was one of the first experimental confirmations of the picture of moving flux lines with electrical measurements, but more importantly also the first example of nonlocal vortex motion, i.e. motion in regions where no driving current flows. Subsequently, this idea was reestablished for the case of high-temperature superconductors (HTSC) in the early 90's to clarify the dimensionality of the vortex lines in these materials (see e.g. [5, 6, 7, 8]). Since HTSCs consist of weakly coupled layers, one of the main questions was whether the flux lines would behave as purely two-dimensional pancake vortices or remain coupled fully three-dimensional across the whole sample thickness. The substantially smaller conductivity in the c-direction perpendicular to the layer planes in comparison to the in-plane conductivity leads to a strongly nonuniform current distribution across the sample thickness when e.g. injected into the top layer. The relative strength of vortex-vortex interactions and thermal fluctuations then determines whether or not the conductivity is nonlocal. A nonlocal response perpendicular to the vortices was also predicted theoretically [9] and found experimentally [10] in case of high viscosity of the vortex matter close to the melting transition in HTSC. In absence of a driving current, this effect is expected to die off after a few vortex lattice constants [11].

In 2004, Grigorieva et al. found a different nonlocal effect [11], where vortex motion in a mesoscopic wire made of a conventional, high-κ type-II superconductor, which is connected to remote voltage probes via a perpendicular channel causes dissipation in a region of the superconductor, where basically no transport current flows. In contrast to the above mentioned viscosity-induced dynamical effect, here the nonlocal vortex motion survives over several hundred intervortex spacings in absence of a driving current. This Transversal Flux Transformer Effect is at the heart of this thesis. While previous studies centered around the geometry dependence of the effect, measured via magnetic field sweeps [11, 12, 13], this study is mainly concerned with detailed high-sensitivity DC measurements of the current dependence. Strong nonlinearities are found, hinting at an interplay of Lorentz force and nonequilibrium at high current densities.

This thesis is organized as follows: in chapter 2, an overview of theoretical concepts important for the understanding of the topic is presented. First, basics of the mixed state and the two main theories, Ginzburg-Landau (GL) and Bardeen-Cooper-Schrieffer (BCS), and secondly forces on vortices and the resulting motion are discussed. Then, the more advanced topic of flux-flow resistance and nonequilibrium effects will be described, before the main features of the TFTE are introduced. Finally, the basics of the Berezinskii-Kosterlitz-Thouless transition are presented, which might play an important role regarding special features observed in our measurements immediately below T_c.
The chapters 3, 4 and 5 address the material properties and the sample fabrication,

the measurement setup and the determination of the superconducting parameters via characterization measurements respectively.
The main results are discussed in chapter 6, where both local and nonlocal measurements of detailed high-sensitivity DC measurements of voltage-current characteristics taken across the whole B-T-plane will be presented. This is done in both cases for two well-understood limits, namely temperatures very close and well below the transition temperature T_c. The previously predicted [14] and observed [15, 16] strong nonlinearities in local measurements, called flux-flow instabilites (FFI), provide a starting point for a successful interpretation of the observed features of the TFTE in the nonlocal curves: in the simplest picture, the Lorentz force acting on the vortices in the local wire creates a pressure on the vortices in the channel, such that the mutual vortex repulsion can explain the nonlocal vortex motion. However, several new aspects, including abrupt sign reversals of the vortex motion are observed. This can be understood in terms of an interplay between Lorentz force (low currents) and Nernst effect via local electron heating (high currents) for $T \ll T_c$, and between the Lorentz force (low currents) and a force due to the local suppression of the superconducting gap (high currents) for T close to T_c.
At temperatures immediately below T_c, several independent measurements show an absolute negative resistance in absence of magnetic field, which cannot be easily explained. These results are presented in chapter 7.
Chapter 8 provides an outlook in terms of time-resolved vortex dynamics.

Chapter 2

Overview of the relevant concepts

In this theory chapter, I will prepare the ground for a successful interpretation of my measurements by presenting an overview of the relevant concepts. This will be done without going into the subtle details neither of the microscopic description (BCS-theory) nor the Ginzburg-Landau theory of superconductivity, which would inevitably go beyond the scope of this thesis and can be looked up in numerous standard text books (see e.g. [17,18]). Rather, I would like to remind the reader of some basic concepts of type-II superconductors, vortices and their motion, which are relevant for this investigation (see e.g. [19]).

The first section serves as an introduction to the basic properties of type-II superconductors together with a glimpse at the two main theories, while the remaining sections deal with less well-known properties of vortices: While section 2.2 lists the many different contributions to forces on flux lines, section 2.3 discusses the different regimes of vortex motion. The last two sections summarize previous results of experiments on nonlocal vortex motion in mesoscopic channels of a specific geometry (section 2.4) and basics of the Berezinskii-Kosterlitz-Thouless transition (section 2.5).

2.1 The mixed state

As already mentioned in the introduction, superconductivity manifests itself in two basic and distinct properties, namely lossless conduction and perfect diamagnetism below limiting values of temperature, magnetic field and electrical current respectively. The latter feature is strongly modified in a second category of superconductors, called type-II, where magnetic flux can penetrate the specimen in the form of vortices, each carrying one flux quantum. In this section, I will first describe the basic phenomenology and early modelling, before more profound theories are addressed in following subsections.

2.1.1 Phenomenology and London model

The simplest phase diagram of a superconductor is governed by the observation that superconductivity can (reversibly) be destroyed by either applying critical values of temperature, magnetic field or electric current to the material. Slightly more detailed information on the behavior of type-II superconductors is contained in the B-T phase plane shown in figure 2.1 (left). For magnetic fields smaller than the lower critical field $B_{c1}(T)$ the response is still perfectly diamagnetic, expelling any external field from the interior of the material apart from a small surface layer. Between the lower critical field $B_{c1}(T)$ and the upper critical field $B_{c2}(T)$, flux can penetrate in the form of flux lines or vortices, created by circular screening currents within the material which bundle the magnetic field lines. Also indicated is the thermodynamic critical field $B_{c,\,th}(T)$ between the other two critical fields, associated with the condensation energy (this will be dealt with in the section on the Ginzburg-Landau-theory).

A cross-section through a flux line structure is shown in figure 2.2: a circular screening current j_s around the core allows for penetration of the magnetic field B on the length scale of λ, whereas the Cooper-pair density n_s (see next sections) drops rather sharply from the bulk value to zero at the core center. Due to the repulsive interaction between two neighboring circular currents, the vortices usually arrange themselves in a hexagonal lattice shown on the right side of the same figure. The actual lattice spacing can be adjusted by an external magnetic field $B = |\vec{B}|$:

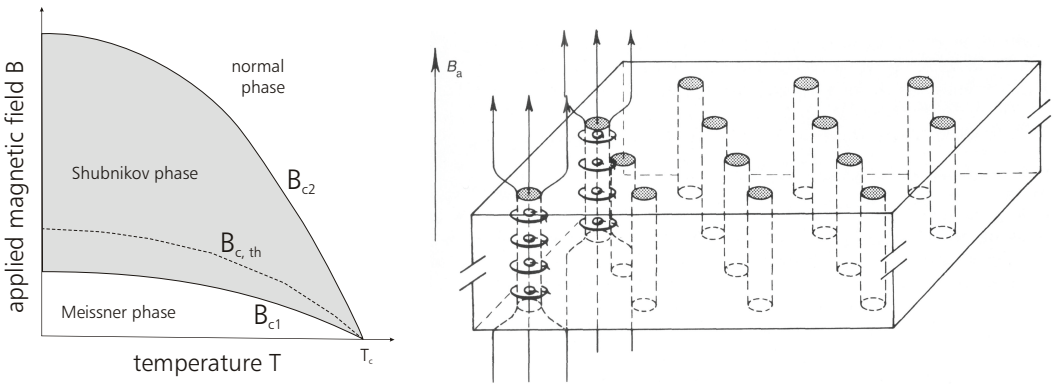

Figure 2.1: (Left) Simple B-T phase diagram of a type-II superconductor, showing the Meissner phase below $B_{c1}(T)$ and the Shubnikov phase for $B_{c1}(T) < B < B_{c2}(T)$. (Right) Schematic of the Shubnikov phase, where flux lines created by circular supercurrents allow for partial flux penetration (source [18]).

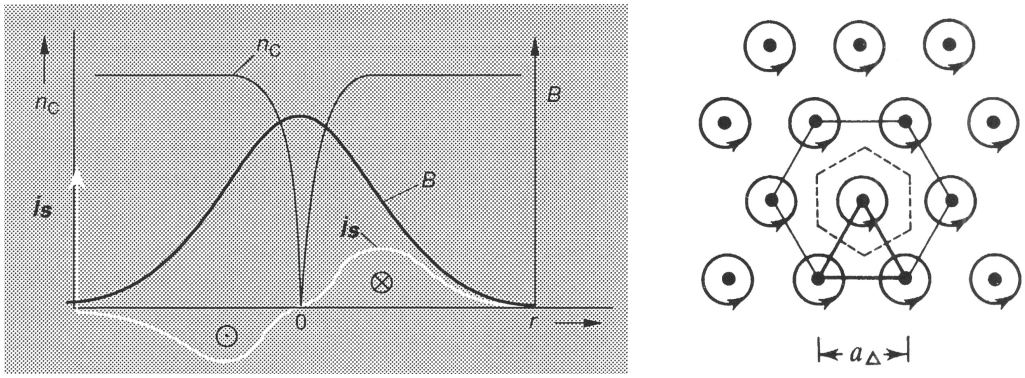

Figure 2.2: (Left) Cross-section through a vortex, showing the Cooper-pair density n_c, the supercurrent density j_s and the magnetic field B (source [18]). (Right) Hexagonal vortex lattice with spacing a_Δ (source [17]).

$$a_\Delta = \left(\frac{4}{3}\right)^{1/4} \sqrt{\frac{\Phi_0}{B}} \quad , \tag{2.1}$$

i.e. the vortex density grows as the field increases.

The two basic electrodynamic properties, namely perfect conductivity and ideal diamagnetism, found a first successful description in 1935 by the London brothers [20] with the following two equations:

$$\vec{E} = \mu_0 \lambda_L^2 \dot{\vec{j}_s} \tag{2.2}$$

$$\vec{B} = -\mu_0 \lambda_L^2 \vec{\nabla} \times \vec{j_s} \quad , \tag{2.3}$$

where $\lambda_L = \sqrt{m/(\mu_0 q^2 n_s)}$ is the London penetration depth, $\mu_0 = 4\pi \cdot 10^{-7}\,\mathrm{Vs/(Am)}$ and q, m and n_s are the charge, the mass and the density of superconducting electrons respectively. According to the first London equation, a stationary supercurrent j_s generates no electric field and thus no dissipation, whereas a finite electric field accelerates the superconducting electrons in contrast to Ohm's law in a normal metal. The second London equation can be combined with the Maxwell equation $\vec{\nabla} \times \vec{B} = \mu_0 \vec{j_s}$ to yield

$$\vec{\nabla}^2 \vec{B} = \frac{1}{\lambda^2} \vec{B} \quad , \tag{2.4}$$

since $-\vec{\nabla} \times (\vec{\nabla} \times \vec{B}) = -\vec{\nabla}(\vec{\nabla} \cdot \vec{B}) + \vec{\nabla}^2 \vec{B}$ and $\vec{\nabla} \cdot \vec{B} = 0$. This quite obviously implies an exponential screening of magnetic field within a superconductor (consider for example

a superconductor filling the positive half-space) and justifies the use of λ as a penetration depth. Empirically, it is found that

$$\lambda(T) \approx \frac{\lambda(0)}{\sqrt{1-(T/T_c)^4}} \quad . \tag{2.5}$$

In view of the definition of λ_L above, this implies that n_s vanishes at T_c like $(1-t^4)$, where $t = T/T_c$ is often used as the so-called *reduced temperature*. This phenomenological formula stems from a two-fluid model by Gorter and Casimir [21], assuming coexistence of normal and superconducting "fluids". The experimental finding that measured values of $\lambda(T)$ remained always larger than $\lambda(0)$ even after extrapolation to $T = 0$ inspired Pippard to introduce a characteristic length scale ξ_0 associated with his nonlocal generalization of the London model [22]. He argued that only electrons within $\sim k_B T_c$ of the Fermi energy can take part in a phenomenon which sets in at T_c, and with these having a momentum of $\sim k_B T_c/v_f$ (where v_f is the Fermi velocity), the uncertainty principle provides a good estimate of this length scale via

$$\xi_0 \approx \Delta x \geq \hbar/\Delta p \approx \hbar v_f/k_B T_c \quad . \tag{2.6}$$

Apart from a numerical prefactor determined by fitting experimental data (see [17] and original literature for more details on both of the above quoted theories), this concept in a way already anticipated parts of the results from the microscopic BCS-theory. In presence of scattering, the "pure" coherence length ξ_0 was assumed to be replaced by ξ defined as

$$\frac{1}{\xi} = \frac{1}{\xi_0} + \frac{1}{\ell} \quad , \tag{2.7}$$

where ℓ is the mean free path.

In thin films, the penetration depth is modified according to

$$\lambda_{eff} \approx \lambda_L \left(\frac{\xi_0'}{d}\right)^{1/2} \tag{2.8}$$

in parallel magnetic field (where ξ_0' is a modified Pippard coherence length, see Tinkham [17] for details), and according to

$$\lambda_\perp \approx \lambda_{eff}^2/d \tag{2.9}$$

in perpendicular magnetic field. The latter applies to our case of thin a-NbGe films, and the consequence is rather dramatic: Instead of the bulk value of roughly $800\,\mathrm{nm}$, the effective penetration depth $\lambda_\perp$ due to the film thickness of roughly $40\,\mathrm{nm}$ is enlarged

to values on the order of $16 - 20\,\mu\mathrm{m}$, which is a factor of 10 larger than usual lateral sample dimensions. This implies that the magnetic field penetration is more or less spatially uniform over the entire structure as soon as vortices enter the sample at finite fields (since also $B_{c1} \ll B_{c2}$), so that the vortices can be regarded as well-separated, single entities only electrically, i.e. with respect to their finite core size (which is on the order of $\xi \approx 10\,\mathrm{nm}$).

Fluxoid quantization

Another important, macroscopic feature of superconductivity is the quantization of the *fluxoid* Φ', defined by F. London as follows:

$$\Phi' = \Phi + \mu_0 \lambda_L^2 \oint \vec{j_s} \mathrm{d}\vec{r} = \oint \vec{A} \mathrm{d}\vec{r} + \mu_0 \lambda_L^2 \oint \vec{j_s} \mathrm{d}\vec{r} \quad . \tag{2.10}$$

Considering a multiply connected superconductor, i.e. in the simplest case a superconducting ring, this means that Φ' contains both contributions, the ordinary flux Φ through the integration circuit (where $\vec{A}$ is the vector potential) and the contribution from the screening currents in the superconductor. Recalling that the canonical momentum for charged particles is given by $\vec{p} = m\vec{v} + q\vec{A}$ and the definition of λ_L, plus using $\vec{j_s} = q n_s \vec{v}_s$, we can rewrite eq. 2.10 to apply the semi-classical Bohr-Sommerfeld quantum condition:

$$\begin{aligned} \Phi' &= \oint \vec{A} \mathrm{d}\vec{r} + \oint \left(\mu_0 \frac{m}{\mu_0 q^2 n_s} q n_s \vec{v}_s \right) \mathrm{d}\vec{r} \\ &= \oint \left(\vec{A} + \frac{m}{q} \vec{v} \right) \mathrm{d}\vec{r} = \frac{1}{q} \oint \left(q\vec{A} + m\vec{v} \right) \mathrm{d}\vec{r} \\ &= \frac{1}{q} \oint \vec{p} \mathrm{d}\vec{r} = n \frac{h}{q} \quad . \end{aligned} \tag{2.11}$$

This together with the experimental observation that the flux quantum is given by $\Phi_0 = h/(2e)$ is a first indication that superconductivity is produced by charged carriers of $|q| = 2e$, i.e. Cooper pairs.

While for thick superconducting rings, the path of integration can be chosen such that the second term in eq. 2.10 is zero (since the screening currents only flow in a thin surface layer), and the above simply yields quantization of the magnetic flux itself [1], the situation of a thin ring (where $j_s \neq 0$ along the path of integration) actually really implies that it is the *fluxoid* rather than the flux which is quantized. This was demonstrated experimentally for the first time in 1962 by Little and Parks [25].

[1] shown experimentally in 1961 by two groups independently [23, 24]

2.1.2 Ginzburg-Landau theory

Even after the huge success of the microscopic theory by Bardeen, Cooper and Schrieffer (BCS), the Ginzburg-Landau (GL) theory still provides a useful first step towards understanding a given problem involving superconductivity, and is actually particularly suited for dealing with spatially inhomogeneous situations such as vortices in type-II superconductors. The theory was introduced in 1950 some years before BCS and is based on Landau's general theory of second-order phase transitions, which introduced the important concept of an order parameter. This quantity can have different dimensions, depending on the system whose transition is considered, and in the case of superconductivity plays the role of a complex, macroscopic pseudo-wavefunction $\Psi(\vec{r}) = |\Psi(\vec{r})|e^{i\phi}$. As such, it already contains one important ingredient of superconductivity, namely a well-defined macroscopic phase ϕ. The connection to the charge carriers is given by $|\Psi(\vec{r})|^2 = n_s(\vec{r})$, where $n_s(\vec{r})$ is the local density of superconducting electrons. Due to its phenomenological basis, the GL-theory was not as well respected as it would have deserved it, until Gor'kov [26] could show in 1959 that it could be derived from the BCS-theory in the limiting case of T close to T_c and not too rapidly varying Ψ and $\vec{A}$. One of the biggest successes of the GL-theory was the prediction of the vortex mixed state by Abrikosov [3]. The importance of the contributions by Abrikosov and Gor'kov explains also why nowadays, one often speaks of the Ginzburg-Landau-Abrikosov-Gor'kov theory, or GLAG for short.

The idea is that above the critical temperature T_c, the order paramter $\Psi(\vec{r}) = 0$, and that it continuously increases below T_c. For slowly varying $\Psi(\vec{r})$, we can thus expand the free energy density f in a Taylor series of the form

$$f_s = f_n + \alpha(T)|\Psi|^2 + \frac{1}{2}\beta(T)|\Psi|^4 + \frac{1}{2m^*}\left|\left(\frac{\hbar}{i}\vec{\nabla} - q\vec{A}\right)\Psi\right|^2 + \frac{1}{2\mu_0}|\vec{B}_{ext} - \vec{B}_{int}|^2 ... \quad (2.12)$$

Here, f_s and f_n denote the free energy density of the superconducting and normal state respectively; odd powers in Ψ are forbidden since f must be real. The last term describes the energy needed to change the external field $\vec{B}_{ext}$ to the internal value of $\vec{B}_{int}$, and the term involving the vector potential $\vec{A}$ reflects the spatial variations of $\vec{B}_{int}$ and $\Psi(\vec{r})$, for which supercurrents are necessary. If we neglect the latter two for some first considerations, we see that $\beta(T)$ must be positive, since otherwise a large enough value of Ψ would always lead to $f_s - f_n < 0$, i.e. always to the superconducting state (for $|\Psi| \to \infty$). Secondly, for $T < T_c$, $\alpha(T)$ must be negative, to allow for $f_s < f_n$ with $\beta(T) > 0$. For $T > T_c$ on the other hand, $\alpha(T)$ must be positive to yield $f_n < f_s$ with $|\Psi| = 0$ as the energy minimizing solution. This is depicted in figure 2.3, showing also the equilibrium positions of Ψ for both cases.

The coefficients α and β can also be expanded around T_c, where we obtain $\alpha(T) = \alpha(0)(t-1)$, keeping only the leading term, and β can taken to be constant. The minimum for the case $T < T_c$ occurs for $\Psi = -\alpha/\beta = \Psi_\infty$, where the latter is the value of the order parameter infinitely deep inside the bulk material, far from any surface fields or currents. This can be used to recover the condensation energy

$$f_s - f_n = \alpha|\Psi_\infty|^2 + \frac{1}{2}\beta|\Psi_\infty|^4 = -\frac{\alpha^2}{2\beta} = -\frac{1}{2\mu_0}B_{c,th}^2 \quad , \tag{2.13}$$

where $B_{c,th}$ is the thermodynamic critical field. We can now also solve for the coefficients:

$$\alpha = -\frac{1}{\mu_0}\frac{B_{c,th}^2}{n_s} \tag{2.14}$$

$$\text{and} \qquad \beta = \frac{1}{\mu_0}\frac{B_{c,th}^2}{n_s^2} \quad . \tag{2.15}$$

Since eq. 2.12 gives the free energy density, one has to take the volume integral of 2.12 to find the minimum of the overall free energy, and standard variational methods lead to the two famous Ginzburg-Landau equations

$$0 = \frac{1}{2m^*}\left(\frac{\hbar}{i}\vec{\nabla} - q\vec{A}\right)^2\Psi + \alpha\Psi + \beta|\Psi|^2\Psi \tag{2.16}$$

$$j_s = \frac{q\hbar}{2m^*i}\left(\Psi^*\vec{\nabla}\Psi - \Psi\vec{\nabla}\Psi^*\right) - \frac{q^2}{m^*}|\Psi|^2\vec{A} \quad . \tag{2.17}$$

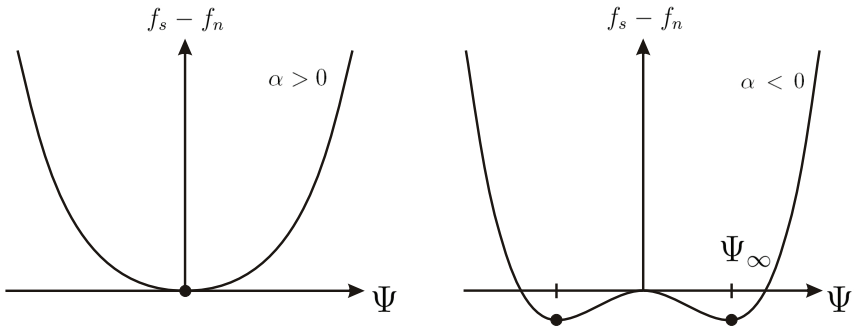

Figure 2.3: Ginzburg-Landau free energy $f_s - f_n$ for $T > T_c$ (implying $\alpha > 0$) and for $T < T_c$ ($\alpha < 0$), with the dots indicating the equilibrium positions / values of Ψ (drawn as in [17]).

This system of differential equations needs to be supplied with appropriate boundary conditions for a given situation. We note that the first of the two equations has the form of a Schrödinger equation apart from the nonlinear term, with energy eigenvalue $-\alpha$. The second one on the other hand looks exactly like a quantum mechanical current. Ginzburg and Landau already pointed out that the particle's mass m^* and charge q would not necessarily need to be identical to those of the electron, and indeed, it was later found from the BCS-theory that $|q| = 2e$ since the electrons are conjugating to form Cooper pairs. Naturally, one would then also take $m^* = 2m_e$ and $n_s = (1/2)n_e$, leaving the London penetration depth unchanged: $m^*/(q^2 n_s) = m_e/(e^2 n_e)$. In reality, the interpretation of the BCS-theory is more complicated in this regard, but we will conclude the discussion at this point for lack of space and relevance.

What is more important are further results of the GL-theory, namely two characteristic length scales. In the case of small magnetic fields, we can use the equilibrium value Ψ_∞ instead of Ψ and take the curl of the second GL equation 2.17 to obtain

$$\vec{\nabla} \times \vec{j_s} = -\frac{q^2}{m^*}|\Psi_\infty|^2 \vec{B} \quad , \tag{2.18}$$

which is equivalent to the second London equation 2.3 upon identification of $|\Psi_\infty|^2 = n_s$, and we recover the London penetration depth

$$\lambda_L = \sqrt{m/(\mu_0 q^2 n_s)} \quad . \tag{2.19}$$

From the BCS-theory, it is found that furthermore

$$\lambda_L(T) = \frac{\lambda_L(0)}{\sqrt{2(1-t)}} \qquad (\text{pure limit}) \quad , \tag{2.20}$$

$$\text{and} \qquad \lambda_L(T) = \frac{\lambda_L(0)}{\sqrt{2(1-t)}} \left(\frac{\xi_0}{1.33\,\ell}\right)^{(1/2)} \qquad (\text{dirty limit}) \quad . \tag{2.21}$$

Now we turn to the first GL equation 2.16, and consider the case without fields. Then we can take Ψ to be real and if we normalize the wavefunction to $f = \Psi/\Psi_\infty$, the one-dimensional equation reads

$$\frac{\hbar^2}{2m^*|\alpha|}\frac{d^2 f}{dx^2} + f - f^3 = 0 \quad . \tag{2.22}$$

This suggests to introduce the characteristic length scale

$$\xi_{GL}(T) = \left(\frac{\hbar^2}{2m^*|\alpha|}\right)^{(1/2)} \propto \frac{1}{\sqrt{1-t}} \tag{2.23}$$

which represents the natural length scale for spatial variations of Ψ, called the GL coherence length. The relation to Pippard's coherence length is found in BCS near T_c, which yields

$$\xi_{GL}(T) = 0.74\frac{\xi_0}{\sqrt{1-t}} \qquad (\text{pure limit}) \quad , \tag{2.24}$$

$$\text{and} \qquad \xi_{GL}(T) = 0.855\frac{\sqrt{\xi_0 \ell}}{\sqrt{1-t}} \qquad (\text{dirty limit}) \quad . \tag{2.25}$$

Finally, it proved very useful to define the famous dimensionless Ginzburg-Landau parameter

$$\kappa = \frac{\lambda_L(T)}{\xi_{GL}(T)} \quad . \tag{2.26}$$

The wall energy associated with a normal-to-superconductor interface changes sign at exactly $\kappa = 1/\sqrt{2}$. This was already shown in the original GL-paper, but nobody realized the significance of the solutions for negative surface energy at high κ until Abrikosov's ground-breaking contribution in 1957, where he predicted type-II superconductors and examined their properties. The most prominent features have already been presented in figure 2.2.
More details about vortices in type-II superconductors will be discussed in the following subsections, but before that, some basics of the microscopic theory will be presented.

2.1.3 Microscopic description: BCS-theory

The basic idea of the BCS-theory [27] is that in presence of an attractive interaction between conduction electrons in a metal, the Fermi sea is unstable against the formation of bound pairs. The origin of this attraction was found to be the polarization of the lattice, i.e. the attraction of the positive ions therein by the negatively charged electrons. If this is strong enough to overcome the repulsive (screened) Coulomb interaction between the electrons, a net attractive interaction and thus a pairing mechanism results.

To further illustrate this concept, let us start by considering the situation of unpaired electrons in a normal metal. In the simplest approximation of free electrons, their energy is given by

$$\epsilon_k = \frac{\hbar}{2m}(k_x^2 + k_y^2 + k_z^2) \quad , \tag{2.27}$$

which depends on the discrete values of the wave vector $\vec{k} = (k_x, k_y, k_z)$. In the ground state, all states within a sphere of radius k_f, the Fermi wave vector, are occupied by

electrons. At higher temperatures, the border between occupied and unoccupied states gets washed out according to the Fermi distribution function

$$f(\epsilon_k) = \frac{1}{e^{(\epsilon_k - \mu)/(k_B T)} + 1} \quad , \tag{2.28}$$

where μ is the chemical potential, which for low temperatures is roughly equal to ϵ_f. Now we introduce an attractive interaction $-V$ for states within $\pm\hbar\omega_c$ of the Fermi energy. Since the attractive interaction was found to be mediated by (virtual) phonons, it makes sense to identify ω_c as a characteristical phonon frequency, namely the Debye frequency ω_D. The result is that electrons with equal and opposite momentum and spin $\{\vec{k}\uparrow, -\vec{k}\downarrow\}$ form Cooper pairs, whose energy is lowered with respect to the energy of two unpaired particles:

$$\epsilon_{pair} \approx 2\epsilon_f - 2\hbar\omega_c e^{-2/N(0)V} \tag{2.29}$$

with $N(0)$ being the density of states at the Fermi level. The BCS ground state is then given by

$$|\Psi_0\rangle = \prod_k \left(u_k |0\rangle_k + v_k |1\rangle_k\right) \quad , \tag{2.30}$$

where $|0\rangle_k$ denotes an unoccupied state with momentum $k = |\vec{k}|$ and $|1\rangle_k$ an occupied one. The respective coefficients or occupation probabilities can be derived by solving the Schrödinger equation and minimizing the energy with respect to u_k and v_k yielding

$$|v_k|^2 = 1 - |u_k|^2 = \frac{1}{2}\left(1 - \frac{\epsilon_k - \epsilon_f}{\sqrt{|\Delta|^2 + (\epsilon_k - \epsilon_f)^2}}\right) \tag{2.31}$$

The parameter Δ is of central importance for the theoretical description of superconductivity, and is given by $\Delta = -V\sum_k u_k v_k$. This pairing potential is in general a complex number $\Delta = \Delta_0 e^{i\phi}$ and depends on all of the paired states. In the normal conducting state, either u_k or v_k are identically zero and thus the pairing potential vanishes.
The two functions are plotted in figure 2.4 for a typical value of $\Delta_0 \approx 1\,\mathrm{meV}$. The probability $|v_k|^2$ of finding an electron with momentum $\vec{k}$ is almost equal to 1 deep inside the Fermi sphere, as it would have been for electrons without interaction. Analogously, for energies far above the Fermi energy, the probability $|u_k|^2 \approx 1$, since this state is unoccupied. A dramatic deviation from normal metals is seen in an interval of roughly $\pm\Delta_0$ around ϵ_f.
The BCS ground state describes particles with identical values of all physical observables, in particular the center-of-mass velocity is the same for all pairs. This is the essence of the macroscopic nature of the quantum state of superconductivity.

The elementary excitations of this system are given by breaking up the Cooper pairs into two independent electrons. These together with the interaction are called quasiparticles, whose (individual) energies are $E_k = \sqrt{(\epsilon_k - \epsilon_f)^2 + \Delta_0^2}$. As a consequence, at least an energy of $2\Delta_0$ needs to be supplied for an excitation, i.e. there is an energy gap of this size around ϵ_f, where no quasiparticles are allowed. The density of states of the quasiparticles in the superconductor for energies $|E_k - \epsilon_f| \geq \Delta_0$ is given by

$$N_s(E_k) = N_n(\epsilon_f) \cdot \frac{|E_k - \epsilon_f|}{\sqrt{(E_k - \epsilon_f)^2 - \Delta_0^2}} \quad , \tag{2.32}$$

with $N_n(\epsilon_f)$ being the density of states of the normal state at the Fermi level. The gap in the density of states can be seen in figure 2.4 (right). It is temperature dependent and monotonically decreases to zero when $T \to T_c$. Since it turns out that $n_s \propto \Delta_0^2$, it is probably not surprising that one can show that the macroscopic wavefunction Ψ is also proportional to Δ.

Let us conclude this chapter by noting some more practically relevant results of the BCS-theory. A connection between the transition temperature and $N_n(\epsilon_f)$, $\hbar\omega_c$ and V is given by

$$T_c = 1.13 \frac{\hbar\omega_c}{k_B} \exp\left(-\frac{1}{N_n(\epsilon_f)V}\right) \quad , \tag{2.33}$$

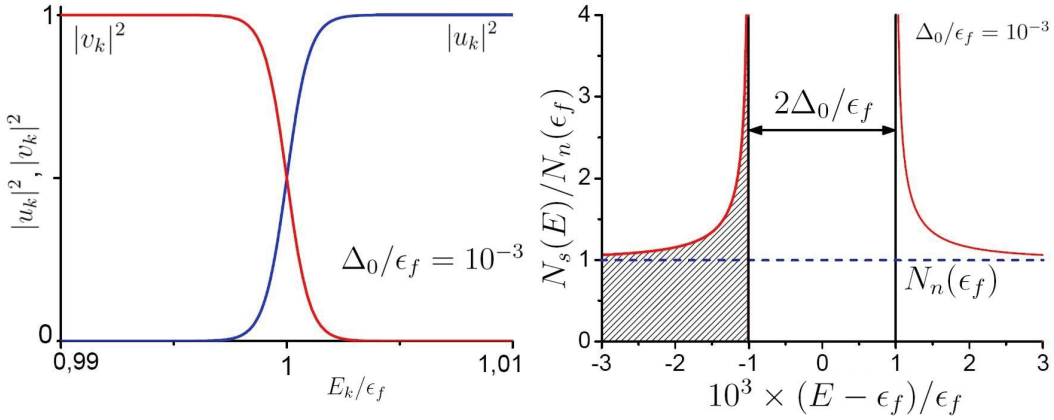

Figure 2.4: (Left) Occupation probabilities plotted as a function of energy (in units of ϵ_f for a ratio of $\Delta_0/\epsilon_f = 10^{-3}$). (Right) Normalized density of states and energy gap of the quasiparticles in the superconductor; at $T = 0$, all states below ϵ_f are occupied (reprinted with kind permission from [28]), drawn as in [18]).

and between the gap at zero temperature and the transition temperature by

$$E_{gap} = 2\Delta_0(T=0) = 3.528\, k_B T_c \quad . \tag{2.34}$$

If again, we use the Debye frequency ω_D as ω_c, eq. 2.33 gives an easy explanation of the isotope effect: heavier atoms have smaller oscillation frequencies and thus T_c is reduced for isotopes with larger masses.
Another useful expression connects the two critical fields according to

$$B_{c1} = B_{c2}\frac{\ln\kappa}{2\kappa^2} \quad , \tag{2.35}$$

implying that for high κ, $B_{c1} \ll B_{c2}$. Several other useful expressions will be presented in section 3.1, when the characteristic parameters for a-NbGe will be extracted from the measurements.

2.2 Forces on flux lines and resulting motion

In this section, I will give a brief summary of the forces that can act on vortices and what the implications for the resulting motion are: An applied driving current leads to a Lorentz force on the flux-lines and thus dissipation, whereas the thermomagnetic effects described in the second subsection are less well-known. The so-called transport entropy associated with vortex motion was discussed and (thought to be) explained already in the early days of flux flow research, but has recently attracted new attention due to a big controversy about its origin [29]. This section closely follows the book by Huebener [19]).

2.2.1 Lorentz force and Josephson relation

Let us consider a flat type-II superconductor in the x-y-plane with magnetic field $\vec{B}$ applied along the z-direction. When a current of sufficient density $\vec{j}_x$ is applied, the flux lines move with velocity $\vec{v}_\Phi$ in a direction given by the Hall angle θ between the y-axis and $\vec{v}_\Phi$ (see figure 2.5).

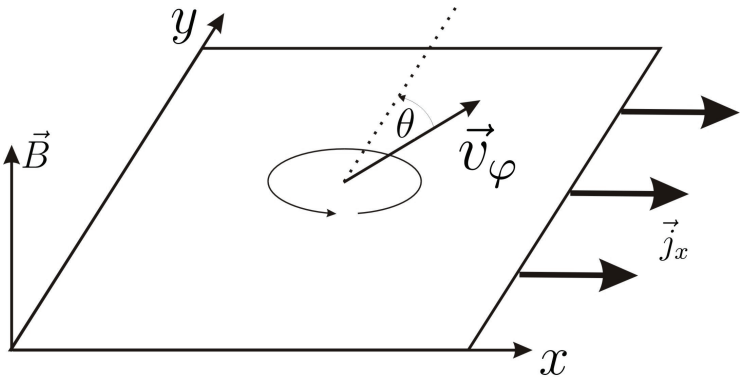

Figure 2.5: Sample geometry for the current-induced motion of vortices

Under stationary conditions, the equation of motion reads

$$\vec{j}_x \times \vec{\Phi}_0 - \epsilon n_s e \vec{v}_\varphi \times \vec{\Phi}_0 - \eta \vec{v}_\varphi - \vec{f}_p = 0 \quad , \tag{2.36}$$

where $\vec{\Phi}_0 = \Phi_0 \cdot \vec{e}_z$, n_s is the density of superconducting electrons, $e = 1.6021 \times 10^{-19}\,\mathrm{As}$, η the vortex motion viscosity and f_p the pinning force. The Lorentz force $\vec{j}_x \times \vec{\Phi}_0$ is thus balanced by the Magnus force $n_s e \vec{v}_\varphi \times \vec{\Phi}_0$, with ϵ being the active fraction of the force, see below, the viscous damping $\eta \vec{v}_\varphi$ and the pinning force f_p, all of which are given per unit length of flux line.

The Lorentz force has the same origin as the usual force between charge carriers in motion and magnetic field in standard electrodynamics and tends to move the vortices perpendicular to applied current and magnetic field. The Magnus force on the other hand is the analog of the hydrodynamic lift force and results in motion perpendicular to the original vortex velocity in absence of pinning and dissipation, i.e. parallel to the applied current. This leads to vortex motion in a direction at an angle θ to the original vortex velocity, see figure 2.5. The resulting Hall voltage due to a finite Hall angle θ was studied in many experiments, but except for very pure substances, the active fraction ϵ of the Magnus force is much smaller than 1. For this reason, we can completely neglect the Magnus force for our purposes, since a-NbGe is a superconductor in the dirty limit ($\ell \ll \xi_0$), and set the Hall angle to zero.
The dissipation mechanisms associated with the motion of vortices are in a sense summarized in the phenomenological parameter η, and different regimes will be discussed in some detail in the next section on flux flow resistance. The main consequence is that the vortex motion causes a time-averaged macroscopic electric field

$$\vec{E} = -\vec{\nabla}U = \vec{B} \times \vec{v}_\varphi \tag{2.37}$$

essentially following Faraday's law. Another point of view would be to make use of the second Josephson relation

$$\frac{\partial \Phi}{\partial t} = \frac{2\pi}{\Phi_0} U \tag{2.38}$$

for the AC Josephson effect. Here, $\Phi = \Phi_2 - \Phi_1$ usually denotes the phase difference between two superconductors 1 and 2 separated by a weak link. In our case, it is the phase difference acquired during the motion of a vortex with velocity $v_\varphi \, \vec{e}_y$ over the whole sample length L, equal to 2π (see e.g. Clem [30]). We thus obtain the induced voltage $U_x = \Phi_0 v_{\Phi,y}/L$, or, at a given vortex density of $n_\phi = B/\Phi_0$, where $N = n_\phi LW$ vortices contribute in a sample of width W and length L, the electric field is given by

$$E_x = N\frac{U_x}{W} = \frac{N\Phi_0 v_{\Phi,y}}{LW} = B v_{\Phi,y} \tag{2.39}$$

which in a more general form then results again in eq. 2.37. Neglecting the Magnus force in eq. 2.36, we arrive at

$$E_x = B\frac{\Phi_0}{\eta}(j_x - j_c) \tag{2.40}$$

for $|j_x| > j_c$ with the critical current density $j_c := f_p/\Phi_0$. Here one assumes that the vortices are entirely pinned for $|j_x| < j_c$ and thus $E_x = 0$ for $|j_x| < j_c$. The measured electric field is thus proportional to the applied driving current density, so in the easiest

case one measures an Ohmic flux flow resistance, further details of which will be discussed in the respective section, 2.3.

2.2.2 Thermomagnetic effects

Since the entropy density of a normal region, such as a vortex core, is higher than in the surrounding superconducting phase, the motion of vortices due to the Lorentz force is associated with the transport of entropy (and energy). Usually, the vortex motion results in flux lines entering the sample on one side, and leaving it on the opposite side, such that the overall vortex density $n_\phi = B/\Phi_0$ stays the same. This automatically implies absorption of heat on the side where they enter, and heat release on the other one, which in open-circuit conditions leads to a temperature gradient along the direction of vortex flow. Again, generally there is a component of the heat current density perpendicular to the applied current, called Ettingshausen effect, and one parallel thereto, called Peltier effect. Quite naturally, the heat current density is given by

$$\vec{j}_Q = T\vec{j}_{\mathrm{entropy}} = Tn_\phi S_\phi \vec{v}_\phi \quad , \tag{2.41}$$

where $\vec{j}_{\mathrm{entropy}}$ is the entropy current and S_ϕ the entropy per vortex line (see also discussion in appendix B). In the stationary case, one gets for the Ettingshausen effect

$$U_y = n_\phi T S_\phi v_{\phi,y} = -\Lambda \frac{\partial T}{\partial y} \quad , \tag{2.42}$$

where Λ is the contribution of mobile vortices to the heat conductivity, and using eq. 2.37, we obtain

$$\left|\frac{\partial T}{\partial y}\right| = \frac{TS_\phi}{\Lambda\Phi_0}\left|\frac{\partial U}{\partial x}\right| \quad . \tag{2.43}$$

A similar expression can be derived for the case of the Peltier effect. This simple proportionality between the transverse temperature gradient and the longitudinal electric field has been observed in many experiments (see e.g. review by Campbell and Evetts [31] and Huebener [32, 19] and respective references therein).

Let us now turn to another driving mechanism for vortices, the Nernst effect: a temperature gradient in $-x$-direction causes a voltage drop in $+y$-direction in presence of a magnetic field in $+z$-direction due to the action of the thermal force $-S_\phi \mathrm{grad}\, T$ (see figure 2.6). Note that this force results in vortex motion *down* the temperature gradient, i.e. *from hot to cold*.

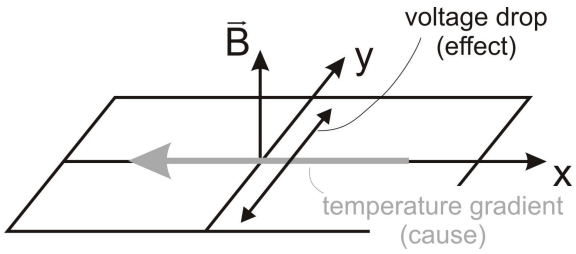

Figure 2.6: Sample geometry for flux motion due to the thermal force (Nernst effect).

The corresponding equation of motion reads

$$-S_\phi \mathrm{grad}\, T - \epsilon n_s e \vec{v}_\varphi \times \vec{\Phi}_0 - \eta \vec{v}_\varphi - \vec{f}_p = 0 \quad , \tag{2.44}$$

analogous to the Lorentz force. In case of a finite Hall angle or $\epsilon > 0$, the Magnus force leads to a nonzero flow component perpendicular to the temperature gradient, and accordingly to the Seebeck effect (voltage drop along $\mathrm{grad}\, T$), which will again be neglected. Although being fundamental to all thermal diffusion phenomena, the thermal force and its origin are not commonly familiar. A derivation following standard, but advanced literature on irreversible thermodynamics is given in appendix B.

Using again the force equation 2.44 together with 2.37 for the geometry shown in figure 2.6, we arrive at

$$E_y = -S_\phi \frac{B}{\eta} (\mathrm{grad}_x\, T - \mathrm{grad}_c\, T) \quad , \tag{2.45}$$

for $\mathrm{grad}_x\, T > \mathrm{grad}_c\, T$, where the critical temperature gradient $\mathrm{grad}_c\, T := -f_p/S_\phi$. Here it is assumed that for $\mathrm{grad}_x\, T < \mathrm{grad}_c\, T$, $E_y = 0$. Again, we see that the generated electric field is directly proportional to the applied driving force, i.e. the gradient of temperature (at least for small gradients, where the temperature dependence of the superconducting parameters can be neglected). The Nernst effect has been extensively studied in a great number of experiments on type-I (see e.g. [33, 34]) and conventional type-II superconductors (see e.g. [35, 36, 37, 38, 39]) as well as high-T_c-compounds (see e.g. [40, 41, 42, 43, 44, 45, 46]). More recently, it has been used to investigate the properties of the so-called pseudogap state (see e.g. [47]), where both a doping-dependent pseudogap opens and vortex-like excitations still exist far above T_c for hole-doped copper oxides.

2.2.3 The transport entropy of a moving vortex

The most important quantity to extract from measurements on the thermomagnetic effects is the transport entropy S_ϕ of a moving vortex. Experimentally, using either the Ettingshausen or the Nernst effect in type-II superconductors, one can rather easily extract the quantity S_ϕ/Φ_0 (according to eqs. 2.43 or 2.45 respectively), if additional measurements for the heat conductivity Λ or viscosity η (using the Lorentz force, see eq. 2.36) are carried out. As a function of temperature, the transport entropy vanishes for both $T \to 0$ and $T \to T_c$, and monotonically decreases with increasing magnetic field from its maximum value at low fields to zero upon reaching the upper critical field. Although this behavior has been documented experimentally rather well (see e.g. figure 2.7), theoretically the situation seems much more complicated and is still not resolved to complete satisfaction up to date.

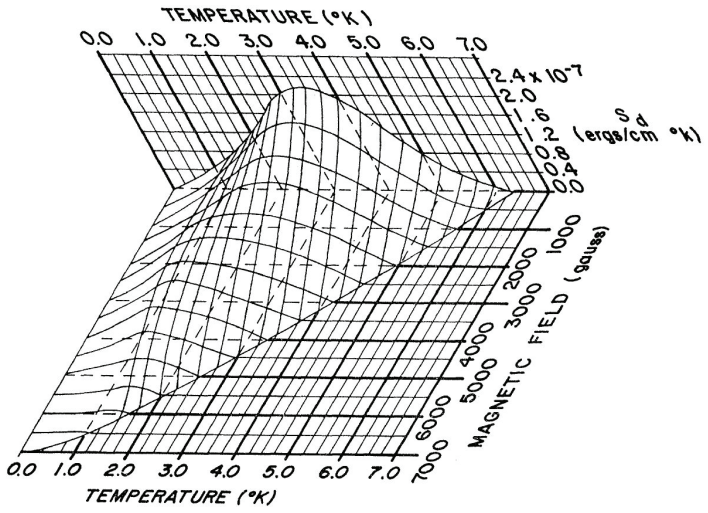

Figure 2.7: Transport entropy S_ϕ as a function of temperature and magnetic field for the type-II alloy In + 40 at.% Pb (source: [36]).

The transport entropy should be considered as a quantity which measures the local difference in entropy density associated with the vortex relative to the contribution of the background. This immediately explains why it should go to zero when $B \to B_{c2}$: as the vortex density grows and the cores start to overlap more and more, the excess entropy carried by a single vortex decreases.
Maki [48] proposed one of the first theoretical models for calculating S_ϕ from time-dependent Ginzburg-Landau theory in 1969. With slight corrections to his first approach

together with Caroli from 1967 [49], he derived the following equation for dirty type-II superconductors, which has been widely used in literature to this day:

$$S_\phi = \langle M \rangle \, L_D(t) = \frac{\Phi_0}{\mu_0 T} L_D(t) \frac{B_{c2} - B}{1.16(2\kappa^2 - 1) + 1} \, . \tag{2.46}$$

The function $L_D(t)$ is smoothly varying from 0 to 1 between $t = T/T_c = 0$ and $t = 1$, and $\langle M \rangle$ is the average magnetization. Important revisions came from Hu in 1976 [50,51] and Kopnin in 1993 [52], who changed the definition of the heat current operator used in the derivation in order to resolve apparent contradictions to either the Onsager principle or the third law of thermodynamics. But it seems that the final result 2.46 for dirty type-II superconductors in the limit of high fields (and temperatures close to T_c for applicability of the GL-theory) remains unchanged. Very recently (June 2008), Sergeev *et al.* [29] claimed that all of the previous models for the transport entropy connected to the thermomagnetic effects are based on the erroneous assumption that the superconducting electrons can actually carry entropy, in contradiction to the London postulate of a macroscopic single quantum state with zero entropy. They provide the following expression in the limit of large κ:

$$S_d(T) = a \frac{\partial}{\partial T} \left(\frac{\Phi_0}{4\pi\lambda(T)} \right)^2 \quad , \tag{2.47}$$

where $S_d(T)$ is the entropy counted from the surrounding background (as mentioned before), $a \approx 0.08$ and the term over which the derivative is taken stems from the contribution of the normal core to the free energy. The magnetic field dependence is claimed to be given by

$$S_d(B,T) = S_{\phi,\,\mathrm{Maki}}(B,T) \left[(T_c/T)^4 - 1 \right] \frac{\ln\left(B_{c2}/B\right)}{\ln \kappa} \quad . \tag{2.48}$$

The authors furthermore state that the predicted proportionality of the transport entropy and the average magnetization in the Maki formula has never been observed experimentally. Unfortunately, at the time of this writing, this controversy remains unresolved, especially since the contribution by Sergeev *et al.* has not yet been published officially. Nevertheless, I will try to compare our experimental results to both approaches (see chapter 6.2.1) and leave the theoretical discussion to the experts.

For further details on the historical developments of theoretical approaches to the transport entropy, the reader is referred to the original papers as well as the book by Huebener [19] (chapter 9.3 and 10.2).

2.3 Flux flow resistance

In this section, I will describe the different regimes of vortex motion in high-κ, low-pinning type-II superconductors in the dirty limit with respect to the parameters external magnetic field, temperature and applied transport current, closely following a book chapter on the properties of a-NbGe by Babić [16].

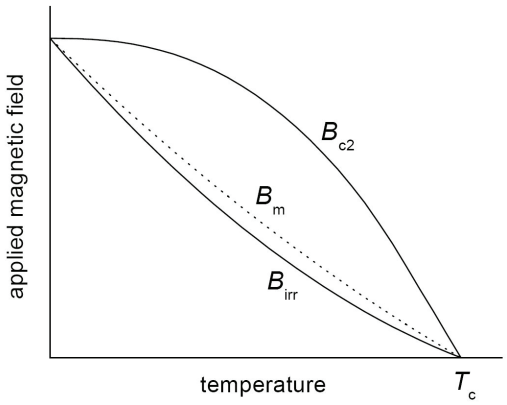

Figure 2.8: Schematic of equilibrium B-T-phase diagram for a-$Nb_{1-x}Ge_x$, showing the boundaries relevant for vortex transport: B_{irr} separates regions with finite pinning at low B, T from regions with negligible pinning at high B, T. Also indicated is a possible position of the melting field B_m, at which the vortex lattice starts to lose its long-range order, leading to a vortex liquid (picture taken from [16]).

The equilibrium phase diagram as shown in figure 2.8 contains three phase boundaries important for vortex transport. The irreversibility field B_{irr} separates regions with finite pinning at low B, T from regions with negligible pinning at high B, T. The name stems from magnetization measurements, which yield an irreversible response below B_{irr}. The upper critical field B_{c2} is the phase boundary to the normal state. These two lines can be obtained easily from transport measurements: at $B_{c2}(T)$, the resistivity of the sample approaches that of the normal state, and at B_{irr} any measurable sign of pinning in voltage-current characteristics disappears. The third, for our purposes in this section less important phase boundary is the melting field B_m, above which the vortex lattice loses its long-range order, forming a liquid-like state with vortices as single entities (see section 2.5). The lower critical field B_{c1}, which separates the Meissner from the Shubnikov phase, plays no important role since it is more than a factor of 1000 smaller than B_{c2} for a typical $\kappa \approx 75$ (at $T = 0$), see eq. 2.35.

2.3.1 Flux flow close to equilibrium

Let us first consider the geometry shown in figure 2.5 simplified by for now neglecting the Magnus force and the pinning force. Consequently, we are dealing with the force balance between Lorentz force and viscous damping, which is referred to as the regime of flux flow:

$$|j|\Phi_0 = \eta|u_\phi| \quad . \tag{2.49}$$

As already mentioned earlier, the vortex motion results in dissipation according to $\vec{E} = \vec{B} \times \vec{v}_\varphi$. This yields a flux flow resistance of

$$\rho_f = \frac{|E|}{|j|} = \frac{B\Phi_0}{\eta} \quad . \tag{2.50}$$

Two main contributions to the viscosity have been worked out. The first one, suggested by Bardeen and Stephen [53], assumes that the superconductor is governed by local electrodynamics and that the vortex core consists of a fully normal cylinder of radius ξ_{GL} where the dissipation is caused by ordinary resistive processes. This leads to

$$\eta_{BS} \approx \frac{\Phi_0 B_{c2}}{\rho_n} \quad , \tag{2.51}$$

where ρ_n is the resistivity in the normal state, and accordingly

$$\rho_f \approx \frac{B}{B_{c2}}\rho_n \quad , \tag{2.52}$$

which even if it is derived from an oversimplified picture goes along well with intuition, since the prefactor on the right hand side represents roughly the volume fraction of normal material.

The second contribution was suggested by Tinkham [54], who assumed that the Ginzburg-Landau wave function can only adjust to the time varying field configurations caused by the moving flux lines in the finite relaxation time $\tau = \hbar/\Delta$ required for nucleation. The corresponding energy loss per pairing-depairing cycle in the cores is equal to a fraction $(v/\xi_{GL})\tau$ of the superconducting condensation energy. Larkin and Ovchinnikov (LO) made a careful quantitative analysis of the above pictures and derived a powerful theory for superconductors in the dirty limit [14], which fully applies to a-NbGe. A detailed description of this theory is outside the scope of this thesis, but I will briefly give the main results.

In the close-to-equilibrium case, i.e. if the applied transport current is small enough such that the vortex cores sustain their equilibrium properties, three limiting cases for $\sigma_f = 1/\rho_f$ have been worked out:

- $T \ll T_c$, $B \ll B_{c2}$:
  Here, the vortex density is small, so that the vortices do not overlap and their contributions simply add up, and

$$\sigma_f = 0.9\sigma_n/b \quad , \tag{2.53}$$

  where $b = B/B_{c2}$ is the reduced magnetic field and $\sigma_n = 1/\rho_n$ is the normal state conductivity. So apart from the numerical factor 0.9, this result corresponds to the simple picture of Bardeen and Stephen.

- B close to B_{c2}, any T:
  In this case, due to the high vortex density, the cores of the vortices almost overlap and σ_f is not much larger than σ_n:

$$\sigma_f = \sigma_n \left[1 + \alpha(T)(1-b)\right] \quad , \tag{2.54}$$

  where $\alpha(T)$ is a temperature-dependent constant between 2 and 4.

- T close to T_c, any B:
  Close to T_c, the Ginzburg-Landau theory can be used to calculate Ψ, but a more complicated form of the electron distribution function requires a numerical solution for σ_f, the result of which is given by

$$\sigma_f = \sigma_n \left[1 + \frac{g(b)}{b\sqrt{1-t}}\right] \quad . \tag{2.55}$$

  The function g can be approximated by the interpolation formulae $g(b) = 4.04 - b^{1/4}(3.96 + 2.38b)$ for $b < 0.315$, and $g(b) = 0.43(1-b)^{3/2} + 0.69(1-b)^{5/2}$ for $b > 0.315$ (see figure 2.9).

2.3.2 Vortex motion in the presence of pinning

Any real material has a finite number of either defects in the crystal lattice or impurities of some kind such that the vortices see not a flat, but a rough free energy landscape. The minima in that landscape act as effective pinning centers, since vortices can lower their energy by occupying these preferably. For applications, this is highly desirable, since immobilizing flux lines reduces dissipation, such that in solenoids for high magnetic

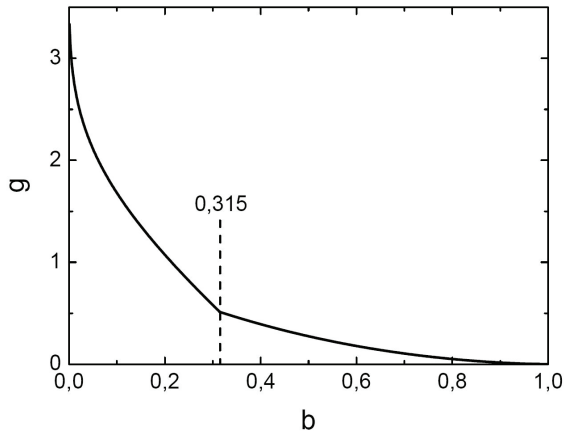

Figure 2.9: The function g(b), defined in two sections for below and above $b = 0.315$. Upon reaching B_{c2}, i.e. $b = 1$, the function becomes zero such that $\sigma_f \approx \sigma_n$ (compare to eq. 2.55).

fields the pinning is enhanced on purpose by use of so-called hard superconductors. For fundamental research on pure flux flow on the other hand, pinning is undesirable and makes things more complicated.

Figure 2.10 (a) shows a schematic of the free energy landscape a vortex (or a vortex bundle) sees in a real material. The free energy barriers created by the inhomogeneities of the material, tending to trap the flux lines, can be surmounted at finite temperatures with finite probability via the Boltzmann factor. In case (a), when no transport current is applied and the landscape is rough but flat, there is equal probability for vortex motion to the left and to the right, and no net vortex motion results. Still, this kind of *flux creep* can lead to a measurable decay of persistent currents in superconducting solenoids. An applied current on the other hand will tilt the 'washboard potential', such that vortices have a preferred direction ('downhill', see figure 2.10 (b)), which in case of moderate current densities (such that the energy landscape still plays a role) leads to the so-called *thermally assisted flux flow* (TAFF). Also in this case, one gets a linear resistivity according to $E = \rho j$, but one should be aware that this ρ is always smaller than ρ_f.

At the beginning of section 2.2, we already introduced an easy way of how to deal with the pinning, which is to use a critical current density j_c, above which vortices start to move (see eq. 2.40). Most of the time, this abrupt onset of dissipation is replaced in real samples by a smoother transition, i.e. a certain current range between the first appearance of E and the linear $E \propto j - j_c$ behaviour, which suggests first single vortex motion over short distances locally before the whole lattice starts to move on a global scale.

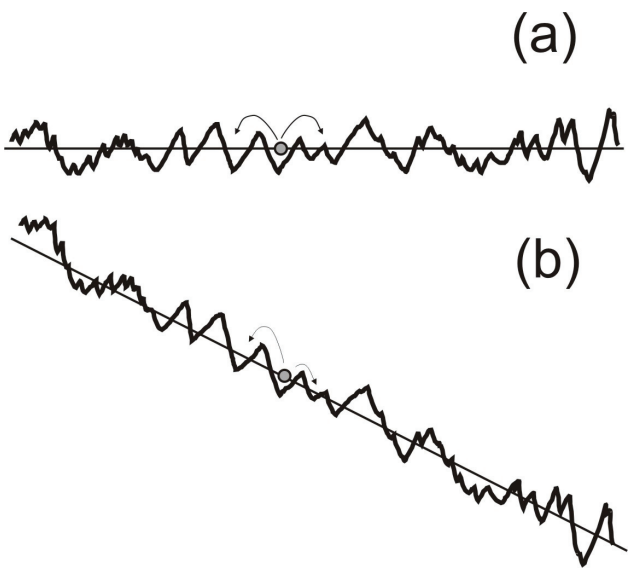

Figure 2.10: (a) Free energy landscape without (a) and with (b) transport current. The grey circle represents a vortex (or vortex bundle), sitting in a minimum, which is thermally assisted to jump over the barrier with equal (a) or unequal (b) probabilities for motion to the left and right direction.

2.3.3 Flux flow out of equilibrium

The dissipation due to vortex motion depends on the distribution of normal excitations in the core, which for high enough current densities (and thus electric fields $\vec{E}$) are no longer set by the bath temperature only. This results in strong nonlinearities in $E(j)$ for current densities larger than those for the ohmic case, but still much below the depairing limit. There are two distinctly different, limiting cases, for which clear pictures have been worked out: At temperatures close to the transition temperature T_c, the well-established theory of Larkin and Ovchinnikov [14] predicts flux-flow instabilities (FFI), i.e. sudden jumps in $E(j)$-curves, due to vortex core shrinking, and well below T_c, the observed FFI have been attributed to electron heating [55, 15].

Vortex core shrinking close to T_c

Close to the transition temperature T_c, the electric field has the strongest effect on the distribution function, and the result found by Larkin and Ovchinnikov is

$$j = \sigma_n \left[A + \frac{g(b)}{b\sqrt{1-t}} \frac{1}{1+(E/E_i)^2} \right] E \quad , \tag{2.56}$$

similar to eq. 2.55. The term $1/(1+(E/E_i)^2)$ reflects the decrease in η and thus the increased vortex velocity, thus also implying a higher level of dissipation, and A is a constant of order unity (exactly equal to 1 in equilibrium, otherwise reflects the suppression of superconductivity outside the cores by strong electric fields). The characteristic electric field E_i corresponds to a critical vortex velocity $u_i = E_i/B$, which depends on T and microscopic sample parameters via

$$u_i^2 = D\frac{\sqrt{14\zeta(3)}\sqrt{(1-T/T_c)}}{\pi\tau_{e,ph}} \quad . \tag{2.57}$$

Here, D is the diffusion constant, $\zeta(x)$ is the Riemann zeta function and $\tau_{e,ph}$ the electron-phonon inelastic scattering time. This can be understood in the following way: at low temperatures, $\tau_{e,ph} \propto (\theta_D/T)^3$ (where θ_D is the Debye temperature) which sets the rate at which the electrons excited by the electric field can relax. In the superconducting state, the rate τ_e at which this happens is even reduced by the fact that not every collision is effective:

$$\tau_e \propto \frac{k_B T_c}{\Delta}\tau_{e,ph} < \tau_{e,ph} \quad . \tag{2.58}$$

This means that if vortices move with a velocity such that they travel a distance $\ell_e \propto \sqrt{D\tau_e}$ during the time τ_e, the electrons will not have enough time to relax within the core and escape in the surrounding superfluid. Taking into account additionally the temperature dependence of the gap, which is close to T_c given by $\Delta \propto (1-T/T_c)^{(1/2)}$, we arrive at eq. 2.57 apart from the numerical factors. The critical velocity u_i is independent of magnetic field B as long as the quasiparticle relaxation length ℓ_e is larger than about the intervortex spacing $a \approx \sqrt{\Phi_0/B}$, i.e. for not too low magnetic fields, where a crossover to the behavior $u_i \propto B^{-1/2}$ was found (for references, see [19], chapter 15.4.4).

Another nice intuitive picture is shown in figure 2.11: quasiparticles inside the core region pick up energy from the electric field, accelerate, and are Andreev reflected at the core boundaries, alternating between electrons and holes. If no relaxation takes place soon enough, a fraction of the quasiparticles can finally leave the core region, reducing the number of quasiparticles and thus leading to a shrinkage of the core.

The above mechanism is well accepted and has been confirmed in measurements on conventional [56,57,15] as well as high-T_c superconductors (see references in [19], chapter 15.4.4). The $j(E)$ defined by eq. 2.56 has an "N" shape for small E_i, i.e. a maximum around E_i between zero and the ohmic part where the normal state is recovered. The region with negative differential conductivity is forbidden in current-biased measurements of voltage-current curves and thus results in a steep jump of the measured voltage. Figure 2.12 (a) shows a measurement of such a steep jump in the $E(j)$ of a NbGe microbridge at

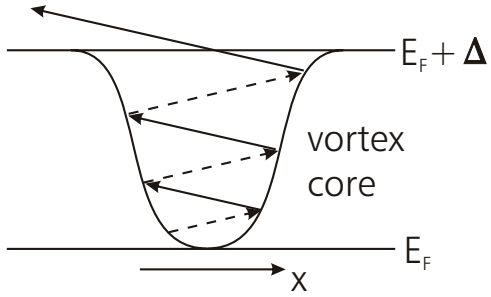

Figure 2.11: Intuitive picture of vortex-core shrinking mechanism: The electrons inside the core are accelerated by the strong electric field and Andreev reflected at the core boundaries until they are able to leave the core region, if no relaxation takes place before.

$t = 0.91$ and $b = 0.15$. While the theoretical curve according to Larkin and Ovchinnikov shows the mirrored "N"-shape, the measured curve suddenly jumps to a high value of E as expected, and shows near to perfect agreement with the rest of the theoretical curve. Part (b) of the same graph shows an $E(j)$ for $t = 0.91$ and $b = 0.62$, where the measured smooth curve is fitted perfectly by the theory. Since a clear jump is only expected for the lowest fields, the simplest way to find E_i from a measured $E(j)$ is to extract $\tilde{j} = j - \sigma_n E$, which has a maximum at $E = E_i$ irrespective of the shape of $E(j)$ (with or without FFI). The expected proportionality of E and B is also confirmed by the experiment (see inset of figure 2.12 (b)) and in fact provides the best indication from measurements that one is dealing with LO-FFI due to vortex-core shrinking.
The theory is expected to work for magnetic fields not too close to B_{c2} (predicted to be limited to $B < 0.4B_{c2}$ by Bezuglyj and Shklovskij [58] but in the meantime experimentally observed up to $0.7B_{c2}$ [15]) and for not too low temperatures, where another mechanism takes over:

Electron heating at low temperatures

The case $T \ll T_c$ was first investigated by Kunchur in 2002 [55] for high-T_c superconductors, and subsequently by Babić et al. for a-NbGe [16, 15]. Kunchur suggested that due to the infrequent inelastic electron-phonon scattering at low temperatures the main effect of the dissipation is to raise the electron temperature to $T^* > T_0$ (where T_0 is the bath temperature), to create additional quasiparticles and to diminish Δ. This leads to a vortex core expansion rather than shrinkage and the viscous drag is reduced because of a softening of gradients of the vortex profile rather than a removal of quasiparticles [55]. Al-

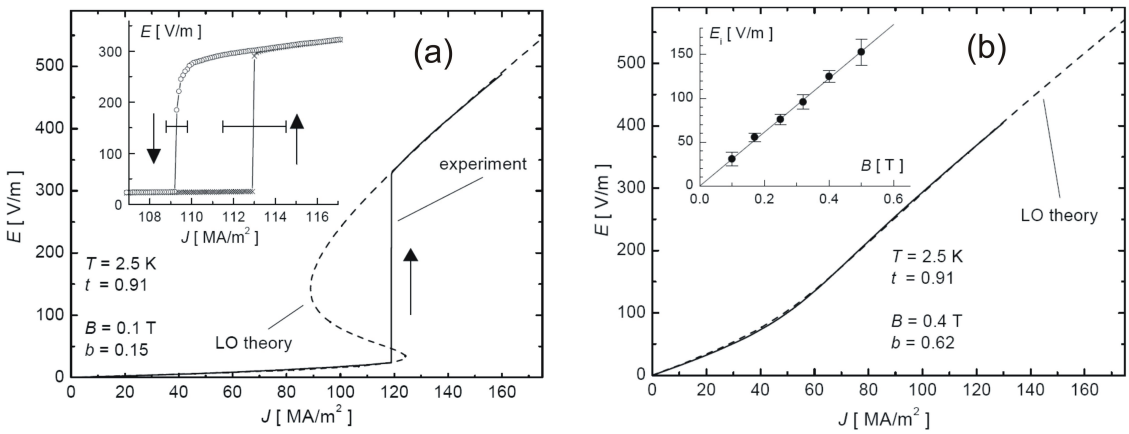

Figure 2.12: (a) Comparison of a measured $E(j)$ with FFI jump (solid line) at $t = 0.91$ and $b = 0.15$, obtained by sweeping the applied current up, and the prediction of eq. 2.56 shown by the dashed line. The region of $dE/dJ < 0$ is experimentally forbidden, resulting in a steep jump at $E_i \propto 30\mathrm{V/m}$ and a hysteresis shown in the inset. The arrows point in the current-sweep directions, and the horizontal error bars indicate the spread of the FFI in repeated measurements. (b) A measured smooth $E(j)$ (solid line) at $t = 0.91$ and $b = 0.62$, compared to eq. 2.56 calculated using $E_i = 125\,\mathrm{V/m}$ (dashed line). Inset: The values of E_i inferred from the $E(j)$ for several different magnetic fields and plotted vs B. The solid line represents $E_i = u_i B$, where $u_i \approx 305\,\mathrm{m/s}$. (Both graphs taken from [16].)

though still lacking a microscopic description, the measured data is explained surprisingly well by assuming that all observables change their temperature dependence according to a replacement of T_0 by $T^*(E)$. In particular, the upper critical field is reduced to its value at the elevated temperature, $B_{c2}(T^*) < B_{c2}(T_0)$, which is depicted in figure 2.13. The destruction of superconductivity happens at the field $E_c(B)$. This electric field (or equivalently current) dependent renormalization of $b^* = B/B_{c2}(T^*) = B/B_{c2}(E)$ then governs the flux flow and can be used in the respective formulae given in section 2.3.1 to describe the $E(j)$-curves.

Babić et al. [15] carried out a full analysis of $E(j)$-curves at low temperatures $T_0 \ll T_c$ and $0 < b < 1$, which we will repeat here to discuss the main features of the electron heating regime. In figure 2.14 (a), several $E(j)$ for different fields at $t = 0.40$ are shown. Although at first sight, the curves might appear to be very similar to the ones in figure 2.12, the origin of the FFI is completely different here and also the details differ quite a bit. For the lowest two magnetic fields, where the instability is most prominent, a partial fit according to the formula $j = j_c + 0.9\sigma_n E/b$ is plotted by the dotted lines, where the pinning is captured by the only fitting parameter j_c. The following steep rise of

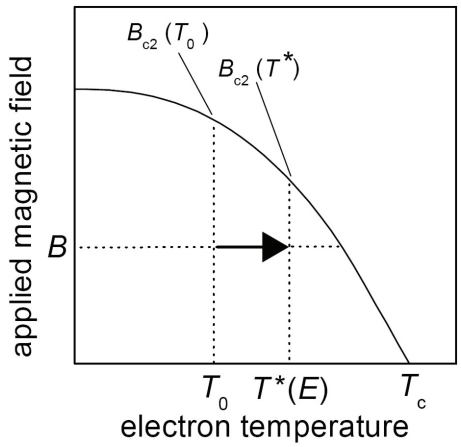

Figure 2.13: Schematic phase diagram illustrating the idea of the electron heating model: While initially 'working' at bath temperature T_0 and magnetic field B, a sufficiently high applied electrical current can lead to substantial heating of the electron system to an elevated temperature $T^*(E)$ (equivalently $T^*(j)$), which in turn leads to a reduced upper critical field $B_{c2}(T^*) < B_{c2}(T_0)$ (picture taken from [16]).

the dissipation can be attributed to the electron heating via the replacement $T_0 \rightarrow T^*$, implying a progressive reduction of B_{c2}. This leads to a nonmonotonic dependence of the ratio $E/b(E)$ on E, which causes the region of negative slope in $j(E)$ and thus an FFI jump similar as in the LO-case, but very different in origin.
The region of high dissipation where $\rho \rightarrow \rho_n$ can be understood by recalling eq. 2.54:

$$j = \sigma_n E \left[1 + \alpha(T)(1-b)\right] \quad . \tag{2.59}$$

In this case, we can neglect j_c, since we are now considering much higher current densities. The electron heating can be nicely incorporated if we replace b by its nonequilibrium value $b^*(E)$, which ultimately will lead to a destruction of superconductivity at $E_c(B)$. Since $\alpha(T)$ varies only moderately (namely between 2 and 4), we can in a first order approach assume it to be constant and invert eq. 2.59 to infer $b^*(E) = B/B_{c2}(E) = 1 - (1/\alpha)[j/(\sigma_n E) - 1]$ from the measured values of E and j. This has successfully been done in figure 2.14 (b) for $\alpha = 3$ and $b^* > 0.9$, where $\alpha(T) \approx \mathrm{const.}$ and the validity of this approach are expected (see eq. 2.54).

The similarity of the b^*-curves for different magnetic fields suggests a possible scaling $b^*(E/E_c)$ for a proper choice of $E_c(B)$, which indeed works as shown in figure 2.15 (a). By using appropriate values for $E_c(B)$, all $b^*(E)$-curves (left-hand scale) can be collapsed onto a single one when plotted versus $1 - E/E_c$. Such a scaling is typical close

to a dynamic phase boundary (compare e.g. to the scalings $1 - T/T_c$ close to T_c and $1 - B/B_{c2}$ close to B_{c2}).

The values for $E_c(B)$ thus obtained are plotted in the inset of the same figure, showing a linear dependence on b according to $E_c(B) = E_{c0}(1 - b)$ with $E_{c0} \approx 1500\,\mathrm{V/m}$. This represents a nice connection to the 'initial' conditions $(T_0, b = B/B_{c2}(T_0))$. Using the obtained values of $b^*(E)$ (or equivalently $b^*(j)$) and the measured $B_{c2}(T)$ in the B-T-phase plane, one can actually go 'backwards' and reconstruct the corresponding values of $T^*(E)$ $(T^*(j))$ (compare to schematic in figure 2.13). The result of this procedure is plotted in figure 2.15 (b) (solid lines), where the dotted lines indicate the corresponding $T_c(B)$.

The analysis can be extended one step further by making the connection between the observed scaling of E_c and the thermodynamics of the mixed state. The process of

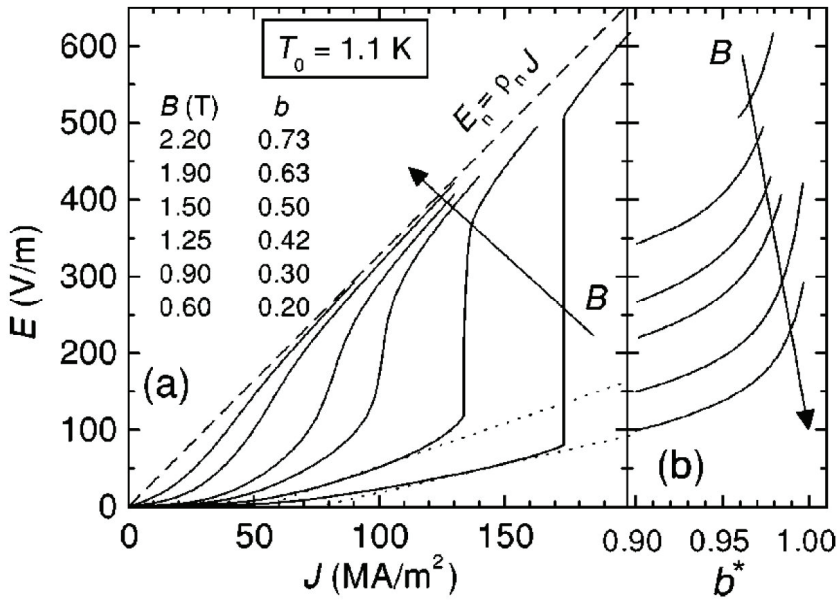

Figure 2.14: (a) Measured $E(j)$ at $t = 0.40$ (solid lines), for $0.6\,\mathrm{T} \leq B \leq 2.2\,\mathrm{T}$ ($B_{c2} = 3.0 \pm 0.1\,\mathrm{T}$) increasing as indicated by the arrow. The dashed line shows $E_n = \rho_n J$. The dotted lines are plots of $J = 0.9\sigma_n E/b + Jc$ for $0.6\,\mathrm{T}$ and $0.9\,\mathrm{T}$. (b) E vs. b^* calculated from the measured $E(j)$ and eq. 2.59 using $\alpha = 3$. The vertical scale is the same as in (a) and the arrow points again in the direction of increasing B (taken from [15]).

electron heating can be described by

$$jE\tau_e = G_s(T_0) - G_s(T^*) \quad , \tag{2.60}$$

where the right-hand side corresponds to the loss in Gibbs free energy density due to the evaporation of superfluid, and τ_e plays the same role as a relaxation time as τ_e in the LO-nonequilibrium case [59]. The normal part of the Gibbs free energy density due to the heating can safely be neglected here, since otherwise E_c vs. $1-b$ would have a noticeable intersect at $1-b=0$. At the phase boundary, $E=E_c$, the above equation yields $\sigma_n E_c^2 \tau_0 = G_s(T_0)$, where τ_0 is the relaxation time at E_c. According to Fetter and Hohenberg [60], we can write $G_s \approx U_s(1-b)^2$, where $U_s = B_{c2}^2/(4\mu_0\kappa^2)$ is the superconducting condensation energy for $B=0$ and thus arrive at the presumed scaling of $E_c \propto 1-b$ and receive a link between E_c and τ_0.
Now we can proceed to calculate the relaxation time $\tau = [G_s(T_0) - G_s(T^*)]/(jE)$ by inserting our values for $B_{c2}(E)$ into $G_s(T^*)$, and again obtain a scaling with respect to

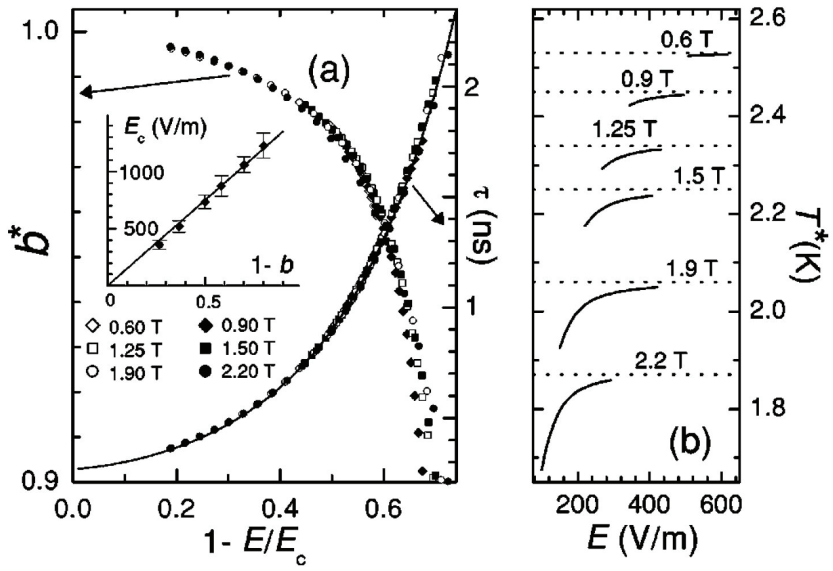

Figure 2.15: (a) Scaling plot of the nonequilibrium reduced magnetic field b^* (left-hand scale) and the quasiparticle scattering time τ (right-hand scale) vs. $1-E/E_c$, as indicated by the arrows and calculated as explained in the text. The solid line represents $\tau = \tau_0 \exp[3.5(1-E/E_c)^{3/2}]$ with $\tau_0 = 0.25\,\mathrm{ns}$. Inset: E_c against equilibrium $1-b$. The error bars indicate how much E_c varies if the scaling of b^* is performed using α between 2 and 4. (b) The electron temperature T^* (solid lines) vs. E for different B, estimated from the equilibrium $B_{c2}(T)$ characteristics. The dotted lines represent $T_c(B)$ (taken from [15]).

$1 - E/E_c$, shown in figure 2.15 (a) (right-hand scale). It is worth noting that this is not a simple consequence of the scaling of b^*, since $B_{c2}^2(E)$ enters the equations for $U_s(E)$ independently. Although the phenomenological equation

$$\tau_e(E,B) = \tau_0 \exp\left[3.5\,(1 - E/E_c(B))^{3/2}\right] \tag{2.61}$$

describes the measured data well, we will see in the results section that the parameters 3.5 and $3/2$ are not universal. The physical meaning of this relaxation time can be understood as the lifetime of nonequilibrium quasiparticles created by the evaporation of superfluid due to dissipation. Since the recombination to Cooper pairs via emission of thermal phonons is unlikely, it is reasonable to assume that instead nonequilibrium phonons are responsible for the recombination. A possible explanation for the observed form of eq. 2.61 goes as follows [16]: let us start from above E_c, where $\Delta(E,B) = 0$ and successively lower the electric field E such that Δ starts to grow. This goes along with a reduction of the number n_q of nonequilibrium quasiparticles, which we can assume to be exponential with Δ, yielding $d\Delta \propto -dn_q/n_q$ for the process. Since the recombination to a Cooper pair requires 2 quasiparticles, the corresponding scattering rate $\tau_q^{-1} \propto n_q^2$ and we obtain $d\Delta = C d\tau_q/(2\tau_q)$. To get τ itself, we can integrate this equation according to our cool-down process:

$$\int_0^{\Delta(E,B)} d\Delta = \frac{C}{2}\int_0^{\tau_e(E,B)} \frac{d\tau_q}{\tau_q} \Longrightarrow \tau_e(E,B) = \tau_0 \exp\left[2\Delta(E,B)/C\right] \tag{2.62}$$

When we now finally assume that also Δ is a function of $1 - E/E_c$ close to E_c, i.e. a power law like $\Delta(E,B) = \Delta(T_0)(1 - E/E_c(B))^{\mu}$, we arrive at

$$\tau_e(E,B) = \tau_0 \exp\left[\frac{2}{C}\Delta(T_0)(1 - E/E_c(B))^{\mu}\right] \quad , \tag{2.63}$$

which in case of $\mu = 3/2$ reproduces eq. 2.61. The prefactor of 3.5 might in principle originate from $\Delta(T_0) \approx \Delta_0$ and $C \approx k_B T_c$, but this should not be considered as much more than an educated guess.

2.4 Nonlocal vortex motion in mesoscopic channels

This section introduces the basics of the nonlocal effect which is at the very heart of all of the studies presented in this work.

The famous DC transformer of Giaever [4] in 1969 did not only provide one of the first proofs of the concept of flux motion by electrical measurements, but at the same time was the first example of nonlocal vortex motion in two electrically decoupled thin superconducting films. By using a thin layer of SiO_2 as an insulating barrier in between two films of Sn, he could show that upon applying a magnetic field perpendicular to the arrangement of thin films and by passing a current through the primary layer of Sn, also a voltage in the secondary layer of Sn develops due to the magnetic coupling of the vortex lines threading through both films.

In 2004, Grigorieva et al. [11] discovered a complementary flux transformer effect, where the nonlocality originates in the in-plane vortex-vortex repulsion over large distances in mesoscopic channels:

2.4.1 Transversal Flux Transformer Effect

When passing a current I through a horizontal wire (AB) connected to remote voltage probes (CD) via a perpendicular narrow channel all made of a low-pinning type-II superconductor, a nonlocal voltage can be measured that is entirely due to vortex motion, see figure 2.16. The voltage measured in isothermal sweeps of magnetic field applied perpendicular to the sample plane appears above a certain threshold field $B_d(T)$, which can be associated with always present finite pinning and more specifically with successive saturation of stronger pinning sites before interstitial vortices at higher vortex densities are free to move. Then it acquires a maximum value $R_p = U_{nl}(B_p)/I$ around a peak field $B_p(T)$ and finally decays again to zero upon approaching the upper critical field $B_{c2}(T)$. This behavior is shown in figures 2.17 & 2.18.

What is of course most remarkable about this effect is that there should be absolutely no voltage detectable when using a normal metal instead of a (low-pinning) type-II superconductor: Using the van-der-Pauw method [61], which for our case reads

$$1 = \exp\left(-\frac{\pi d}{\rho} R_{AB,CD}\right) + \exp\left(-\frac{\pi d}{\rho} R_{BC,DA}\right) \quad , \tag{2.64}$$

where d is the film thickness, ρ its resistivity and $R_{AB,CD} = (U_C - U_D)/I_{AB}$ and analogously $R_{BC,DA} = (U_D - U_A)/I_{BC}$, we arrive at

$$R_{AB,CD} = -\frac{\rho}{\pi d}\ln\left[1 - \exp\left(-\frac{\pi L}{W}\right)\right] \quad . \tag{2.65}$$

Here, we used that $R_{BC,DA} = \rho L/(Wd)$, which corresponds to a conventional 4-point measurement across the channel. When we plug in typical values for $\rho = 182\,\mu\Omega\mathrm{cm}$, $d = 40\,\mathrm{nm}$, $L = 2\,\mu\mathrm{m}$ and $W = 250\,\mathrm{nm}$, we see that $R_{AB,CD} \approx 10^{-10}\,\Omega$, which is analogous to saying that the current (density) sent in the local wire from A to B (or vice versa), as in the case of the TFTE, is reduced by this factor of 10^{10} at a distance of $L = 2\,\mu\mathrm{m}$ at the lower cross between C and D. Or in other words: there should be practically no measurable voltage in the nonlocal contacts. This has also been validated for the case of superconducting wires using numerical GL-simulations (see footnote 12 in ref. [11]).

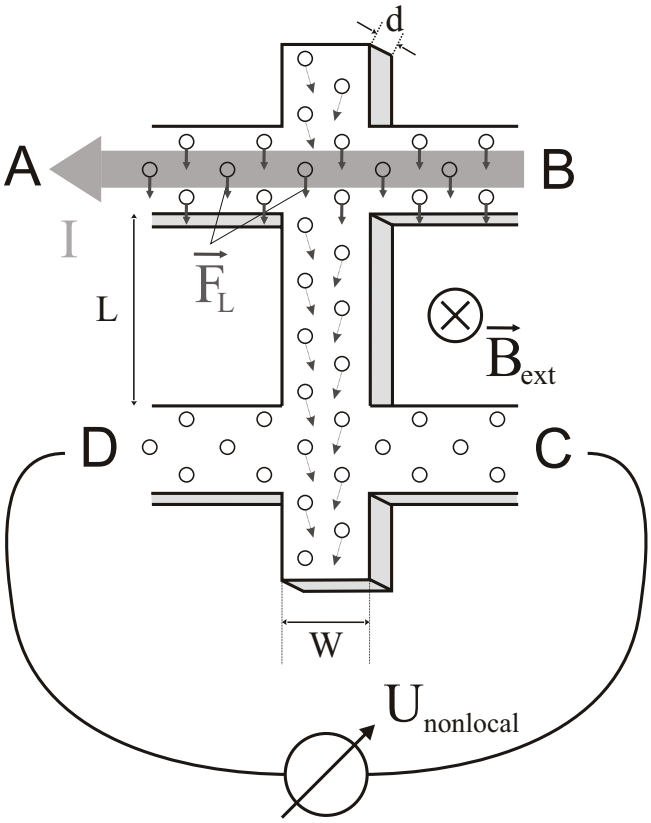

Figure 2.16: Schematic of the geometry used for the Transversal Flux Transformer Effect: A current sent in the local wire AB causes a nonlocal voltage drop at the remote contacts CD (compare also to SEM-image of actual sample, figure 3.5).

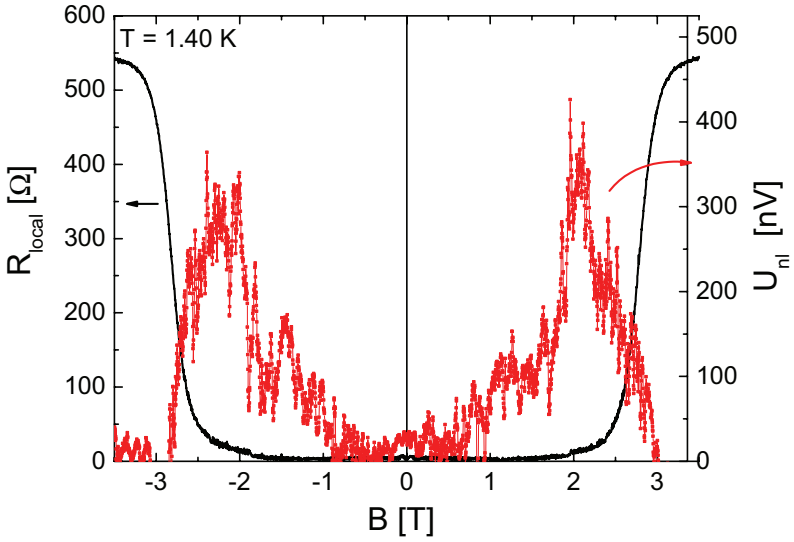

Figure 2.17: Magnetic field dependence of the nonlocal voltage U_{nl} (right y-axis) together with the corresponding magnetoresistance R_{local} from a local measurement (left y-axis, sample length $L = 2\,\mu$m, applied current $I = 300\,$nA; graph from [12]).

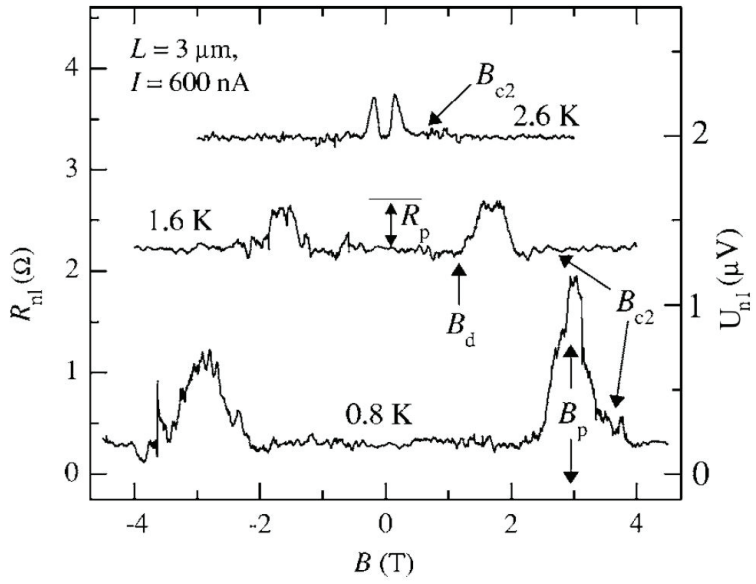

Figure 2.18: Magnetic field sweeps for different temperatures; Left scale shows the nonlocal resistance R_{nl}, while right scale indicates the corresponding voltage measured. The curves are offset for clarity, symbols denote characteristic fields as described in the text (graph from [12]).

So what is actually different when instead, we use a low-pinning type-II superconductor subject to an out-of-plane magnetic field? The answer is that the Lorentz force $\vec{f_L} = \vec{j} \times \vec{\Phi}_0$ due to the applied driving current in the local wire AB acts on the vortices therein[2], especially also on the ones immediately at the upper cross, pushing or pulling them (depending on the current direction) in the direction of the vertical channel that connects the two horizontal wires. The vortex-vortex repulsion together with the requirement for a constant vortex density set by the external magnetic field leads to a very efficient pressure transfer of the force chain through the channel, and once vortices move in the lower cross, a nonlocal voltage is generated via $\vec{E} = \vec{B} \times \vec{v}_\varphi$ (see figure 2.16). This simple idea captures the essence of the effect very nicely without further assumptions and was successfully used in ref. [12] to explain the observed $1/L$-dependence:

Considering the geometry (channel length L, wire width W, sample thickness d, cross-sectional area $A = Wd$), at vortex density $n_\Phi = B/\Phi_0$, a number of $n_\Phi W^2$ vortices in the upper cross of the local wire each encounter the Lorentz force $F_L = j\Phi_0 d$, thus applying a pressure of

$$p = \frac{n_\Phi \Phi_0 I}{d} \tag{2.66}$$

on the vortices in the channel. The corresponding pushing force per unit length $f = pA/d = pWd/d = pW$ is balanced by the force required to move $n_\Phi LW$ vortices in the channel against the frictional damping ηv_φ per vortex (where v_φ is the vortex velocity in the channel). This yields

$$\frac{n_\Phi \Phi_0 IW}{d} = n_\Phi LW\eta v_\varphi \Leftrightarrow v_\varphi = \frac{\Phi_0 I}{\eta L d} \propto 1/L \quad . \tag{2.67}$$

Using $U_{nl} = WBv_\varphi$, we obtain

$$R_{nl} = \frac{U_{nl}}{I} = WB\frac{\Phi_0 I}{\eta L d I} = \frac{\Phi_0 WB}{\eta L d} \quad . \tag{2.68}$$

In the last step, one further characteristic feature of the observed nonlocal signal was taken into account: as shown in figure 2.19, the measured nonlocal voltage scales linearly with applied current, which motivated the use of the nonlocal resistance R_{nl} as a measure of the efficiency of the effect.

Despite its simplicity, the above model accounts very well for the observed behavior of the nonlocal signal. The small, yet still finite pinning strength prohibits vortex motion below

[2] As described in the previous section, the Lorentz force is able to move vortices only if it is larger than the pinning force. This is why a low-pinning material is necessary for this rather small effect to be observable.

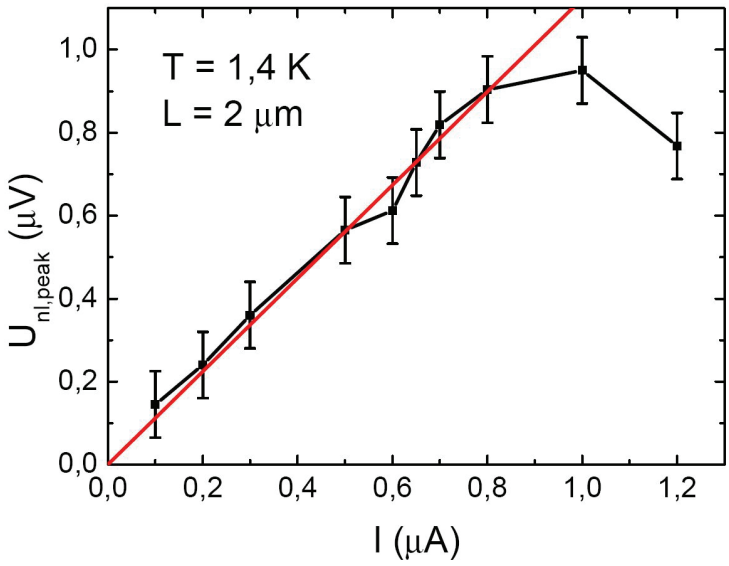

Figure 2.19: Current dependence of the nonlocal signal: the observed linear scaling motivated the use of a nonlocal resistance according to $R_{nl} = U_{nl}/I$ (graphs from [13]).

a certain threshold field both in the local and the nonlocal signal, but there are strong hints that it plays a minor role for the effect: The amorphous low-pinning materials used seem to have a certain number (or density) of stronger pinning sites that are occupied first during vortex nucleation, and after these are saturated, the 'excess' vortices can move along easy-flow rivers in between (see e.g. the zero magnetoresistance in low fields, figure 2.17, and refs. [62, 12]). In any case, the nonlocal signal in a-NbGe was already two orders of magnitude larger [12] than in the original study [11], which allowed for DC measurements of the effect. The fact that a vortex chain can propagate over such large distances $\sim 2\,\mu\mathrm{m}$ compared to the intervortex separation $a_0 = \sqrt{\Phi_0/B}$, which typically is of the order of $50\,\mathrm{nm}$ (at $B = 1\,\mathrm{T}$) can be attributed to the stiffness of the vortex lattice, which behaves more like an incompressible fluid, or in a more pictorial description, like hard spheres (tennis balls) in a tube with something like a half-pipe cross-section. The actual mechanism underlying the confinement could not yet be identified to complete satisfaction. Although Meissner screening currents and the resulting surface barrier seem to be a good candidate at first sight, the resulting profile in the case of high-κ type-II superconductors with a width $W = 250\,\mathrm{nm} \ll 825\,\mathrm{nm} = \lambda(0) \ll 17\,\mu\mathrm{m} = \lambda_\perp$ is almost entirely flat: in the case of negligible bulk pinning, the magnetization, which essentially comes from the screening currents and is given by the difference of the external

field and the induction inside the sample, is extremely small for the relevant field ranges in this kind of material. Another possible cause of the confinement could be given by surface pinning along the channel edges, which so far seems most likely. Measurements on more narrow channels with less effective pressure transfer point towards a region on the order of $50\,\mathrm{nm}$ of strongly pinned vortices along the edges, such that easy flow rivers inside the sample are built. I will come back to this point in the measurements section 6.2.1.

Another result of Grigorieva et al. [11] was the successful attribution of the fine structure of the nonlocal signal to changes in the vortex configurations, such as entry of additional vortices, or dips due to a jamming of vortices in the lower cross. Numerical simulations taking into account the actual geometric vortex arrangements using time-dependent GL-theory produced similar results to the measurements.

Taking a closer look at figure 2.19, one can see that for currents larger than $800\,\mathrm{nA}$ strong deviations from the linear behavior are observed. Already knowing about the nonlinearities and FFIs in the local IV-characteristics (see section 2.3.3), the question arises what will happen for even larger current densities? Does the nonlocal signal saturate? Or decay to zero? If yes, will it do so abruptly, or slowly? These questions built the main motivation for the measurements of DC nonlocal $V(I)$, which due to the smallness of the signal on the order of $50\,\mathrm{nV}$ is quite a task experimentally. The benefit of such measurements on the other hand would be that in contrast to magnetic field sweeps, the vortex density as well as the main superconducting parameters remain constant during current sweeps.

2.5 Thermal excitation of vortex-antivortex pairs

This last theory section introduces the basic ideas of the Berezinskii-Kosterlitz-Thouless (BKT) transition, which I would like to discuss on a very elementary level here.

Originally proposed for XY-magnets and liquid He by Kosterlitz and Thouless [63], who by the way supposed that this transition could not happen in a charged superfluid (=superconductor)[3], it was refined and expanded for the case of thin superconducting films by Halperin and Nelson [66] and even further generalized by Young [67] for arbitrary vector Coulomb gases. Similar considerations had already been carried out by Berezinskii [68, 69] several years earlier.

By now it has become clear that these theories apply to a whole class of 2D phase transition phenomena, with the key mechanism being dislocation mediated melting, which is absent in three dimensions. Strictly speaking, there are no 2D crystals with 'real' long-range order, in contrast to 3D, since the energy needed to allow for long wavelength excitations, which tend to destroy the translational symmetry on large length scales, is always finite for 2D and can be provided through thermal excitations [70]. On intermediate scales on the other hand, a quasi crystal can exist, since the logarithmic divergence of the particle displacements starts to play a major role only for large distances. Furthermore, it turns out that the phase transition actually happens in two steps: the low temperature phase, a solid-like crystal with a discrete symmetry looses its quasi long-range order due to the thermal excitation of bound pairs of topological defects. The latter can then start to dissociate at the melting temperature T_m, yet the remaining symmetry was shown to still be discrete, which means the resulting phase is not a liquid, which has a continuous translational symmetry. This intermediate phase between crystal and isotropic liquid is usually called the hexatic (or liquid-crystal) phase due to its sixfold directional symmetry. The second step from hexatic to liquid is provided via disclination unbinding (for a visual illustration, consult [70]). Since this second phase transition is usually even harder to observe experimentally, we will not pursue it any further, but now turn towards the implications of the melting transition for the vortex matter.

The topological defects in a superconductor are given by vortices. While the energy needed to create one single flux line (in the absence of an externally applied magnetic field) scales with the system size logarithmically, which forbids such excitations, the

[3]This statement refers to the argument that the finite range of the logarithmic interaction prevents the full analogy to superfluid He. This turns out to be less important in nowadays mesoscopic samples, where the lateral dimensions of a thin film are easily several orders of magnitude smaller than $\lambda_\perp$, the validity limit of the log-dependence (see also already remarks in ref. [64] and [65]).

energy for the creation of pairs of opposite vorticity (such that the total flux is still zero) remains finite even for infinite samples. More specifically, it is given by

$$\epsilon \propto 2\frac{\Phi_0^2}{\lambda_\perp} \ln\left(\frac{R_{12}}{\xi_{GL}}\right) \quad , \tag{2.69}$$

where R_{12} is the distance of the two vortices and $\lambda_\perp = \lambda^2/d$ is the effective penetration length for thin superconducting films of thickness d. Since this means that the thermally created pair can lower its energy by reducing the distance between the two cores, they attract each other until at separation ξ_{GL} they can annihilate again. So in thermal equilibrium, the creation and annihilation of vortex and antivortex pairs are balanced. While this is true for low temperatures[4], the form of the free energy $F = E - TS$ suggests that for high enough temperatures, the entropy term will start to dominate and favor pair dissociation. This consideration leads to an implicit criterion for the transition temperature T_{BKT} via

$$k_B T_{BKT} = \frac{\Phi_0^2}{8\pi\mu_0\lambda_\perp(T_{BKT})} \quad . \tag{2.70}$$

Beasley et al. [64] derived an explicit formula for T_{BKT} in the dirty limit given by

$$T_{BKT} = \frac{1}{1 + 0.173\, R_\square/R_c}\, T_c \quad , \tag{2.71}$$

where $R_c = \hbar/e^2 = 4.12\,\mathrm{k\Omega}/\square$ and $R_\square = \rho/d$ is the sheet resistance. This means that the closer the latter is to R_c, the lower is T_{BKT}. For very small sheet resistances on the other hand, the two temperatures should be almost indistinguishable.

Later it was suggested that the above formula should be slightly modified with a numerical factor of order 1 in front of the fraction of resistances to account for renormalizations [71, 72]. Although this equation may have its use in many situations, experiments suggested that it is actually "not the sheet resistance but the weakness of the superconductivity, as exemplified by a large transverse penetration depth" [73], which is the key ingredient for appearance of the BKT transition (see also ref. [74]).
A practically more useful approach is a determination of T_{BKT} from nonlinear IV-characteristics at different temperatures: at temperatures above T_{BKT}, a certain number of unbound vortices exists and leads to the ordinary flux flow dissipation, i.e. to a linear resistance. As the temperature is lowered, this linear resistance can be shown to vary as $\sim \exp(-C/\sqrt{T - T_{BKT}})$, with a sharp onset at T_{BKT}. Below T_{BKT} on the other hand, there are no free vortices in case of zero applied current. As soon as a finite current is

[4] "Since both the energy and the entropy depend logarithmically on the system size in the same way", see [63]

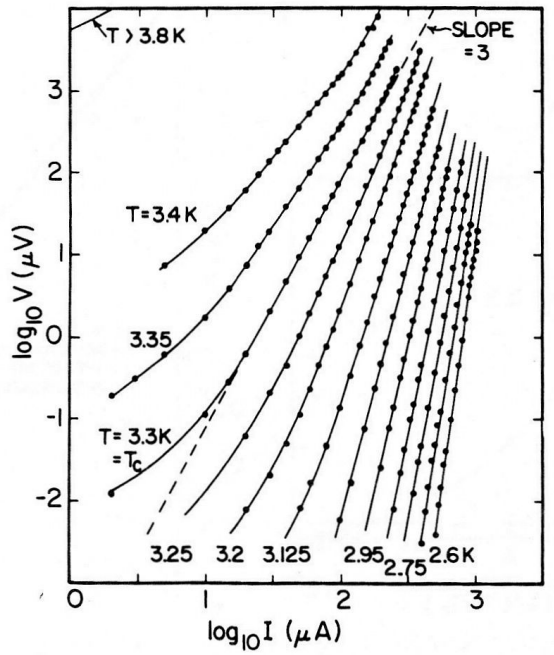

Figure 2.20: Nonlinear resistance measurements on high sheet-resistance films of Hg(Xe) for different temperatures in a log-log scale. At $T = 3.3\,\mathrm{K}$, the slope is equal to 3 and thus $T_{BKT} = 3.3\,\mathrm{K}$ (source: [75]).

applied, it exerts an equal and opposite force on the vortex and antivortex due to their opposite vorticity and starts to dissociate them. The number of vortices increases as I^2, and the voltage rises as $V \sim I^{a(T)}$, with $a(T) \approx 3$. Epstein et al. [71, 75] nicely confirmed these relations experimentally by measurements on high sheet-resistance films of Hg(Xe). Figure 2.20 shows a log-log plot of V(I)-characteristics taken at different temperatures.

The curves show a linear slope over large parts of the range, which allows for a determination of the exponent $a(T)$. Plotted as a function of T for three samples with different sheet resistance, one can easily determine both transition temperatures, see figure 2.21: at T_c, theory predicts a linear dependence for $a(T)$ and $a(T_c) = 1$, whereas at lower temperatures, the power-law dependence with exponent three should be observed [75]. This method seems to provide a reasonably well defined method to obtain the transition temperature T_{BKT}, although it has been argued that complications due to pinning and vortex injection at the edges due to the self-field of the supercurrent might arise [76].

The analysis can of course also be extended to account for finite magnetic fields. A

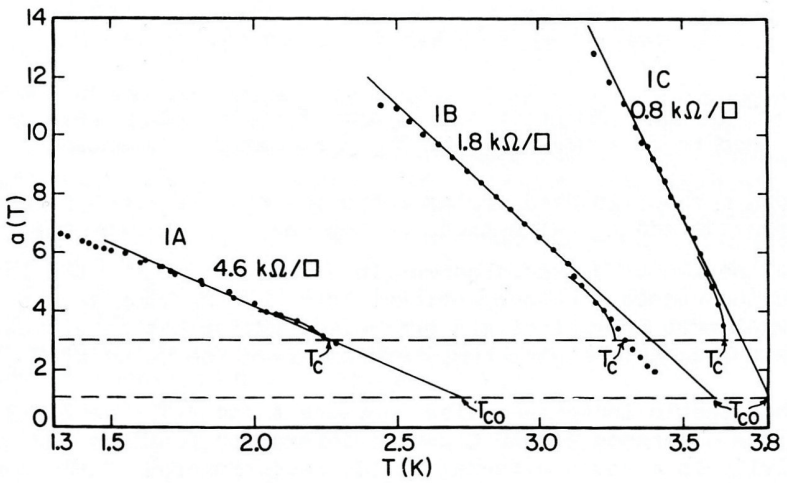

Figure 2.21: Plot of the exponent $a(T)$ in $V \sim I^{a(T)}$ vs. temperature for three samples with different sheet resistance. The extrapolations to $a(T) = 3$ and $a(T) = 1$ yield T_{BKT} and T_c respectively (source: [75]).

particularly nice example intimately connected to our experiments was performed by Berghuis et al. [77], who extracted the dislocation mediated melting field in thin films of a-NbGe. The criterion they used is given by a sharp drop to zero of the shear modulus c_{66} according to

$$Ac_{66}a_0^2 d/(k_B T) = 4\pi \quad , \tag{2.72}$$

where $a_0 = 1.075\sqrt{\Phi_0/B}$ is the lattice spacing and the parameter A of order unity represents renormalizations, derived by Fisher [65]. The shear modulus itself is given by

$$c_{66} = \frac{B_{c2}^2(t)}{4\mu_0} b(1 - 0.29b)(1 - b)^2 \quad , \tag{2.73}$$

where $B_c(t) = B_c(0)(1 - t^2)$, and b and t are the reduced field and temperature respectively [78]. We shall conclude this section here by noting that the BKT-transition can substantially influence and broaden the resistive transition, especially in high-T_c materials, but is somewhat difficult to be clearly observed in conventional type-II superconductors due to the compromise that has to be made between ultimately thin (high sheet resistance) and homogeneous films (thicker films). Apart from materials showing metal-to-insulator transitions, the newer class of superconductor-to-insulator transition materials seem to be better candidates or playgrounds for fundamental research in that regard.

Chapter 3

Material and sample preparation

In this chapter, I will briefly discuss the material properties of a-NbGe and the sample preparation process.

3.1 Amorphous $\mathrm{Nb_{0.7}Ge_{0.3}}$

3.1.1 Reasons for the material choice

While for applications, it is desirable to immobilize vortices in order to minimize dissipation and allow for high critical currents, e.g. to produce high magnetic fields with solenoids made from so-called hard superconductors, fundamental research on vortex dynamics requires obviously quite the opposite, i.e. highly mobile flux lines. This need for materials with intrinsically low pinning is met best by either high-T_c-superconductors (HTSCs) or thin films of amorphous alloys of transition metals like Nb and Mo with some elements of the IV group, such as Ge and Si. Since it turned out that the situation in the HTSCs is much more complicated, the dissipative mechanisms being dominated by fluctuations, it seems that the amorphous thin films offer the best possible playground for investigating the properties of free vortex motion.
Amongst these films, amorphous $\mathrm{Nb_{1-x}Ge_x}$ with $x \approx 0.3$ is one of the best examples for extremely low pinning, and thus the ideal candidate for our purposes. While the crystalline counterpart $\mathrm{Nb_3Ge}$ had the highest transition temperature (roughly $23\,\mathrm{K}$) ever observed before the discovery of the HTSCs and very strong pinning, $\mathrm{Nb_{0.7}Ge_{0.3}}$ is a weak-coupling, conventional superconductor in the dirty limit with a T_c of $2.7 - 3\,\mathrm{K}$, and the Ginzburg-Landau parameters $\lambda(0) \approx 800 - 1000\,\mathrm{nm}$, $\xi(0) \approx 6 - 8\,\mathrm{nm}$ and $\kappa \approx 70 - 100$. While the GL-parameters slightly vary from sample to sample, the low-lying B_{irr}-line in the B-T phase diagram and thus large parts therein with negligible pinning are common to all of them, provided that the sample thickness is not much larger

than several ξ. After trying different film thicknesses ($d = 20$, 40 and $60\,\mathrm{nm}$) in previous experiments (see e.g. [12, 13, 79]), all samples used in this study have $d = 40\,\mathrm{nm}$. This seems to provide the best trade-off between low pinning (thin films) and homogeneous samples (thicker films).

3.1.2 Material parameters

The theoretical basis for extracting the material parameters of superconductors like a-NbGe from measurements was built by Gor'kov [26] and later used by Kes and Tsuei [80], who derived practically useful expressions connecting the relevant quantities available from simple transport measurements. These have been conveniently summarized in the book chapter by Babić [16] as follows.

Close to T_c, the coherence length of a weak-coupling, amorphous superconductor in the dirty limit ($\ell \ll \xi_0$) is given by

$$\xi(T) = \sqrt{\frac{e\Phi_0 D}{8k_B T_c(1-t)}} \quad , \tag{3.1}$$

where $D = v_f \ell/3 = [2e^2\rho_0 N^*(0)]^{-1}$ is the diffusion constant (v_f: Fermi velocity, ℓ: mean free path, $N^*(0)$: (renormalized) density of states at the Fermi level). Together with the GL-solution for the upper critical field close to T_c, $B_{c2}(T) = \Phi_0/(2\pi\xi^2(t))$, it is convenient to define

$$\mathcal{S} := -\left(\frac{dB_{c2}(T)}{dT}\right)_{T=T_c} = \frac{B_{c2}^0}{T_c} = \frac{\Phi_0}{2\pi T_c \xi^2(0)} = \frac{8k_B}{2\pi e D} \quad . \tag{3.2}$$

Since this is only valid near T_c, the intersection of the linear fit to $B_{c2}(T)$ with the y-axis, B_{c2}^0, is about 1.4 times larger than the actual $B_{c2}(T = 0\,\mathrm{K})$. Using then the BCS-expressions for the condensation energy density

$$U_c = \frac{B_c^2(0)}{2\mu_0} = 1.56\, N^*(0)(k_B T_c)^2 \tag{3.3}$$

and the (negative) slope of the thermodynamic critical field (close to T_c)

$$-\left(\frac{dB_c(T)}{dT}\right)_{T=T_c} = 1.73\frac{B_c(0)}{T_c} \quad , \tag{3.4}$$

one can define

$$\kappa = \frac{1}{\sqrt{2}}\left(\frac{dB_{c2}/dT}{dB_c/dT}\right) = ... = 3.54 \times 10^4\sqrt{\rho_0 \mathcal{S}} \quad . \tag{3.5}$$

Usually, the temperature dependence of κ can be neglected. Employing two more BCS-results, namely $\lambda(0) = \lambda_L(0)\sqrt{\xi_0/\ell}$ and $\kappa = 0.715\,\lambda_L(0)/\ell$, we obtain

$$\lambda(0) = 1.63\,\kappa\xi(0) = 1.05 \times 10^{-3}\sqrt{\frac{\rho_0}{T_c}} \quad . \tag{3.6}$$

In fact, it turns out that it is sufficient to measure ρ_0, T_c and $\mathcal{S}$ in order to calculate all superconducting parameters according to the formulas summarized in table 3.1. In the bottom row of the table, typical values for amorphous $Nb_{0.7}Ge_{0.3}$ are listed.

	κ	$\xi(0)$ [m]	$\lambda(0)$ [m]	$B_c(0)$ [T]	$N(0)$ [$\mathrm{J^{-1}m^{-3}}$]
expression	$(\rho_0\mathcal{S})^{1/2}$	$(T_c\mathcal{S})^{-1/2}$	$(\rho_0/T_c)^{1/2}$	$T_c(\mathcal{S}/\rho_0)^{1/2}$	$\mathcal{S}/\rho_0$
multiplier	3.54×10^4	1.81×10^{-8}	1.05×10^{-3}	1.15×10^{-5}	1.78×10^{41}
value	90	7×10^{-9}	1000×10^{-9}	30×10^{-3}	1.8×10^{47}

Table 3.1: Summary of the expressions for determination of superconducting parameters of dirty superconductors from transport measurements. To calculate a parameter use the given expression, insert ρ_0 in Ωm, $\mathcal{S}$ in T/K and T_c in K, and multiply with the corresponding multiplier. In the last row, values typical of a-$Nb_{0.7}Ge_{0.3}$ are given [16].

3.2 Fabrication of mesoscopic channels

In this section, the process of sample fabrication is briefly summarized. The complete recipe can be found in appendix C.

The previous studies on the Transversal Flux Transformer Effect, which had already clarified the channel width- and length-dependence of the effect, suggested a size of roughly $2\,\mu\mathrm{m}$ channel length and $250\,\mathrm{nm}$ channel width for close to optimal efficiency of the effect. These dimensions built the starting point of the design and remained unchanged for all samples used during this study.
The second requirement came from the plans to also perform measurements in the high-frequency regime, where a minimum contact resistance from the leads and pads towards the central structure leads to a maximum cut-off frequency that can pass through the whole setup: cables to instruments + measurements lines in cryostat + sample resistance + capacitances via

$$f_{\mathrm{cut-off}} = 1/(2\pi R_{total} C_{total}) \quad , \tag{3.7}$$

where R_{total} and C_{total} denote the total resistance and capacitance of the setup. Details on this topic will be discussed in chapter A, where the results from the time-dependent measurements are presented. The impact on the sample design was that the lead and pad areas were maximized in order to minimize the sample resistance. This design (see figure 3.1) was used for all measurements presented here.
Due to the relatively small dimensions of the main structure, electron-beam lithography (EBL) was employed for the sample preparation. Two different approaches were taken: (i) a conventional positive EBL resist and (ii) a negative EBL resist. Case (i) is the standard workhorse of sample preparation in mesoscopic physics. Here the desired pattern is first written onto a neutral substrate (Si/SiO_2) covered with a positive EBL resist, which after development shows a positive of the desired structure (i.e. the resist is gone where the pattern was written via EBL). This mask can then be used to sputter the thin film of a-NbGe onto the substrate in the desired geometry. In the following lift-off, the remaining resist is dissolved and washed away together with the undesired parts of the NbGe (which lie on top of the resist), so that finally the designated structure remains (compare to figure 3.2). The second approach (ii) starts off with a homogeneous layer of a-NbGe, covering the whole chip, which is then coated with a negative resist. After the exposition of the pattern via EBL, the development this time dissolves everything but the structure itself. A dry etching step (RIE: reactive ion etching) removes the film where it is not covered and thus protected by the resist, so that after sufficient etching time, again only the desired structure remains (see figure 3.3).

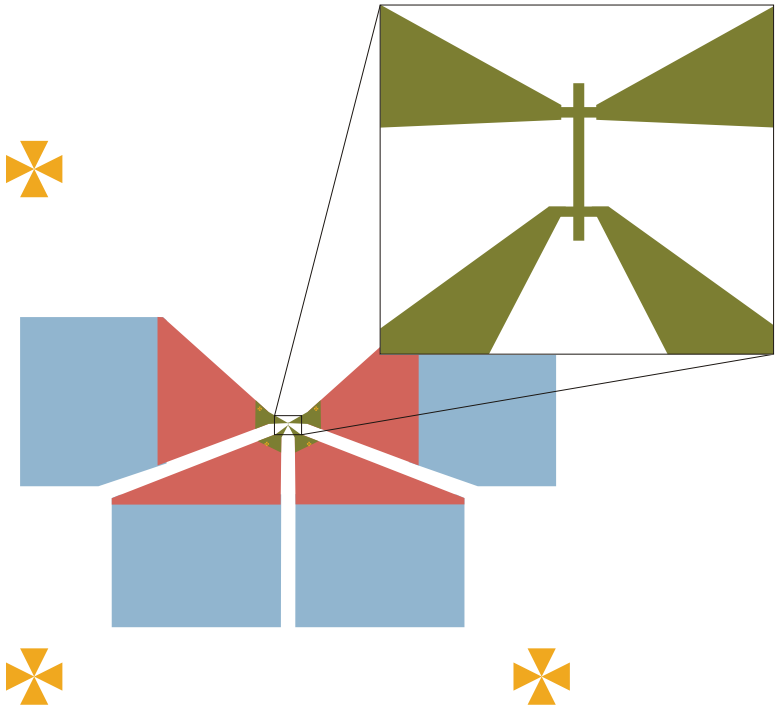

Figure 3.1: Sample design as drawn in the electron-beam lithography software (left main figure) and a zoom of the inner structure (upper right). The pads (blue), the leads (red) and the inner structure (brown) are all made of NbGe, and the alignment markers (orange) have been made of Au. The size of the pads is roughly $100 \times 100\,\mu\mathrm{m}^2$*, and the vertical channel of the inner structure has a length of* $2\,\mu\mathrm{m}$ *and a width of* $250\,\mathrm{nm}$*.*

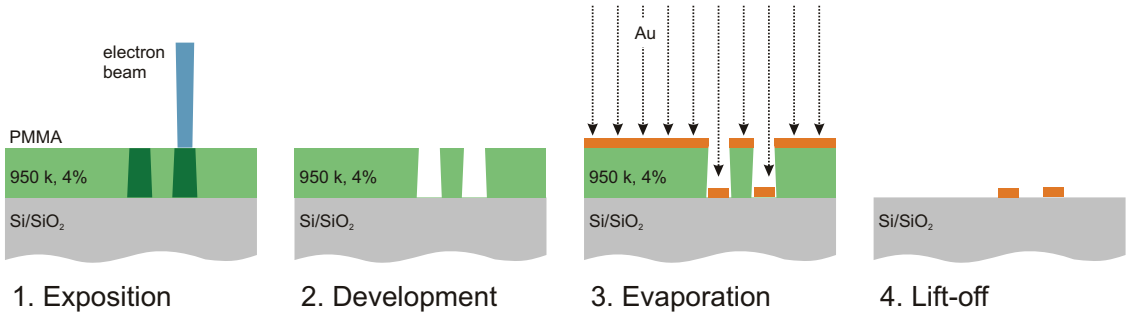

Figure 3.2: Lift-off process used to define Au-markers for repositioning

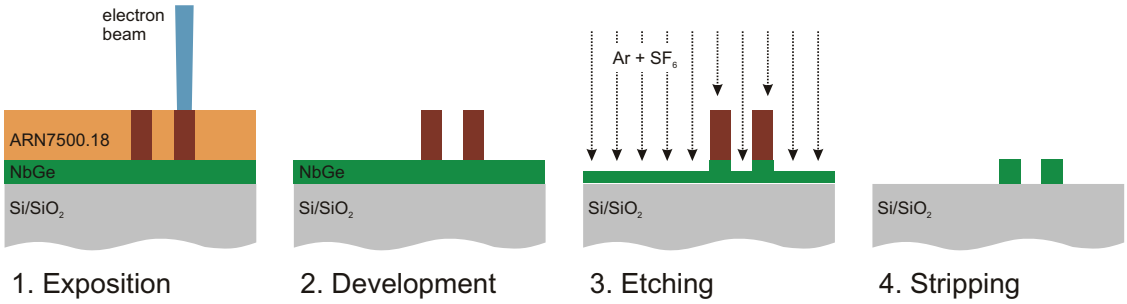

Figure 3.3: Etching process used to define the sample structure of the NbGe

During the standard lift-off process (using a double-layer of standard, positive EBL-resist), the following problem occurred: Since sputtering is a much less directed form of depositing material onto a substrate than for example evaporation, it can happen that some material is deposited on the vertical side walls of the trench in the resist. Sometimes this leads to undesired thin flaps at the edges of the structure after the lift-off that cannot be removed (see figure 3.4). It can even be that short circuits are created by these "wings", since they might topple over to the sides.
The above problem inspired the use of a negative EBL-resist, which implies etching a homogeneous film as described above and depicted in figure 3.3. After some trial-and-error period at the beginning, since this process was newly established in our group, the results were quite satisfying, as shown in figure 3.5. Apart from nicer sample edges, this also had the advantage that a small stockpile of wafers with different thicknesses of a-NbGe could be procured as a starting point for sample preparation[1], which sped up the whole process quite a bit. Before, each lift-off sample had to be sent away for sputtering in between the EBL and the lift-off itself.
As indicated in figure 3.1, the sample also contained alignment markers for repositioning (in a planned extra step for adding an additional wire in the center at the top, see outlook in the summary), which were produced separately beforehand by the standard lift-off EBL and evaporation of Au.
For further details the interested reader is referred to the recipe in appendix C.

[1]Until very recently, all of our a-NbGe samples have kindly been sputtered at the Phys. Inst. and DFG Center for Funct. Nanostr. (CFN), Univ. Karlsruhe, Germany by Dr. Christoph Sürgers

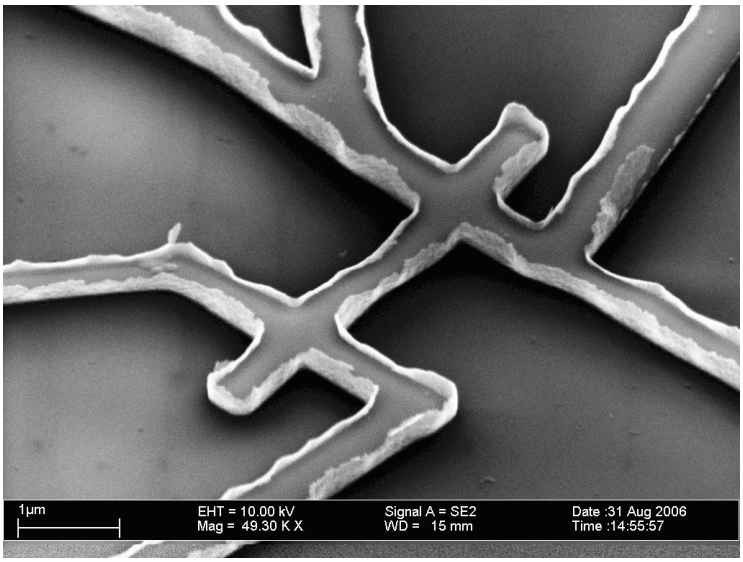

Figure 3.4: SEM-image of one of the lift-off samples with undesired "wings".

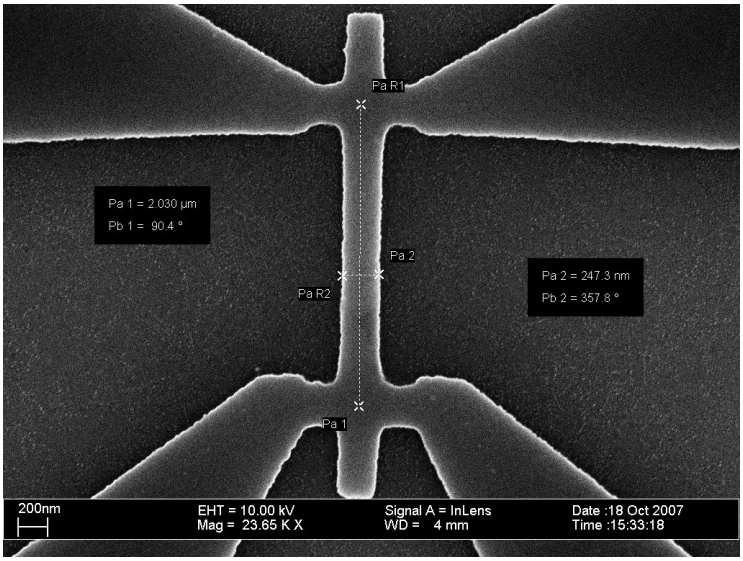

Figure 3.5: SEM-image of one of the samples used in this study.

Chapter 4

Measurement setups

This chapter gives a brief summary of the experimental setups used for the different measurements. The first two sections describe the standard setups for the characterization and $E(j)$-curves as well as investigations on a possible Berezinskii-Kosterlitz-Thouless transition. Special emphasis is put on the difference between the local and nonlocal schemes. The last section briefly discusses the time-dependent measurements, where a box-car averaging technique was employed.

All of these measurements have in common that they were performed in a sorption pumped ^{3}He-system with a base temperature of $300\,\mathrm{mK}$, a *Heliox VL* insert from *Oxford Instruments*, equipped with a $12\,\mathrm{T}$ magnet ($14\,\mathrm{T}$ with the help of a lambda stage). The insert has two cooling stages, a $1\,\mathrm{K}$ pot with a needle valve, used to pre-cool and condense the ^{3}He in the second closed cooling cycle. There, the ^{3}He is sorption pumped, and the system is operated in single shot mode. Everything below the $300\,\mathrm{mK}$ pot has been replaced by custom made parts during this thesis. Details of the new sample holder can be found in appendix D. The improvements include a rotatable sample holder, which can be operated at base temperature to switch the orientation of the applied magnetic field from in-plane to out-of-plane or anything in between (at roughly 2° precision), and 8 singly filtered coaxial lines, which were used for all of the high-sensitivity measurements during this study. A photograph and a schematic of the insert with the measurement lines and filtering is shown in figure 4.1.
Since the standard ceramic chip carriers used for all of the cryostats at our chair have 20 contacts, also each insert has 20 measurements lines (plus some spare lines). Usually in our group's systems, these are divided up into 8 coaxial lines for sensitive voltage measurements and 12 'normal' wires for current and voltage bias and gate control. All of these are typically connected to the instruments via BNC cables or semi-rigid SMA lines, and they enter the insert through break-out boxes with grounding switches at the top. While the 12 'normal' wires are equipped with permanent π-filters for radio frequency

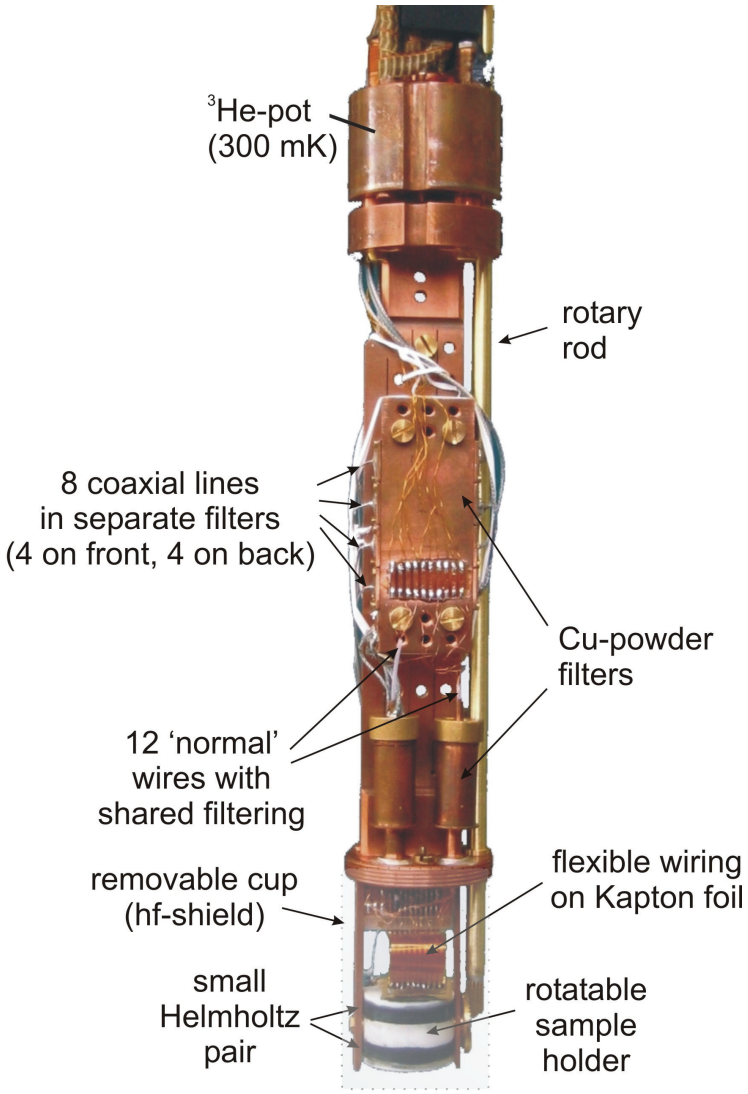

Figure 4.1: Photograph of the bottom part of the insert with details of the filtering and measurements lines. Everything shown below the ^{3}He-pot has been rebuilt and custom-made during this thesis.

(RF) damping, these are optional for the 8 coaxial lines. All of the lines are thoroughly thermalized at $4.2\,\mathrm{K}$ (temperature of the He bath), $1.8\,\mathrm{K}$ (temperature of the '$1\,\mathrm{K}$-pot') and the sample temperature given by the ^{3}He-pot (base temperature $0.3\,\mathrm{K}$). These thermalizations have been renewed during the course of this work: the wires are broken and soldered onto Cu-pads on Kapton foil, which itself is glued onto Ag plates connected to the thermal sinks. Previously, these plates had been made of Cu, which has a smaller

heat conductivity. Additionally to the π-filters, all lines are going through Cu-powder filters which are used to cut-off higher frequencies, which can not only produce noise but also lead to heating effects. These were originally developed by Martinis et al. [81], while a nice comparison and overview of different filtering methods and combinations can be found in ref. [82]. Previously, all lines went through such filters in packs of 6-8, allowing for substantial cross-talk in pulsed measurements. This was also changed during this work, such that now the 8 coaxial lines all have their own single filter box to minimize the cross-talk. A short summary of the production process of these filters can be found in appendix D together with a performance curve.

At the very bottom of the insert, a small Helmholtz pair of superconducting wires was made to allow for small fields perpendicular to the sample plane as well as crossed fields, when rotating the sample holder by 90° and combining this field with that of the large magnet. This can for example be used for spintronics devices such as nanotubes with ferromagnetic contacts.

All instruments can be controlled via GPIB by a central computer by the measurement routine *MeasureXP*, which has been developed and improved over several years by the former Ph.D. student Johannes Bentner. It is based on the *LabWindows CVI* development kit of *National Instruments* and is capable of simultaneously reading 4 different channels, e.g. lock-in amplifiers, voltmeters, nanovoltmeters and temperature, while two devices or parameters can be swept as master and slave device. This way one can for example measure $R(B)$ via a voltage measurement as a function both of magnetic field and temperature. The latter two are controlled by the standard *Oxford Instruments* equipment, i.e. an *ITC 503* temperature controller and an *IPS* power supply for the magnet. The variation of two parameters at once can be carried out fully automated by scripts (text files).

4.1 Characterization and local E(j)-curves

For characterizing the sample by means of $R(T)$- and $R(B)$-curves as well as for the local $E(j)$ measurements, the same connection scheme and instruments were used. Figure 4.2 shows a schematic drawing of the sample with the connections for current bias and voltage measurement, i.e. a conventional 4-point measurement over the channel of $L = 2\,\mu\mathrm{m}$ and width $W = 250\,\mathrm{nm}$ (film thickness $d = 40\,\mathrm{nm}$). Since for this part of the sample, the geometry is well known, one can easily get the geometry independent value of $\rho = RWd/L$. This setup has been used for extracting the parameters T_c, ρ_n and $B_{c2}(T)$ (see chapter 5).

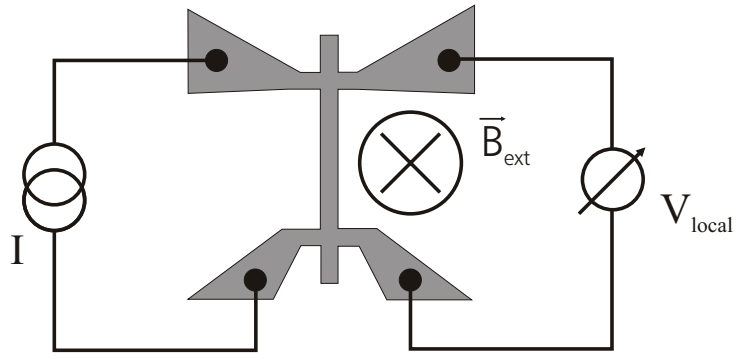

Figure 4.2: Schematic of the measurement setup for all local measurements, including characterization: conventional 4-point geometry over the channel of $L = 2\,\mu\mathrm{m}$ *and width* $W = 250\,\mathrm{nm}$.

The current bias was realized in the AC case by the sinusoidal voltage output of the lock-in amplifier (*SR830* of *Stanford Research Instruments*) and a series resistor ($R_{bias} = 1$ or $10\,\mathrm{M\Omega} > 10^3\,R_{sample}$) put as closely to the break-out box on the head of the insert as possible to reduce noise pick-up in the line behind the resistor. The voltage output from the sample was additionally amplified 102 times by a battery-operated, low-noise preamplifier (*Li-75A* of *NF Circuit Design Block Co*) before measured with the lock-in. For the DC measurements, a programmable DC (current and) voltage source (*Yokogawa 7651*) with the same series resistor was used to define the current. The voltage measurement was then done with a nanovoltmeter (*Agilent 34420A*).

4.2 Nonlocal E(j)-curves and BKT-measurements

The instruments and methods used for the nonlocal measurements are generally exactly the same as in case of the local measurements, but the connection scheme is quite different, see figure 4.3. As already described in the introductory section on the Transversal Flux Transformer Effect (TFTE), the current is sent in the upper local wire, while voltage is measured *nonlocally* in the remote contacts at the lower cross. The dramatic difference between a conventional 4-point measurement and this connection scheme is that in case of a normal metal, this should not yield *any* measurable voltage as was shown in section 2.4.1. Even in the case of a superconductor, the observed voltage can only be explained by the transfer of vortices through the channel towards the nonlocal contacts.

Due to the extremely small signals on the order of 50 to $100\,\mathrm{nV}$ in these nonlocal

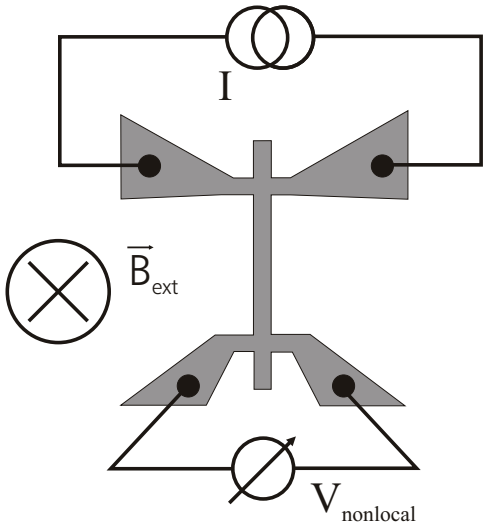

Figure 4.3: Schematic of the measurement setup for all nonlocal measurements, including time-dependent measurements: current is sent between the upper two contacts, while voltage is measured nonlocally between the remote lower contacts. Note that this setup should not yield a voltage when used with a normal metal.

measurements, careful grounding to avoid loops and noise pickup is essential. Since DC measurements have usually finite offset voltages ($\rightarrow$ thermopower) of around $1\,\mu\mathrm{V}$, all $E(j)$-curves were manually shifted to zero, i.e. such that $E(j=0) = 0\,\mathrm{V/m}$. On top of that, the noise level of roughly $50\,\mathrm{nV}$ was reduced by a factor of 2-3 by an adjacent averaging routine ($\pm$10 points).

4.3 Time-dependent measurements

One of the simplest cases for a measurement in the time domain is using current pulses to switch the driving force ON and OFF. A first successful attempt in that direction will be presented in chapter A. The time trace of the voltage signal was recorded by a digital storage oscilloscope (*Accura 100* from *Nicolet*), but the very limited sensitivity of such instruments in comparison to e.g. nanovoltmeters requires to use a more distinguished measurement scheme: box-car averaging. A short description of the technique can be found in appendix A.1, so the details will be skipped at this point. The general idea is to use averaging to improve the signal-to-noise ratio. But since this is a very time consuming process (e.g. 200000 averages were taken), it is still necessary to amplify the signal beforehand as much as possible. We used two amplifiers in series, an *Arstec*

LI-75A and a *Stanford Research Systems SR560*, which gave a total gain of 500000. This enabled us to measure the small signals of the nonlocal effect on the order of $50\,\mathrm{nV}$ after careful grounding. The sample connection scheme was the same as in figure 4.3.

Chapter 5

Sample properties

Any sample is first thoroughly characterized regarding the parameters transition temperature and upper critical field as a function of temperature, which (as shown in section 3.1.2) in combination with ρ_n (the normal state resistivity) suffice as input for calculating all other material parameters . This then builds the starting point for each measurement period, and even serves as criterion to help decide whether or not to use a specific sample for further measurements.

All results refer to the sample shown in figure 3.5, which was used exclusively for the studies presented in chapter 6. The measurement scheme was as described in section 4.1, i.e. a conventional 4-point measurement across the $L = 2\,\mu\mathrm{m}$ channel of width $W = 250\,\mathrm{nm}$.

5.1 Transition temperature

The very first step usually is a temperature sweep (after demagnetization of the magnet) while measuring the resistivity to determine T_c, as shown in figure 5.1. In this case, the sample shows a narrow transition of $\Delta T_c = 10\,\mathrm{mK}$ around $T_c = 2.94\,\mathrm{K}$. This was determined using the midpoint of the transition between 10 % and 90 % according to $T_c = \frac{1}{2}(T_{0.9} + T_{0.1})$, where T_x denotes the temperature at which the resistance $\rho(T_x) = x\rho_n$, with $\rho_n = (182 \pm 3)\,\mu\Omega\mathrm{cm}$. These values are both typical for the material and indicate a homogeneous composition. The measurement was done both AC and DC, yielding the same results. The graph shown stems from the AC measurement at a current of $I = 30\,\mathrm{nA}$ (or equivalently $j = 3\,\mathrm{MA/m^2}$) with a frequency of $f = 37.18\,\mathrm{Hz}$. This extremely small current density was chosen to minimize any effect of current on the measured T_c, which decreases with increasing current.

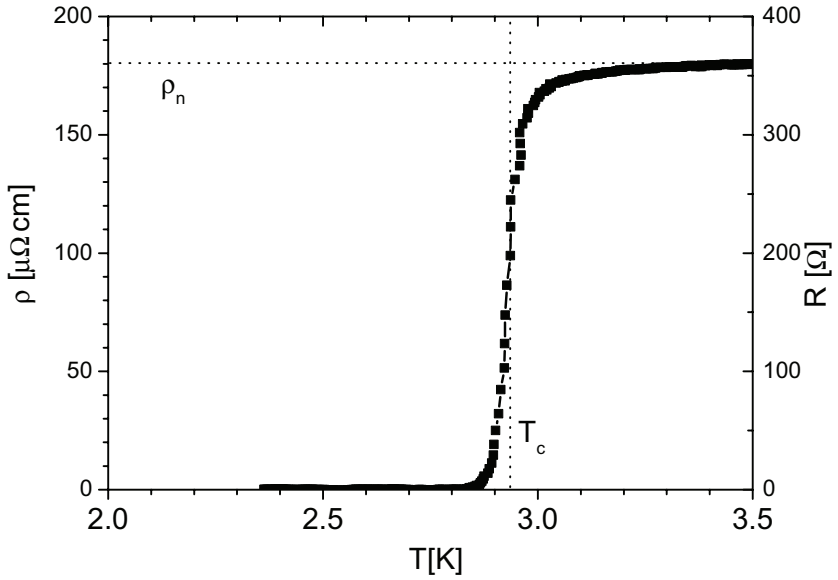

Figure 5.1: Determination of the transition temperature T_c from $\rho(T)$ (left y-axis). The horizontal dotted line indicates $\rho_n = 182\,\mu\Omega\mathrm{cm}$, the normal state resistivity, the vertical one $T_c = 2.94\,\mathrm{K}$, where $\Delta T_c = 10\,\mathrm{mK}$, and the corresponding measured value of R is shown on the right y-axis.

5.2 Upper critical field $B_{c2}(T)$

For determination of the temperature dependence of the upper critical field $B_{c2}(T)$, the same (AC) measurement setup as above was used. One example of the 16 different $R(B)$-curves taken at temperatures $0.3\,\mathrm{K} < T < 3.0\,\mathrm{K}$ is shown in figure 5.2. The current used ($I = 30\,\mathrm{nA}$ or $j = 3\,\mathrm{MA/m^2}$) was extremely low to avoid any nonequilibrium effects. The curve is very well symmetric around $B = 0\,\mathrm{T}$, but still the side where the material goes from the superconducting to the normal state was chosen for the evaluations. To extract the actual values for the respective $B_{c2}(T)$, two different methods have been used: (i) the intersection of linear fits to the steep increase (or in other, mathematically more precise words to the inflection point) and the asymptotic approach onto ρ_n on the one hand, and (ii) the magnetic field where $\rho(B) = 0.9\rho_n$ on the other hand (used e.g. in ref. [83]). As seen from the graph (dashed arrow), the agreement between the two methods is almost perfect. Another thing to be seen from the graph is that at low magnetic fields, the vortex motion is clearly hindered by stronger pinning sites first being populated before at intermediate fields vortices are free to move. This effect is reduced successively as temperature increases, since then obviously the

thermal energy helps to surmount the pinning forces.

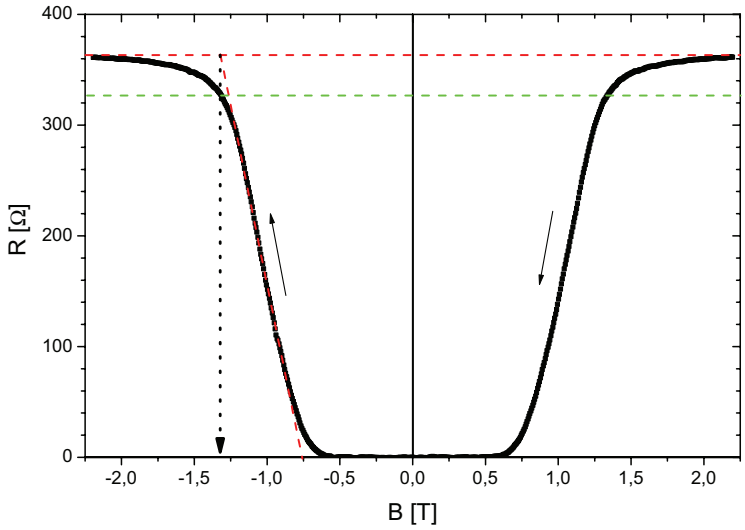

Figure 5.2: Exemplary $R(B)$-curve (AC) at a temperature of $T = 2.40\,\mathrm{K}$ and an applied current of $I = 30\,\mathrm{nA}$ or $j = 3\,\frac{\mathrm{MA}}{\mathrm{m}^2}$ to illustrate the two different methods used to extract the actual value of $B_{c2}(T)$: The intersection of the red dashed lines is one method which uses linear fits to the slope of the steep increase in magnetoresistance and the asymptotic approach onto ρ_n, whereas the green dashed line marks 90 % of ρ_n. The resulting value of $B_{c2}(T = 2.40\,\mathrm{K}) = 1.32\,\mathrm{T}$ is indicated by the dotted black arrow and agrees perfectly for both methods. Note that the curve is well symmetric around $B = 0$; the solid arrows show the sweep direction.

The result for both methods is plotted in figure 5.3 in cyan and blue respectively, together with a numerical evaluation of the theoretical formula (red) for $B_{c2}(T)$ from the theory of Werthammer-Helfand-Hohenberg (WHH) [84], which for the case of a thin film in perpendicular field is given by

$$\ln\left(\frac{T_c}{T_{c0}}\right) = \Psi\left(\frac{1}{2}\right) - \Psi\left(\frac{1}{2} + \frac{DeB_{c2}}{2\pi k_B T_c}\right) \quad , \tag{5.1}$$

where $D = 8k_B T_c \xi^2(0)/(e\Phi_0) = 4.8 \cdot 10^{-5}\,\mathrm{m}^2/\mathrm{s}$ is the diffusion constant, and $\Psi(z) = \Gamma'(z)/\Gamma(z)$ is the digamma function (see also Tinkham [17]). The agreement is good close to T_c and shows some significant deviations for lower temperatures. The enhancement of the upper critical field above the WHH-prediction at low temperatures may possibly be related to and explained by field-induced suppression of localization effects in

highly disordered films [85]. Such effects are expected for materials with $\rho_n > 100\,\mu\Omega\mathrm{cm}$, which is fulfilled for our films. A more rigorous analysis as for example in refs. [77, 86] may also provide better agreement at low temperatures, but seems a bit pedantic for our purposes, since we are mainly interested in the (negative) slope $\mathcal{S} = |dB_{c2}/dT|_{T=T_c}$ as discussed in section 3.1.2, for which the deviation at low temperatures is within 10 %. Additionally, according to the method and criteria given in refs. [77, 86], it involves high-resolution $E(j)$-curves (voltage resolution better than $1\,\mu\mathrm{V}$), which at least for our samples is not easily fulfilled due to the tiny dimensions compared to microbridges or even larger specimens. One could of course optimize the setup and sensitivity range of the nanovoltmeters (also used for the local $E(j)$) to better resolve the low current regions, but again, this was not the main focus of these experiments. DC voltage signals of less than $50\,\mathrm{nV}$ were successfully measured for the nonlocal curves, whereas the maximum signal of the local measurements is around $2\,\mathrm{mV}$. Even so, the extracted slope $\mathcal{S} = 2.3 \pm 0.1\,\mathrm{T/K}$ (green dotted line) agrees well with previous findings [16, 15].

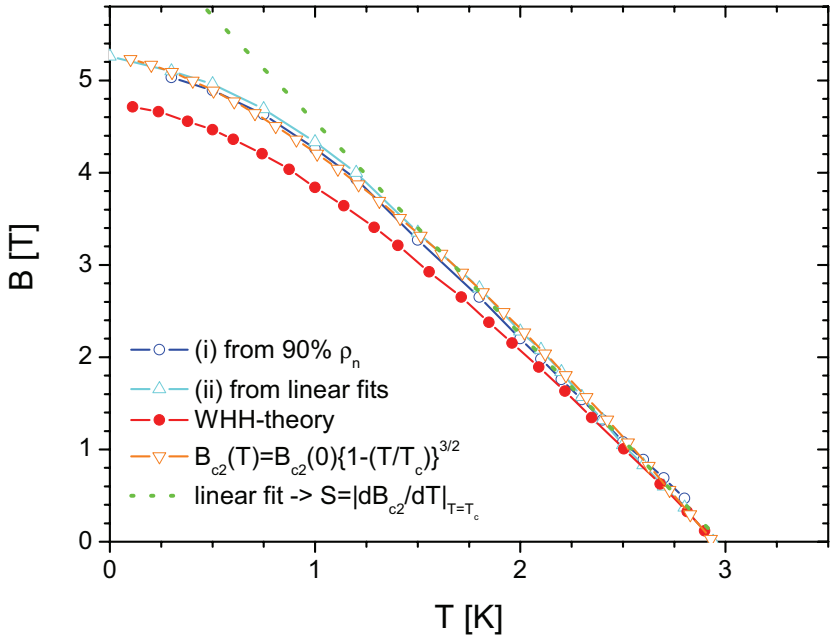

Figure 5.3: Temperature dependence of the upper critical field $B_{c2}(T)$. The graph shows data from two different methods (blue, cyan) used for extracting the respective value for each $R(B)$-curve, the curve according to the theory of Werthammer-Helfand-Hohenberg [84] (red) and an analytical fit function (orange) used to interpolate and invert the curve (see text for details). The dotted green line indicates the linear fit close to T_c which yields the slope $\mathcal{S} = |dB_{c2}/dT|_{T=T_c} = 2.3 \pm 0.1\,\mathrm{T/K}$.

Additionally, an analytical fit is shown in orange, found by manually adjusting the parameters $B_{c2}(0)$ and α in a fit formula of the type

$$B_{c2}(T) = B_{c2}(0)\left(1 - \frac{T}{T_c}\right)^{\alpha} \quad . \tag{5.2}$$

The curve shown was obtained for $B_{c2}(0) = 5.26\,\mathrm{T}$ and $\alpha = 3/2$. The agreement is quite good and justifies the use of this phenomenological formula as an interpolation for the inverted $T_c(B)$-curve, which will become important in chapter 6.1.1 when trying to obtain the heating temperature T^* from the extracted values of b^* of the local $E(j)$-curves (see section 2.3.3). Another thing worth noting is that this quite crude guess of the analytical form of $B_{c2}(T)$ does also yield a result almost indistinguishable from the numerical WHH-formula for the parameters $B_{c2}(0) = 4.7\,\mathrm{T}$ and $\alpha = 3/2$ (not shown).

5.3 Extracted material parameters

The above two measurements serve as the main input into the formulas for finding the material parameters as described in section 3.1.2. The results are summarized in table 5.1.

	κ	$\xi(0)$ [m]	$\lambda(0)$ [m]	$B_c(0)$ [T]	$N(0)$ [$\mathrm{J^{-1}m^{-3}}$]
expression	$(\rho_0\mathcal{S})^{1/2}$	$(T_c\mathcal{S})^{-1/2}$	$(\rho_0/T_c)^{1/2}$	$T_c(\mathcal{S}/\rho_0)^{1/2}$	$\mathcal{S}/\rho_0$
multiplier	3.54×10^{4}	1.81×10^{-8}	1.05×10^{-3}	1.15×10^{-5}	1.78×10^{41}
value	72	7.0×10^{-9}	825×10^{-9}	38×10^{-3}	2.25×10^{47}
error	± 2	$\pm 0.3 \times 10^{-9}$	$\pm 20 \times 10^{-9}$	$\pm 2 \times 10^{-3}$	$\pm 0.14 \times 10^{47}$

Table 5.1: Summary of determined material parameters using $\rho_0 = (1.82 \pm 0.03)\,\mu\Omega\mathrm{m}$, $\mathcal{S} = (2.3 \pm 0.1)\,\mathrm{T/K}$ *and* $T_c = (2.94 \pm 0.10)\,\mathrm{K}$.

The values found are perfectly within the expected ranges, indicating a sample of good quality despite the small dimensions.

Chapter 6

Nonlinear vortex transport

This chapter comprises the two main parts of the measurements: first, the vortex motion regimes are characterized and identified with the help of the nonlinear instability features in local voltage-current characteristics of our mesoscopic channel. This is done in complete analogy to section 2.3 and in the well understood two limiting cases, namely for temperatures close to and well below T_c, presented in section 6.1. The information obtained then builds the basis for the second class of experiments described in section 6.2, which focus on the current dependence of the TFTE in measurements of nonlocal IV-curves.

The vantage point for these investigations was an initial probe of the nonlocal response, tested as in the previous studies [11, 12] by magnetic field sweeps. The result of such an (AC) test run at a rather high current density of $j = 200\,\mathrm{MA/m^2}$ (or equivalently, $I = 2\,\mu\mathrm{A}$) is shown in figure 6.1. This corresponds to rather strong nonequilibrium, as will be discussed in some detail later in this chapter, but was chosen to get a quick overview map of the nonlocal signal in the B-T-plane by an easily resolved voltage signal. The first thing to notice is that at low temperatures, pinning seems to hinder the vortex motion up to considerably large fields, indicating significant pinning. At larger field values, and for higher temperatures, the nonlocal voltage displays the usual peak slightly below B_{c2} before it decays again when the sample approaches the normal state. As the temperature increases, the two peaks (symmetric in applied field since the two sign reversals in $\vec{f}_L = \vec{j} \times \vec{\Phi}_0$ and $\vec{E} = \vec{B} \times \vec{v}_\varphi$ cancel) start to overlap and finally merge for the highest temperature ($T = 2.70\,\mathrm{K}$) to one single peak centered around $B = 0$. This behavior is of course no surprise, since as described in section 2.4, the field of the peak in U_{nl} happens slightly below B_{c2} and thus essentially follows the temperature dependence of the upper critical field roughly. The offset (nonzero value) at high magnetic fields, which may either be related to the finite common mode rejection (CMR) of the instrument or thermovoltages, is independent of magnetic field and will be neglected in

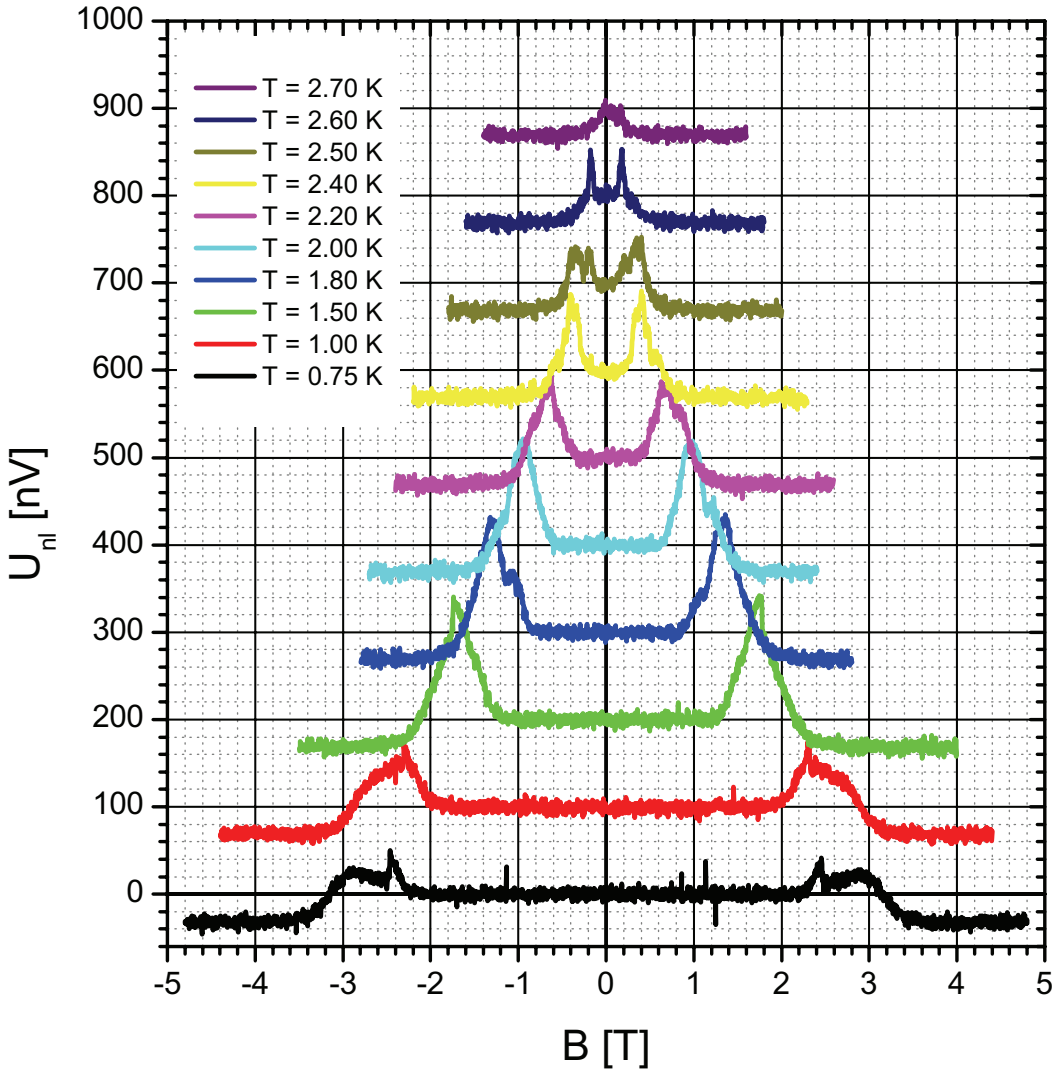

Figure 6.1: Initial AC test measurement of the nonlocal signal at a comparatively large applied current of $I = 2\,\mu\mathrm{A}$, which, as will be shown later, is already deep in the nonlinear regime. Still, this 'map' provides a useful overview and orientation for appropriate field values at the different temperatures and demonstrates that indeed, the TFTE is observable over most of the B-T-phase diagram. Note that the curves are offset for clarity by $100\,\mathrm{nV}$ *successively.*

what follows, since all other measurements of interest were performed DC, where offsets are compensated for by shifting the $U(I)$ to $U(I = 0) = 0$.

6.1 Local voltage-current characteristics

All local measurements were performed in the geometry shown in figure 4.2, using a DC voltage source (*Yokogawa 7651*) together with a series resistor of $1\,\mathrm{M}\Omega$ as the current input at a sweep rate of $4\,\mathrm{nA/s}$. While measurements were performed for both polarities, usually sweeping back and forth between current densities high enough to reach ρ_n, most graphs will only show the upsweep-branch, going from superconducting to normal. At each of the 9 different measurement temperatures, ranging from $T = 0.75\,\mathrm{K}$ to $T = 2.85\,\mathrm{K}$, different magnetic fields between zero and $B_{c2}(T)$ were used. In this way, almost the whole B-T-plane was covered, but the focus still remained on the regions where the largest nonlocal signal was seen, i.e. the magnetic fields around the peak of U_{nl} at each of the temperatures of interest, compare to figure 6.1. For reasons of brevity and in order to work out the main results, only the most typical curves at temperatures revealing the best agreement with the two limiting cases will be presented.

6.1.1 Low temperatures: electron heating regime

This subsection summarizes the findings for the local $E(j)$-curves taken at low temperatures. Although more data is in principle availabe at $T = 1.00\,\mathrm{K}$ and $1.50\,\mathrm{K}$, mainly data from the lowest measurement temperature of $T = 0.75\,\mathrm{K}$ are presented, since these yield the clearest results. The analysis takes the exact same route as for the measurements on microbridges, ref. [15, 16], described at length in section 2.3.3.

Local $E(j)$-curves at a temperature of $T = 0.75\,\mathrm{K}$ for magnetic fields between $2.00\,\mathrm{T} < B < 4.00\,\mathrm{T}$ are shown in figure 6.2. The curves for lower fields ($B = 0.5$, 1.0 and $1.5\,\mathrm{T}$) have been omitted to allow for a clearer presentation, since the corresponding FFI-jumps for those fields are at significantly higher values of j. This range and the enhanced field resolution were chosen specifically due to the fact that the nonlocal signal peaks around roughly $3\,\mathrm{T}$. The FFI-kink at $B = 2.00\,\mathrm{T}$ becomes smoother successively as the field is increased, in complete agreement with the measurements on the microbridges. One distinct difference between the two cases becomes immediately apparent when trying to fit the low current regions: in the lower right corner of the graph, the dotted line represents a fit for $B = 2.00\,\mathrm{T}$ in the low current region according to the LO-formula $j = j_c + 0.9\sigma_n E/b$, where $j_c = 158\,\mathrm{MA/m^2}$ is the only fit parameter (to be compared with figure 2.14 (a)). Clearly, there is poor agreement between the two curves. This can be attributed to the increased pinning strength in the mesoscopic channels used in this study, where the layer thickness is 40 instead of $20\,\mathrm{nm}$ for the microbridges, and the oversimplifications that are used in the derivation of the formula: it disregards individual hopping of vortices, plastic shear between vortex "columns" and all other real effects

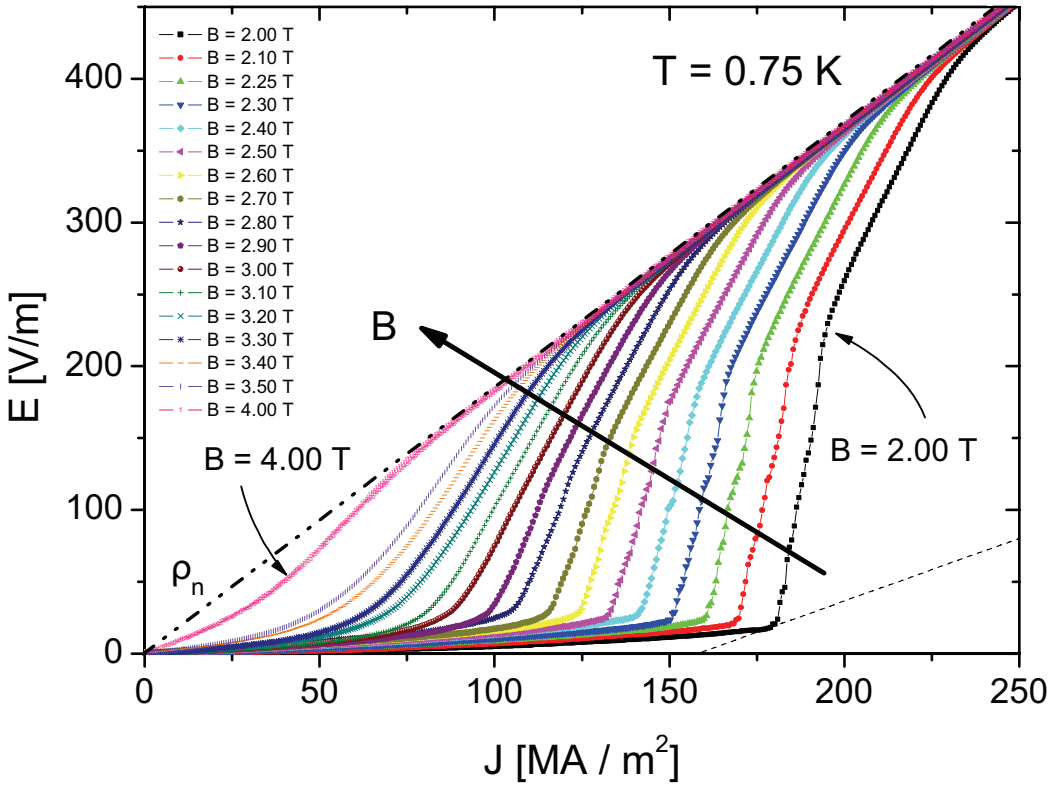

Figure 6.2: Local $E(j)$ for $2.0\,\mathrm{T} < B < 4.0\,\mathrm{T}$ at $T = 0.75\,\mathrm{K}$, which corresponds to $t = T/T_c = 0.26$. The critical field at this temperature is $B_{c2} = 4.69\,\mathrm{T}$. The dotted line in the lower right corner represents a fit for $B = 2.00\,\mathrm{T}$ in the low current region according to $j = j_c + 0.9\sigma_n E/b$, where $j_c = 158\,\mathrm{MA/m^2}$ is the only fit parameter (to be compared with figure 2.14 (a)). Quite obviously, the pinning in these samples is much stronger than in the case of the microbridges, leading to vortex hopping motion at low currents, which inhibits agreement with the LO-formula.

related to pinning. It furthermore assumes that the entire lattice moves collectively in a flow against a constant pinning force $f_p = j_c\Phi_0$. Vortex entry/exit conditions in realistic mesoscopic samples may as well introduce additional effects in comparison to wider microbridges, as they are relevant in only a narrow region (when compared to the sample width) close to the sample edges [87]. These issues are of little relevance for the central topic of this thesis.

What is more important is that we can again use the local $E(j)$-curves to extract the nonequilibrium values of $b^* = B/B_{c2}(E)$ by recalling figure 2.13 and the discussion following eq. 2.59. The resulting $b^*(E) = 1 - (1/\alpha)[j/(\sigma_n E) - 1]$ from the measured values of E and j, and for $\alpha = 3$ can similarly be collapsed onto a universal curve when

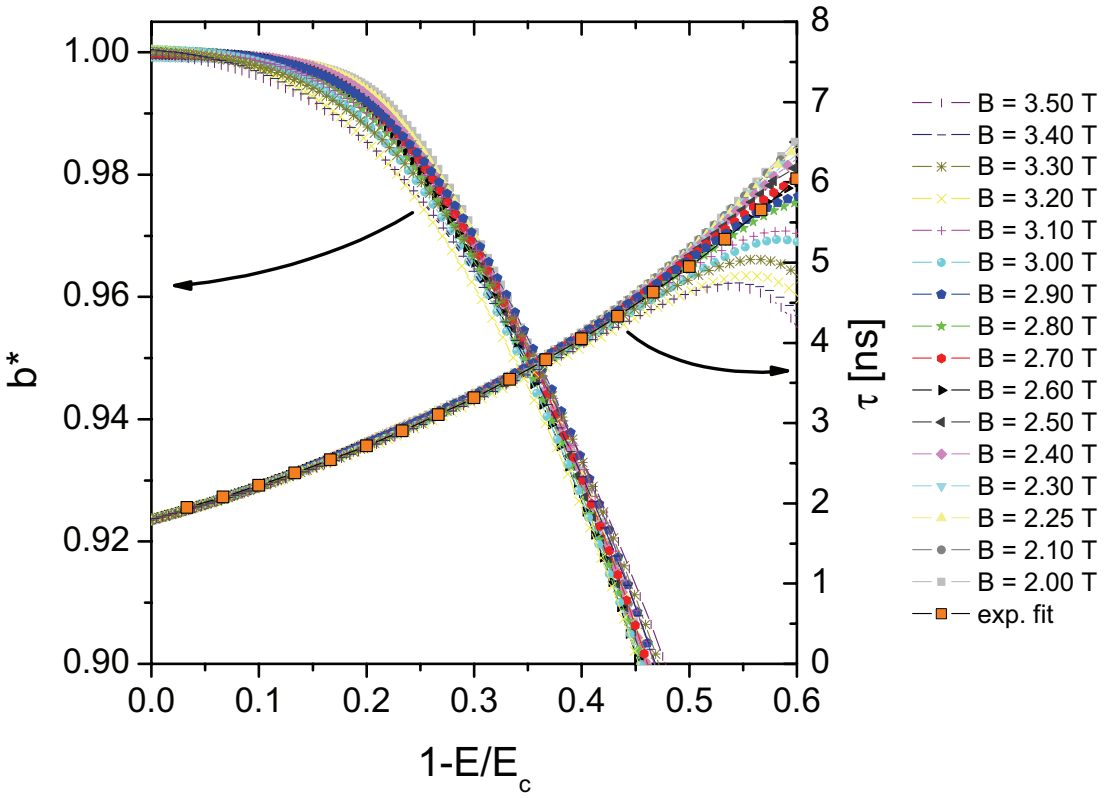

Figure 6.3: Scaling plot of the nonequilibrium reduced magnetic field $b^* = B/B_{c2}(T^*)$ (left-hand scale) and the quasiparticle scattering time τ (right-hand scale) vs. $1 - E/E_c$, as indicated by the arrows and calculated as explained in the text. The orange squares represent $\tau = \tau_0 \exp[2(1 - E/E_c)]$ with $\tau_0 = 1.82\,\mathrm{ns}$ (to be compared with figure 2.15).

plotted versus $1 - E/E_c$ with the appropriate scaling values E_c. This can be seen in figure 6.3 for $0.9 < b^* < 1.0$, where $\alpha(T) \approx \mathrm{const.}$ and the validity of this approach are expected (see eq. 2.54). The scaling works very well for $2.00\,\mathrm{T} < B < 3.50\,\mathrm{T}$, and at the same time, the corresponding E_c scale nicely linearly as expected in the same range, before deviations for smaller as well as higher fields occur. This is shown in the inset of figure 6.4: $E_c(B) = E_{c0}(1 - b)$ with $E_{c0} \approx 900\,\mathrm{V/m}$. Since the temperature here is lower than in figure 6.4, it is to be expected that also E_{c0} is smaller, because it implies a larger relaxation time at lower temperature, which is reasonable, see below.

The next step is using the B-T-phase diagram together with the inferred values of $b^*(E)$ to reconstruct the corresponding heating temperatures $T^*(E)$, which is shown for some exemplary fields in figure 6.4. While strictly speaking, the approach is only valid for

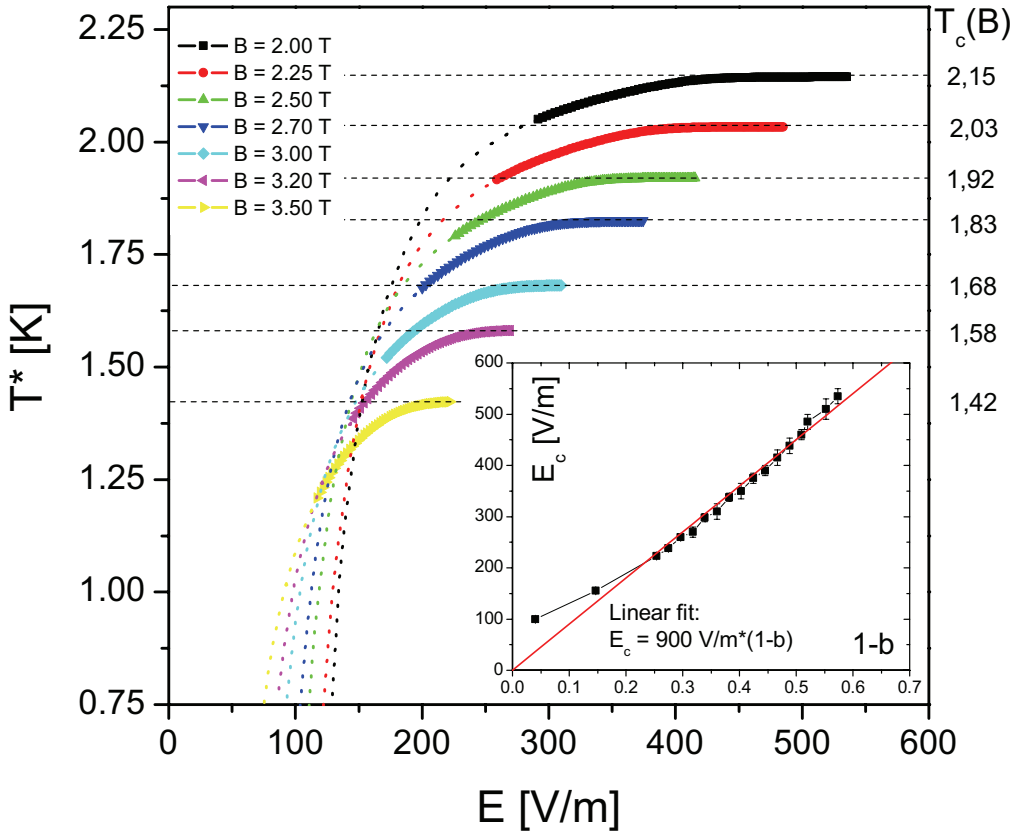

Figure 6.4: Extracted effective electron temperatures T^* for seven different magnetic fields as estimated from the equilibrium $B_{c2}(T)$ characteristics. The dashed lines represent $T_c(B)$, which is in addition written next to the graph on the right for each field (to be compared with figure 2.15 (b)). Inset: E_c against equilibrium $1-b$ (to be compared with inset of figure 2.15 (a)).

$0.9 < b^* < 1.0$, which leads to the curves for T^* plotted with the filled colour symbols, it makes some sense to expand the analysis to lower electric fields (i.e. lower currents in the $E(j)$-curve), since one can see that in the restricted range, the heating starts from an offset value above the bath temperature $T_0 = 0.75\,\mathrm{K}$. Lacking any other meaningful picture or mechanism, it is justified rather well to assume that this 'gap' is bridged also by the electron heating. Besides, the scaling of b^* vs. $1-E/E_c$ works rather well also for $b^* < 0.9$, where the assumptions made during the derivation are not fulfilled as perfectly as above that value. This region is indicated by the dotted colour lines extending the

better justified values of T^*. The corresponding phase boundaries, where the electron heating temperature T^* reaches the critical temperature $T_c(B)$ of the applied magnetic field, are represented by the horizontal dashed lines, with the values for the respective $T_c(B)$ written next to the graph on the right side. Upon reaching this point, the normal state and thus $j = \sigma_n E$ is recovered, and one may ask what happens then: does the applied current also produce heating effects in the normal wire? This question will be addressed in slightly more detail with the help of noise measurements in section 6.2.1, when the effect of the heating on the nonlocal voltage will be discussed.
The last part completing the procedure is the extraction of the relaxation time $\tau = [G_s(T_0) - G_s(T^*)]/(jE)$, using the measured $E(j)$ and $G_s(T_0) = \sigma_n E_c^2(B)\tau_0$ instead of $G_s \approx U_s(1-b)^2$ (as in section 2.3.3 and ref. [15]), where $E_c(B)$ equals the value extracted from the scaling of b^*. This way one can avoid problems with the approximation $G_s \approx U_s(1-b)^2$, the validity of which diminishes as b decreases. Instead, one uses G_s without predicting its dependence on b. Note that there is no such problem with $G_s(T^*)$, as in this case b^* is close to unity and the above approximation should be almost exact [87]. The obtained curves display a very satisfying scaling behavior for electric fields roughly of the order of the validity of the scaling of b^*, see figure 6.3. The collapsed curve is well described by a fit formula of the form

$$\tau(E, B) = \tau_0 \exp[a(1 - E/E_c)^c] \tag{6.1}$$

with $\tau_0 = 1.82\,\mathrm{ns}$, $a = 2$, $c = 1$ and the corresponding values of E_c. The same analysis has been performed for $T = 1.00$ and $1.50\,\mathrm{K}$; a summary of the values found is given in table 6.1.
While the numbers for E_{c0} and τ_0 roughly agree with those of ref. [15], the functional form of $\tau(E, B)$ remains unclear: in the case of the microbridges, the exponent $c = 3/2$,

T [K]	E_{c0} [V/m]	τ_0 [ns]	a	c
0.75	900	1.82	2.0	1.0
1.00	1050	1.12	2.18	1.0
1.50	1480	0.33	2.70	1.1

Table 6.1: Summary of determined parameters for the electron heating model in case of $T = 0.75$, 1.00 and $1.50\,\mathrm{K}$.

and $a = 3.5$, whereas the lowest two temperatures used for the mesoscopic channels suggest $c = 1.0$ and a close to 2. On the other hand, given the imperfectness of the current samples for investigations centered around these issues, one should repeat similar measurements with microbridges and probably at even lower temperatures for a clearer picture.

Altogether, the overall agreement with the results on microbridges strongly suggests the applicability of the electron heating model also for the mesoscopic channels, which will be a good starting point for the interpretation of the nonlocal measurements.

6.1.2 High temperatures: vortex-core shrinking regime

Also the regime of temperatures close to T_c has been studied extensively in terms of local $E(j)$-curves, in complete analogy to ref. [15, 16] and section 2.3.3.

Measurements at $T = 2.50\,\mathrm{K}$ ($t = T/T_c = 0.85$) are shown in figure 6.5. The curves for the lowest magnetic fields display slightly 'nervous' switching in the region around the FFI, but other than that, the $E(j)$-curves are as expected, with the transition region getting smoother as the magnetic field increases.
Recalling eq. 2.56,

$$j = \sigma_n \left[A + \frac{g(b)}{b\sqrt{1-t}} \frac{1}{1+(E/E_i)^2} \right] E \quad , \tag{6.2}$$

we can try to fit the measured $E(j)$ by inserting the appropriate values for $g(b)$ (note: different functions for $b < 0.315$ and $b > 0.315$, see comments after eq. 2.55), b and t, with the fit parameters being E_i and A. The latter should be close to 1 at least for high enough electric fields and accounts for the suppression of the order parameter outside the vortex cores by the 'evaporated' quasiparticles (see also ref. [83]). In figure 6.6, the result of fits to the $E(j)$ for $b = 0.10$ and 0.65 are shown: in order to account for the slope at high applied current densities, A was fixed to 0.98. While this upper part is described well by the theoretical curve, the agreement for small currents is again rather poor, most likely due to the higher pinning than in the microbridges and for the same reasons as in the case of low temperatures. On the other hand, the region of the negative differential conductivity in case of low magnetic field (figure 6.6 (a)) and thus the actual jump seems to be captured reasonably well, which leads to a satisfying linear dependence of the corresponding instability fields E_i versus b shown in figure 6.7.
The slope of the linear fit yields the critical vortex velocity $u_i = E_i/B = 205\,\mathrm{m/s}$, which

can be used in conjunction with the LO expression

$$u_i^2 = D\frac{\sqrt{14\zeta(3)}\sqrt{(1-T/T_c)}}{\pi\tau_{e,ph}} \quad . \tag{6.3}$$

to calculate the electron-phonon relaxation time $\tau_{e,ph} = 0.58\,\mathrm{ns}$. For this,

$$D = 8k_B T_c \xi^2(0)/(e\Phi_0) = 4.802 \cdot 10^{-5}\,\mathrm{m}^2/\mathrm{s} \tag{6.4}$$

and $\zeta(3) = 1.20206$ have been used. The actual energy relaxation time at low temperatures is larger by a factor $1/\sqrt{1-t}$, which yields $\tau_E \approx 1.50\,\mathrm{ns}$ (see also section 2.3.3 and refs. [15, 16]). The corresponding energy relaxation length $\ell_E = \sqrt{D\tau_E} = 268\,\mathrm{nm}$, which is roughly equal to the sample width $W = 250\,\mathrm{nm}$. This is an indication towards a necessity for a modification of the LO-formula, which is intended to work for the case $W \ll L_E$. Namely, we can estimate the time-of-flight of vortices across the channel

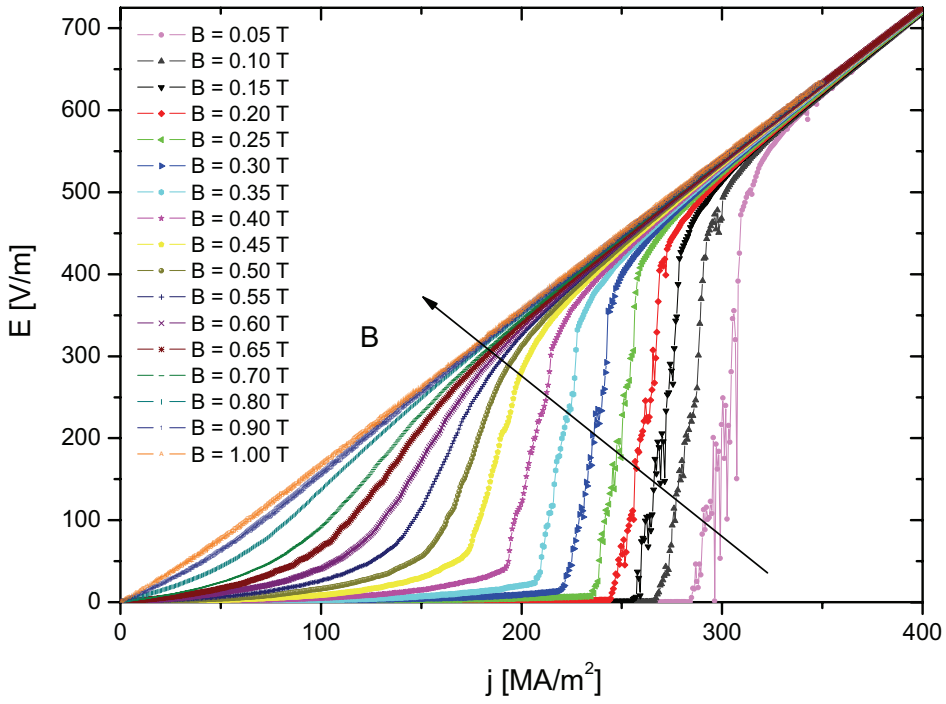

Figure 6.5: Local $E(j)$ for $0.05\,\mathrm{T} < B < 1.0\,\mathrm{T} = B_{c2}(T)$ at $T = 2.50\,\mathrm{K}$ (to be compared with figure 2.12), which corresponds to $t = T/T_c = 0.85$. Again, one can clearly see that the pinning in these samples is much stronger than in the case of the microbridges, see also figure 2.12. The critical field at this temperature is $B_{c2} = 1.0\,\mathrm{T}$.

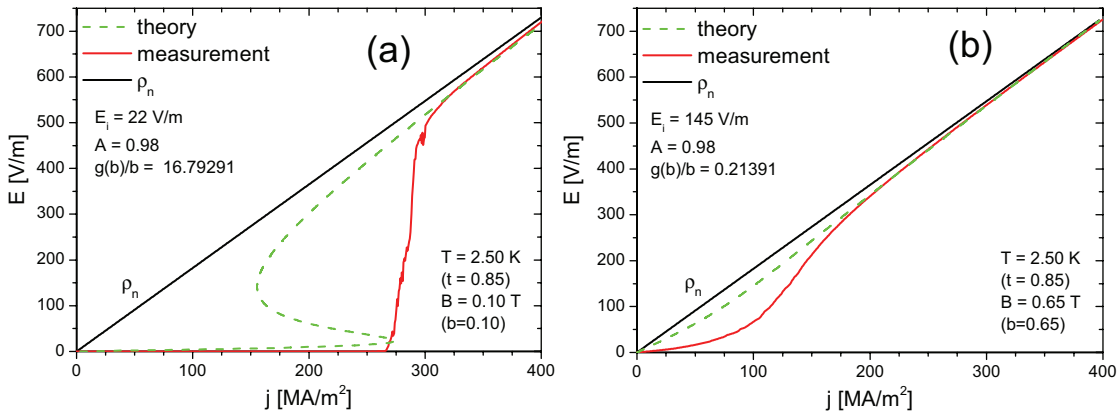

Figure 6.6: Local $E(j)$ at $T = 2.50\,\mathrm{K}$ for (a) $B = 0.10\,\mathrm{T}$ (or $b = 0.10$) and (b) $B = 0.65\,\mathrm{T}$ (or $b = 0.65$) together with fits according to eq. 6.2 (to be compared with figure 2.12). While the high-current part and the jump due to the onset of the negative differential conductivity are captured well, the theoretical formula fails to describe the low-current regions mainly due to the higher pinning than in the microbridges of ref. [15].

width to be $t = W/u_i = 1.2\,\mathrm{ns}$, which is slightly smaller than the energy relaxation time. Since the LO-theory treats the problem in terms of considering a single vortex (or a circular volume roughly corresponding to the primitive Wigner-Seitz cell) as a representative of a periodic lattice, in our restricted geometry the question arises which vortex to choose: one close to the edge or one in the center? Quite obviously, there is a certain timescale associated with the establishment of nonequilibrium. But this can for example just mean that less quasiparticles can escape the core region in the reduced time-of-flight. And since the extracted $E_i(B)$ are very well linear beyond any doubt (in stark contrast to temperatures well below T_c) despite the uncertainty about the applicability of the LO-expressions in their analytically exact forms, it seems more than reasonable to assume that the vortex-core shrinking is the underlying mechanism of the strong nonequilibrium close to T_c. This is further supported by experiments on wider samples of a-NbGe, where it was shown that the core-shrinking was always the origin of the strong nonequilibrium close to the transition temperature [87, 88]. The remarkable difference in the observed nonlocal voltages between data at high and low temperatures to be presented in the following sections provides another independent proof of this conclusion.

For our purposes, it should be sufficient to note that there are some deviations from the LO-theory, but the overall findings, including other data at temperatures even closer to T_c, strongly support the picture of the vortex-core shrinking.

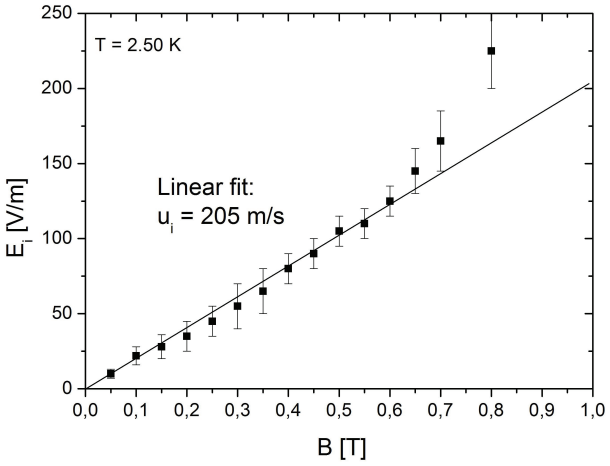

Figure 6.7: Although the fits in figure 6.6 reveal satisfying agreement between theory and experiment only for the high-current parts of $E(j)$, the extracted instability field E_i scales linearly with applied magnetic field $b = B/B_{c2}$ reasonably well for fields even larger than $b = 0.4$, the predicted upper limit in ref. [58] in agreement with the microbridge experiments [15] (see inset of figure 2.12 (b)). The scaling allows for the determination of the critical vortex velocity $u_i = E_i/B = 205\,\mathrm{m/s}$ given by the slope of the linear fit.

Remark: it was also tried to analyze the $E(j)$ at temperatures close to T_c in terms of the electron heating model, but no scaling behavior, neither for b^* nor for τ, could be achieved. Besides, the extracted critical fields E_c displayed a considerable offset when plotted versus $1 - b$ (compare to inset of figure 6.4: $E_c(1 - b = 0) = 0$).

6.2 Nonlocal voltage-current characteristics

As already announced in section 2.4.1, the main purpose of this work was the investigation of the current dependence of the TFTE directly in nonlocal DC IV-curves, the result of which are presented in this section. All measurements were done using the nonlocal setup shown in figure 4.3, with current defined by using a DC voltage source (*Yokogawa 7651*) together with a series resistor of $1\,\mathrm{M}\Omega$, swept at a rate of $4\,\mathrm{nA/s}$, while the nonlocal voltage was measured with a nanovoltmeter (*Agilent 34420A*). As usual in the case of DC measurements, finite offset voltages are always present, but could be minimized to roughly $1\,\mu\mathrm{V}$. Since no voltage is expected in case of zero applied current, all curves were shifted to $V(I=0)=0$. As mentioned in section 4.2, the noise level of roughly $50\,\mathrm{nV}$ was reduced by a factor of 2-3 by an adjacent averaging routine ($\pm$10 points). A comparison of smoothing with different parameters and routines is shown in figure 6.8. A Python script with different number of points for the adjacent averaging yields very similar results to the Origin routine, with best reproduction of the measured curve (while still decreasing the noise level significantly) at ± 10 points. Even the sharp fall after the peak at roughly $I = 2\,\mu\mathrm{A}$ is reproduced without any distortions of the original signal. The reason for using the Python script instead of Origin's built-in option is the speedier programming and ease-of-use when handling several hundred curves at once.

As in the case of the local $E(j)$, large parts of the whole B-T-plane were covered during the measurements, but the analysis presented here centers around the two limiting cases, where the local curves exhibit the well-known FFI features explained in the framework of either vortex-core shrinking (high T) or electron heating (low T).
It is found that the nonlocal voltage displays distinctly different behavior in these two limits, which are explained in terms of the pressure model for the TFTE, with the modification that different driving forces as the main input into the model govern the behavior: as previously observed, at low current densities, the TFTE can be interpreted in terms of the action of the Lorentz force, whereas at higher current densities, where nonequilibrium effects start to dominate, the Lorentz force is replaced by the thermal force (Nernst effect due to local electron heating) for $T \ll T_c$, and by a force due to the local suppression of the superconducting gap / the order parameter for T close to T_c.

6.2.1 Low temperatures: Lorentz force vs. Nernst effect

First, let us discuss the data at temperatures well below the transition temperature T_c. In the preceding section, the electron heating regime was confirmed with the help of local $E(j)$, which allows us to use the results obtained there in order to understand the features of the nonlocal data.

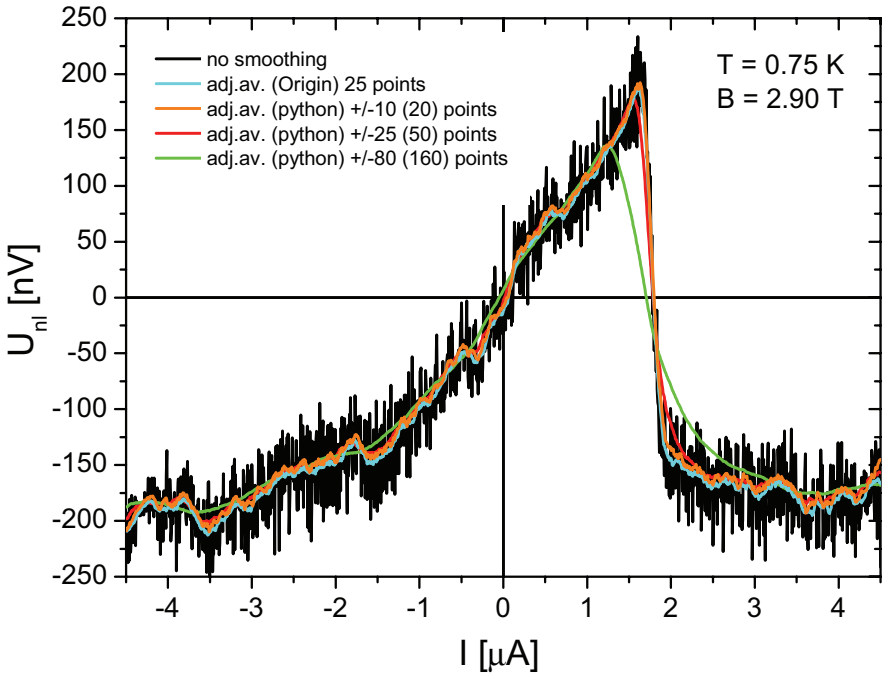

Figure 6.8: Comparison of different digital filtering methods using adjacent averaging for different number of points and two different routines: the easily programmable Python script yields almost identical results to the rather user-unfriendly Origin routine, with the best performance in terms of combined noise reduction and measurement reproduction for ±10 points. The curve shows the DC nonlocal $V(I)$ at $T = 0.75\,\mathrm{K}$ and $B = 2.90\,\mathrm{T}$.

Nonlocal voltage-current characteristics at the lowest measurement temperature of $T = 0.75\,\mathrm{K}$ are shown in figure 6.9 for magnetic fields $2.00\,\mathrm{T} < B < 3.50\,\mathrm{T}$, which corresponds to the region around the peak of the nonlocal signal observed in the AC magnetic field sweep test measurements (see figure 6.1). All curves have been offset by arbitrary amounts for clarity.

If for a moment we just concentrate on the low-current part of the curves, say roughly in between $-1.0\,\mu\mathrm{A}$ and $+1.0\,\mu\mathrm{A}$, very clearly the signal is rather asymmetric in applied current and displays a (close to) linear behavior. At the same time, the slope of this linear part starts from zero at $B = 2.00\,\mathrm{T}$, increases monotonically up to roughly $B = 3.00\,\mathrm{T}$, and then decreases again towards zero for higher fields ($B = 4.00\,\mathrm{T}$, not shown). This perfectly mimics the behavior seen in the magnetic field sweep measurements, that (except for our quick overview 'map' in figure 6.1) were typically all done for low current

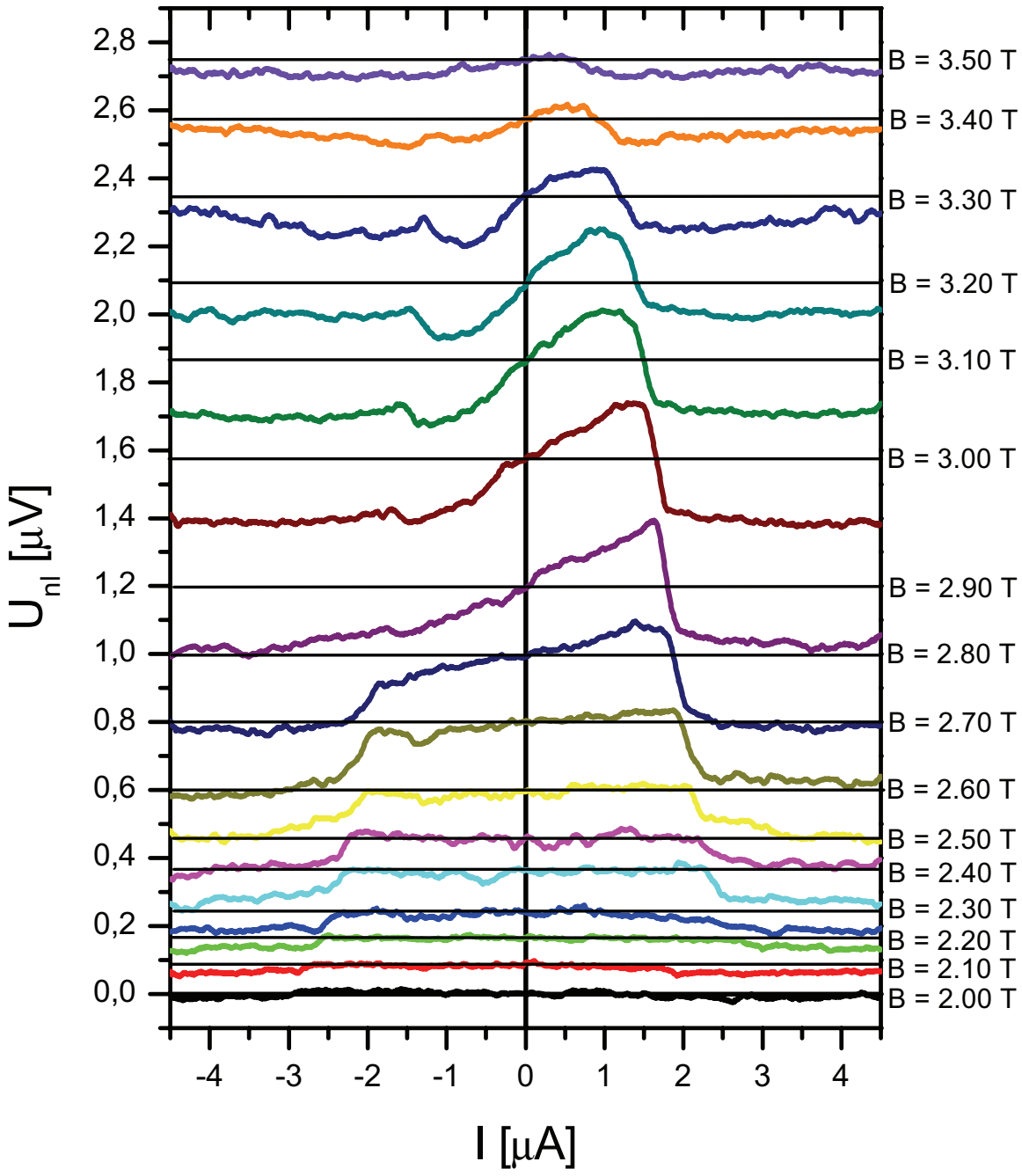

Figure 6.9: Nonlocal $V(I)$-curves at $T = 0.75\,\mathrm{K}$ for the fields indicated next to the graph, representing the region of the peak in the nonlocal signal observed in magnetic field sweeps. Curves have been offset for clarity by arbitrary amounts.

densities in order to safely avoid the nonlinearities (see figure 2.19 and refs. [11, 12, 13]). Accordingly, this part of the signal is well described by the pressure model introduced in section 2.4.1: all vortices in the upper cross (or correspondingly the volume $W^2 d$) encounter a Lorentz force due to the applied transport current, which exerts a pressure on the cross-sectional area of the channel. This pressure leads to a very efficient transfer of the vortex chain all the way down to the lower cross, where the nonlocal voltage is measured, with a linear dependence on the applied current according to

$$V_{nl} = \frac{\Phi_0 W B}{\eta L d} I \quad . \tag{6.5}$$

So far, this is nothing new and just completely confirms the previous findings. But it is worth noting that these findings are already a hint at surface pinning being the possible origin of the lateral confinement of the vortices in the channel: Comparing the two different geometries used for the local (4-point) and the nonlocal measurements (compare to figures 4.2 & 4.3), we realize that in the first case, current flows through the channel, which yields vortex motion perpendicular to the channel length, and current flow perpendicular to the channel direction, which means that vortices move along the channel. At the same time, we note that in the local case, a strong pinning is observed, see local $E(j)$, figure 6.2 (but also for example figure 6.6 (a) at high temperatures), which leads to a strong suppression of the local voltage for low currents, while the nonlocal voltage not only becomes finite as soon as the current is larger than zero, but also does so without any distortions or deviations from the linear behavior. This indicates different pinning strengths in the two different directions, which means that the surface of the channel serves as a confinement potential in the lateral direction via enhanced surface pinning. This further justifies our simple picture of the momentum transfer via the pressure model.

Now turning to the high-current parts (see figure 6.8 for a zoom of the $B = 2.90\,\mathrm{T}$-curve) something very spectacular happens on the side of positive currents at around $I = +2\,\mu\mathrm{A}$: although the driving force for the given geometry (magnetic field pointing into the sample plane, current sent from left to right, check figure 4.3) pulls vortices up towards the local current-carrying wire, and is expected to increase even further as the current is raised, the nonlocal voltage very suddenly encounters an abrupt sign change. This can only mean that the vortices inside the channel completely reversed their direction of motion, now suddenly moving towards the nonlocal lower cross.

At first sight, this seems a very puzzling and confusing observation. But with our knowledge about the electron heating regime expected at this temperature for large currents, a simple explanation seems possible: the main consequence of the nonequilibrium state in this regime is the heating of the electron system to an elevated temperature $T^*(E)$

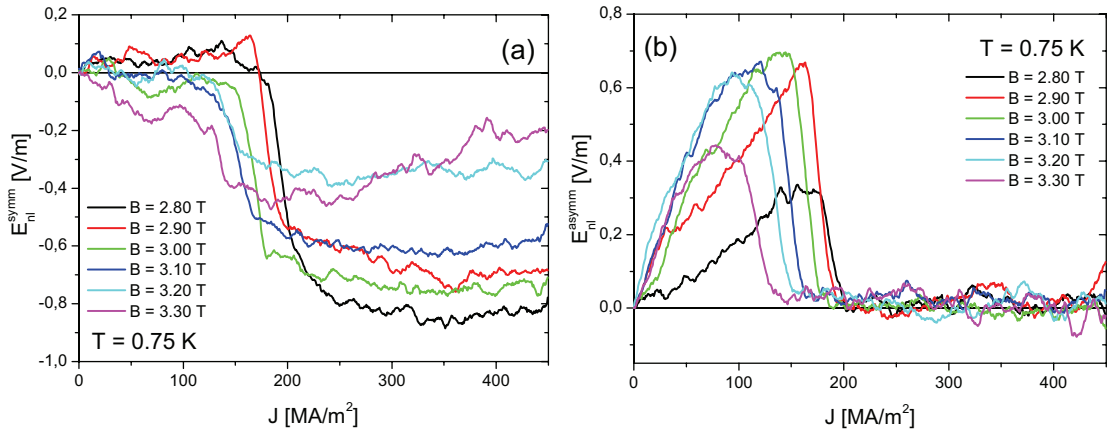

Figure 6.10: Symmetric (a) and asymmetric (b) parts of the nonlocal signal at $T = 0.75\,\mathrm{K}$ as described in the text for the magnetic fields around the highest efficiency of the effect.

above the bath temperature T_0. Since, as demonstrated earlier, the applied transport current is restricted to the local horizontal wire, it should be possible to generate a temperature gradient between the local and nonlocal parts of the sample. And if there were such a gradient, it would immediately imply the existence of a thermal force, which always points down the temperature gradient, i.e. from hot to cold.

To check if this is true, let us first think about the symmetry in this case: since the quasiparticles in the local wire will not care whether they are heated due to a current flowing from left to right, or right to left, this effect should yield the same temperature gradient irrespective of current direction. Indeed, we see from figure 6.9 that the response for high currents is very well symmetric.

This suggests to divide the nonlocal signal into symmetric and asymmetric parts according to

$$E_{nl}^{symm,asymm}(j) = \frac{1}{2}\left(E(j) \pm E(-j)\right) \quad , \tag{6.6}$$

where we have switched to the geometry independent notation of $E(j)$ instead of $V(I)$. The resulting $E_{nl}^{symm,asymm}(j)$ should reveal the action of the thermal force and the Lorentz force in the symmetric and asymmetric parts respectively. This is shown in figure 6.10 for several fields around the efficiency maximum.

The plots indeed support the above picture very well: while at low currents, the nonlocal signal is purely asymmetric and linear in applied current, implying the action of the Lorentz force, the high current data shows an almost purely symmetric response in

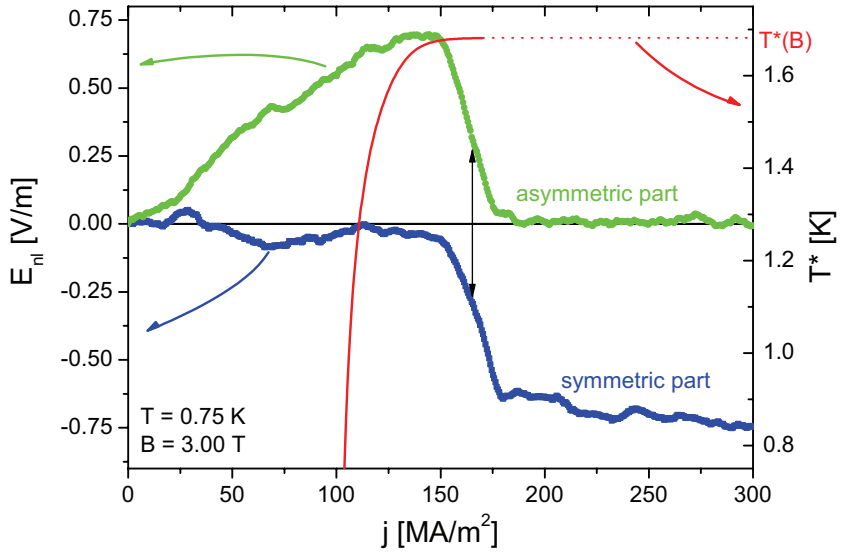

Figure 6.11: Symmetric and asymmetric parts of the nonlocal signal (left scale) at $B = 3.00\,\mathrm{T}$ together with the electron heating temperature T^* (right scale) as a function of applied current density j. The arrow in the center indicates the current at which $E_{nl}^{symm} = E_{nl}^{asymm}$.

accordance with the action of a thermal force. To further illustrate what is happening in more detail, figure 6.11 shows both parts, symmetric and asymmetric, together with the corresponding heating temperature T^* as a function of applied current.

What is particularly nice about this graph is that it reveals why exactly there is the pure Lorentz force response at low current densities: the heating does not start until the current density exceeds $100\,\mathrm{MA/m^2}$ (or correspondingly $I = 1\,\mu\mathrm{A}$). The fact that it kicks in very steeply and quickly saturates on the other hand explains the abrupt sign reversal of the nonlocal voltage. After the electron heating temperature reaches $T_c(B)$, the Lorentz force dies out completely, and so does the asymmetric part of the nonlocal signal for high currents, since the current-carrying wire has become fully normal conducting. This coincidence is shown for several different fields in figure 6.12 in terms of the typical current values at which this happens. While the extracted currents for the maximum in the asymmetric signal, half the maximum, the current at which it roughly goes to zero and the current where both parts of the nonlocal signal are equal display some spread due to the limited resolution, the current at which the phase boundary at $T_c(B)$ is reached lies well within these limits, indicated by the shaded area. This strongly supports our qualitative explanation of the observed sign reversal.

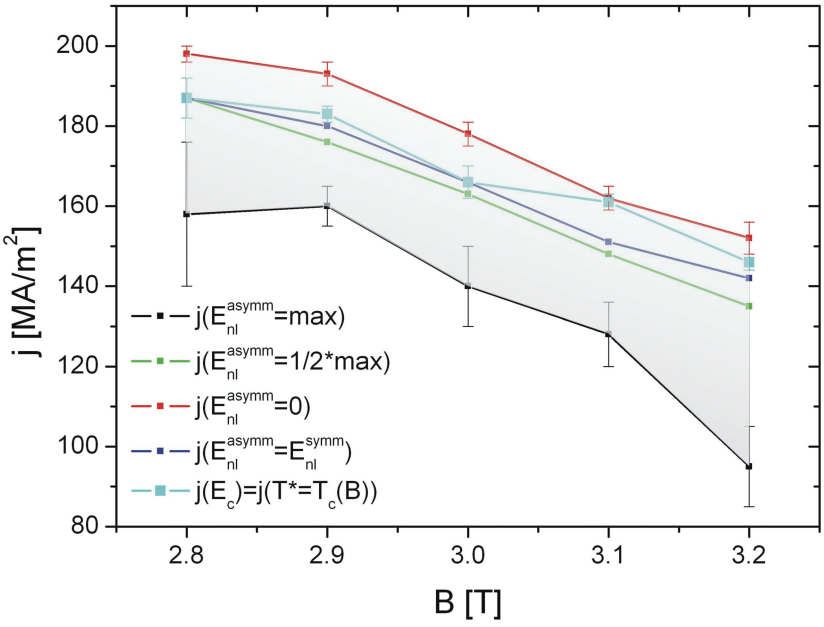

Figure 6.12: Current values of prominent features in the symmetrized nonlocal signals at $T = 0.75\,\mathrm{K}$ as a function of magnetic field: the current at which $T^* = T_c(B)$ stays well within the crossover region set by the maximum of E_{nl}^{asymm} and the approach to zero thereafter.

Determination of the transport entropy

To further quantify this, we can use the pressure model derived in case of the Lorentz force as the driving mechanism, and adopt it to match the case of the thermal force. In complete analogy to section 2.4.1, at vortex density $n_\Phi = B/\Phi_0$, a number of $n_\Phi W L_T$ vortices in the local wire encounter a thermal force of $dS_\phi \mathrm{grad}T = dS_\phi \Delta T/L_T$, thus applying a pressure of

$$p = \frac{n_\Phi W L_T dS_\phi \Delta T}{L_T W d} = n_\Phi S_\phi \Delta T \tag{6.7}$$

to the vortices in the channel. Here, L_T is the effective length over which T varies, and is thus defined via $\mathrm{grad}(T) = (T_0 - T^*(E_c))/L_T$ (see figure 6.13). At this point, the thermal length L_T drops out, which makes the expected nonlocal voltage independent of L_T.

The corresponding pushing force per unit length $f_L = pA/d = pWd/d = pW$ is balanced by the force required to move $n_\Phi LW$ vortices in the channel against the frictional damping ηv_φ per vortex (where v_φ is the vortex velocity in the channel and η in the channel should be independent of the heating in the local wire, i.e. the channel proper-

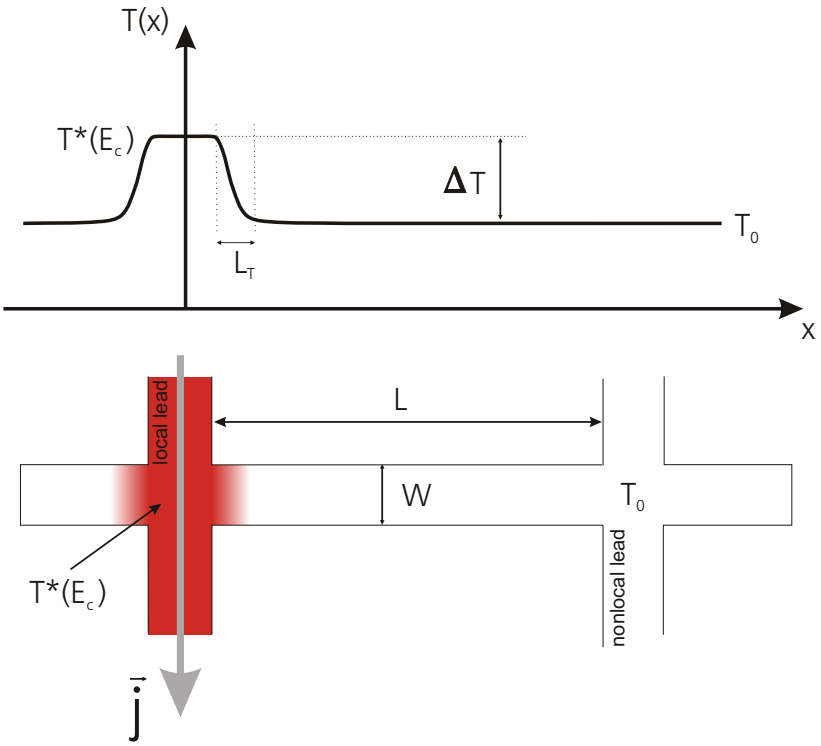

Figure 6.13: Schematic of the temperature gradient evolving between the local part of the sample and the channel / the remote nonlocal contacts.

ties stay the same irrespective of the driving force in the local cross). One can argue now whether or not to consider the effective length, that has to be moved, i.e. the channel length $L+X$, where X is the length of the tails (including the length of the lower cross). But we think that this can only be a small correction and that the vortices will rather leave sideways, towards the contact pads, and find their way out somewhere at a weak spot along the way. I will come back to this point below. The above yields

$$n_\Phi S_\phi \Delta T W = n_\Phi L W \eta v_\varphi \Leftrightarrow v_\varphi = \frac{S_\phi \Delta T}{\eta L} \quad . \tag{6.8}$$

Using $V_{nl} = WBv_\varphi$, we arrive at

$$V_{nl} = \frac{WBS_\phi \Delta T}{\eta L} = \frac{WBS_\phi \Delta T}{\eta L}\frac{d\Phi_0}{d\Phi_0} = \frac{WB\Phi_0}{L\eta d}\frac{dS_\phi \Delta T}{\Phi_0} = R_{nl}^{\mathrm{Lorentz}}\frac{d}{\Phi_0}S_\phi \Delta T \quad . \tag{6.9}$$

This approach justifies the use of R_{nl}, which can be taken as the linear part around zero current. The question of the effective length of the vortex train that has to be pushed

forward (i.e. with or without tail) is also automatically included now when using the measured R_{nl}, which stems from measurements of the actual channel properties.

While this would in principle enable us to calculate the nonlocal voltage that is expected at around the current at which the electron heating temperature T^* saturates, it seems more promising to invert the formula in order to estimate one of the most interesting quantities of vortex motion, namely the transport entropy S_ϕ. As mentioned briefly in section 2.2.3, there are still controversial discussions about the proper theoretical modeling, and especially since the advent of the high-T_c superconductors, where the Nernst effect serves as one of the major experimental tools to explore the pseudogap region above the transition temperature, little experimental data was brought about for the class of the conventional type-II superconductors. Thus there is still quite some spread in both the experimental as well as the theoretical values of the transport entropy, spanning several orders of magnitude. We thus have

$$S_\phi = \frac{\Phi_0}{d}\frac{V_{nl}}{R_{nl}\Delta T} \quad . \tag{6.10}$$

The resulting values for the three lowest measurement temperatures together with the theoretical prediction from the Maki formula, see eq. 2.46, the prediction by Sergeev, Reizer and Mitin (SRM), see eq. 2.48 and [29], and experiments by Huebener et al. on Nb-films [39] and Vidal on Pb-In [89] are shown in figure 6.14. Although the actual values extracted from our measurements on the nonlocal voltage show some spread as well as deviations from both theories, the agreement with other experiments on conventional type-II superconductors and both theories in terms of order of magnitude is very good.
The remaining discrepancies from the two theories stem mainly from three points: (i) the uncertainty associated with the effective thermal healing length L_T of the temperature gradient along the channel (see figure 6.13), (ii) the fact that the extracted values of the entropy originate from measured values of diminutive signals and an oversimplified model, which inhibits a real quantitative comparison between our experiment and theory and (iii) the possibility of additional heating in the normal state.
The first two points are short arguments, whereas (iii) requires a longer discussion. So let me first add to (i) that in absence of a proper theoretical model L_T can be anything between several $\xi(t)$ and several $\ell_E = \sqrt{D\tau_0} \approx 300\,\mathrm{nm}$ for $T = 0.75\,\mathrm{K}$. This will depend on whether it is the high-energy tail of the distribution function that leads to the relaxation or whether one should rather consider this in terms of a sharp normal-superconducting boundary between the overheated normal region and the fully superconducting channel parts, leading to Andreev reflections of the quasiparticles at the interface. Regarding (ii) I think that although the thermal length drops out in our simple approach, it of course still influences the validity and actual values if one were to consider

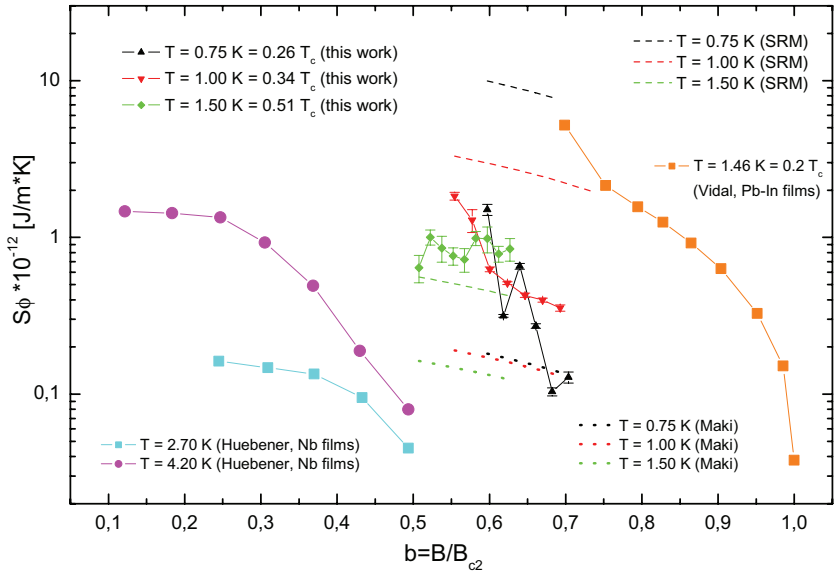

Figure 6.14: Transport entropy (per unit length) extracted from the nonlocal voltage measurements at the lowest three measurement temperatures, together with Maki's theoretical prediction (see eq. 2.46), the prediction by Sergeev, Reizer and Mitin (SRM) (see eq. 2.48 and [29]) and other experimental data on Nb (Huebener et al. [39]) and Pb-In (Vidal [89]).

a more sophisticated model instead. At this point we note that despite the uncertainty about the real length scale, the **temperature gradient is at least on the order of $1\,\mathrm{K}/\mu\mathrm{m}$**, which is several orders of magnitude larger than in studies on macroscopic films, where μm- or even mm-sized samples were used at similar temperature differences of roughly $1\,\mathrm{K}$. On top of that, we are dealing with a tiny effect, with the main input for the estimated S_ϕ coming from DC measurements of voltages on the order of $50\,\mathrm{nV}$, so the nonmonotonic behavior of the extracted transport entropy should not lead to an over-interpretation. Our crude model of this complicated effect obviously does not allow for a fully quantitative comparison to theory, yet the agreement in terms of order of magnitude is still satisfactory. Let me now discuss the more elaborate question of (iii):

Electron heating in the normal state

As mentioned above, the question arises what will happen in terms of heating in the normal state? It has long been shown that considerable heating of the electron system above the substrate temperature is easily achievable in mesoscopic wires by currents of several tens of μA (see e.g. [90, 91]). To check whether there might be a comparable

contribution above the phase boundary, i.e. for high currents, in addition to the electron heating in the superconducting state, noise measurements were carried out to determine the effective temperature independently of the above models. Without drifting off too far from our main course at this point, and without going into details of the measurements, I will briefly summarize the findings. A cross-correlation technique was used similar to ref. [88], where in order to cancel out the uncorrelated internal noise of amplifiers, the voltage signal from the sample is split and put into two amplifiers, whose output in turn is cross correlated by a spectrum analyzer. To avoid both the low-frequency region, where $1/f$-noise is dominant, and the high-frequency cut-off due to finite RC-filtering of the unavoidable sample resistance R and the coaxial cable and filter capacitances C, one choses a frequency window at moderate frequencies typically somewhere in between 10 and several hundred kHz where the noise level is flat and has no undesired radio peaks. Then, first a calibration of the noise level is needed: since the spectral density of the thermal (or Johnson-Nyquist) noise should be proportional to temperature according to

$$S_V = 4k_B T R \quad , \tag{6.11}$$

one can measure this quantity for different temperatures, which should yield a linear relation between the two, the slope basically given by the resistance of the sample (apart from $4k_B$). The spectral density is defined as $S_V = (\Delta V)^2/\Delta f$, where ΔV denotes the voltage fluctuations and Δf is the bandwidth. The result for our sample at different temperatures above T_c, i.e. in the normal conducting state, can be seen in figure 6.15. While the data are well described by a linear fit of the type of eq. 6.11 including a always present and finite offset, the actual value of the resistance is only $80\,\%$ of the measured 2-point resistance. This can rather unambiguously be attributed to the finite capacitances in our measurement setup: the coaxial lines used (with the bonding scheme from the previous measurements unchanged) account for roughly $1\,\mathrm{nF}$ (typically, coaxial lines have approx. $100\,\mathrm{pF/m}$ plus the contribution from the Cu-powder (rf) filters), and one additional π-filter could not be removed easily for these measurements, which adds another $7\,\mathrm{nF}$. This estimate perfectly matches the observed suppression of the total noise measured via

$$R_{eff} = R\frac{X_c}{\sqrt{R^2 + X_c^2}} \quad , \tag{6.12}$$

where $X_c = 1/(2\pi f C_{total})$, $C_{total} \approx 8\,\mathrm{nF}$, $R = 989\,\Omega$, $f = f_{center} = 15.5\,\mathrm{kHz}$ and $R_{eff} = 783\,\Omega$.

In the next step, one can now use the current dependence of the noise to estimate the heating effect due to applied current: a certain increase in the measured power spectral

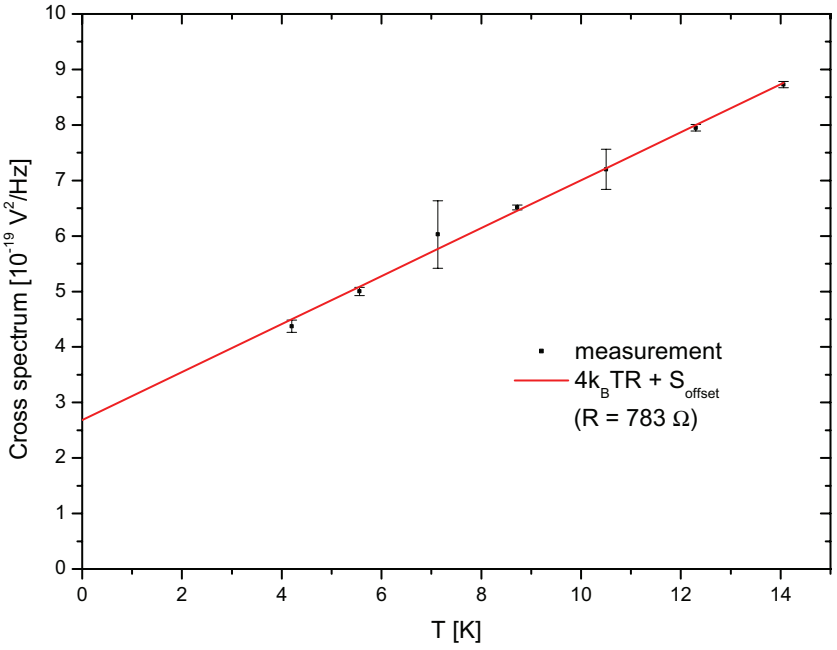

Figure 6.15: Calibration of the noise measurements via thermal noise for different temperatures at a bandwidth of $8\,\mathrm{kHz}$ *around the center-frequency of* $15.5\,\mathrm{kHz}$*. The resulting cross spectra are linearly proportional to the temperature with a finite offset in good agreement with* $S_V = 4k_BTR$*, but for a resistance of only* $80\,\%$ *of the measured 2-point resistance due to a suppression of the measured signal by the low-pass filter composed of the resistances and capacitances in the setup.*

density for a given applied current with respect to zero current can be translated into an effective electron temperature using eq. 6.11: at zero applied current, the signal should be given by the thermal noise at the measurement temperature plus a finite offset, which does not necessarily have to be the same as in the temperature dependence data. In order to compare to the heating effect relevant for the nonlocal data, originally it was planned to perform this set of measurements at $T = 0.75\,\mathrm{K}$. Unfortunately, it turned out that anywhere in the superconducting state, the obtained spectrum was anything but flat and thus unusable. Besides, other effects are expected to strongly influence the noise in the superconducting regime [92, 88]. Instead, measurements were performed at $T = 2.00\,\mathrm{K}$ and $B = 3.00\,\mathrm{T} > B_{c2}(2.00\,\mathrm{K})$ in the normal state. The result of the current dependence measurement of the noise is shown in figure 6.16.

Since we are only interested in a rough estimate of the (additional) heating effect in the normal state, our main purpose here is to get a coarse analytic description of the current dependence in order to apply it to the nonlocal $E(j)$ measurements. In the graph, two

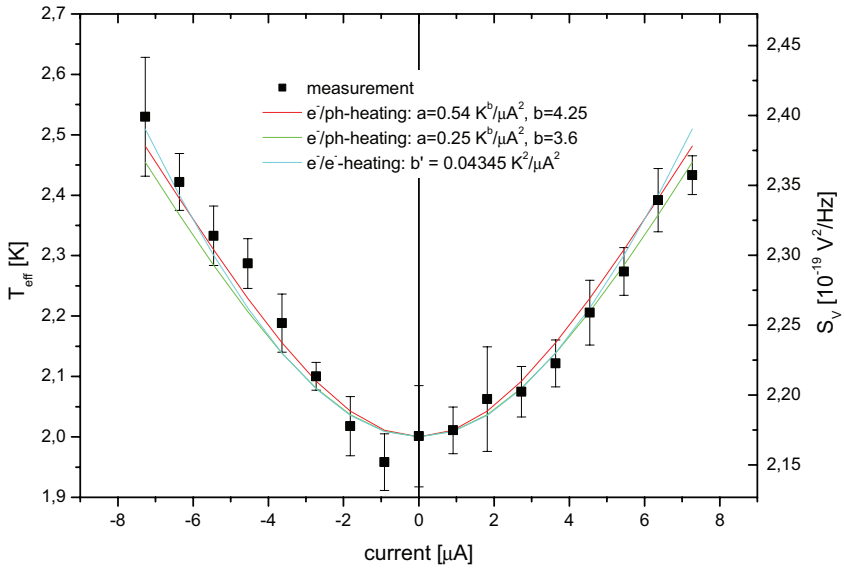

Figure 6.16: Current dependence of the measured cross spectrum at a bandwidth of $8\,\mathrm{kHz}$ *around the center-frequency of* $15.5\,\mathrm{kHz}$ *at* $T = 2.00\,\mathrm{K}$ *and* $B = 3.00\,\mathrm{T} > B_{c2}(2.00)\,\mathrm{K}$ *(normal state). The meaning of the fit parameters for the electron-electron and the electron-phonon heating are explained in the text.*

different models have been used to fit the experimental data: one uses the semi-empirical formula

$$T_{eff} = \left(aI^2 + T_0^b\right)^{1/b} \quad , \tag{6.13}$$

which basically stems from electron-phonon coupling and where T_{eff} is the elevated temperature, a is a measure of the electron-phonon coupling strength and the physical origin of b is beyond the scope of this report [90]. Lacking an easy way to estimate a and b, we just note that the experimental data is well accounted for by a range of parameters a and b. The value for b is approximately the same as in [90], whereas a is larger by roughly a factor of 10. This indicates a weaker electron-phonon interaction than in [90], but most likely, another model is more appropriate in this case: namely, another fit is possible via

$$T_{eff} = \sqrt{T_0^2 + b^2V^2} = \sqrt{T_0^2 + b'^2I^2} \quad , \tag{6.14}$$

which is based on electronic heat diffusion and the Wiedemann-Franz law $\lambda = \mathcal{L}_0 T\sigma$, where λ is the thermal and σ the electrical conductivity, while $\mathcal{L}_0 = (\pi k_B)^2/(3e^2) =$

$2.44 \cdot 10^{-8}\,\mathrm{V}^2/\mathrm{K}^2$ [91]. The parameter b is given by

$$b = \frac{b'}{R^2} = \sqrt{\frac{1}{\pi \mathcal{L}_0} \frac{R_\square}{R} \ln \frac{r_1}{r_0}} \quad , \tag{6.15}$$

where R is the measured normal state resistance, $r_1 \approx l_{e-e}$ is the smallest geometrical length scale involved in this heat chain model, roughly given by the electron-electron scattering length, and $r_0 = min(l_{e-ph}, L_{res})$ is the largest geometrical length scale involved, given by the minimum of the electron-phonon scattering length and the size of the reservoirs L_{res}. When plugging in values for our sample, we arrive at $b' \approx 4.5 \cdot 10^{-3}\,\mathrm{K}^2/\mu\mathrm{A}^2$, which is roughly a factor of 10 smaller than the fit parameter found. This may come from deviations from the Wiedemann-Franz law, which is used in the derivation of the model. Whatever may be the real origin in our case does not seem to change much the rather good fit of the experimental data by the theoretical curves. A deep and thorough analysis would require further experiments, probably a different setup and a lot of effort, which seems not justified for our purpose in this report. But it does allow us to estimate the additional heating effect in the normal state, once the electron heating, which describes the FFI features in local $E(j)$-curves, saturates at $T^*(E_c)$.
Using the second fitting approach, this is summarized in figure 6.17, where (a) the local $U(I)$, (b) the (symmetrized) nonlocal responses and (c) the presumed full heating effect for arbitrary currents are shown. The curve for the heating at high currents was produced by a fit of the type of eq. 6.14, with b' determined from our noise measurements fit, and the bath temperature T_0 chosen such that the curve smoothly joins onto $T^*(I)$ at $I(E_c)$. This yields an intuitive picture for the full current dependence of the heating: at low currents, in the region before the FFI in the local curve, the nonlocal signal consists of a pure Lorentz force TFTE, with a near linear slope and no heating at all. Then, as the FFI sets in around E_c in the local curve, the electron heating steeply kicks in, producing the quick decay of the asymmetric Lorentz force signal and the rise of the Nernst signal. While this model predicts a saturation of T^* at E_c, naturally one would expect an additional heating in the normal state, which is qualitatively well accounted for by our noise measurements and also is indicated by the nonzero slope of the Nernst signal for currents above E_c.

As the main result of this excursus to noise measurements we note that we expect an additional heating effect in the normal state above E_c on the order of roughly $200\,\mathrm{mK}$ for $I = 4.5\,\mu\mathrm{A}$. This can now be used to correct the estimate of the transport entropy, where the underestimated temperature gradient (neglecting the above effect) lead to an overestimation of S_ϕ. We also see from figure 6.17 that the Nernst signal at high currents, which has been used for the calculation of S_ϕ in figure 6.14, can not be attributed to T^*, the temperature extracted from the heating in the superconducting state, only,

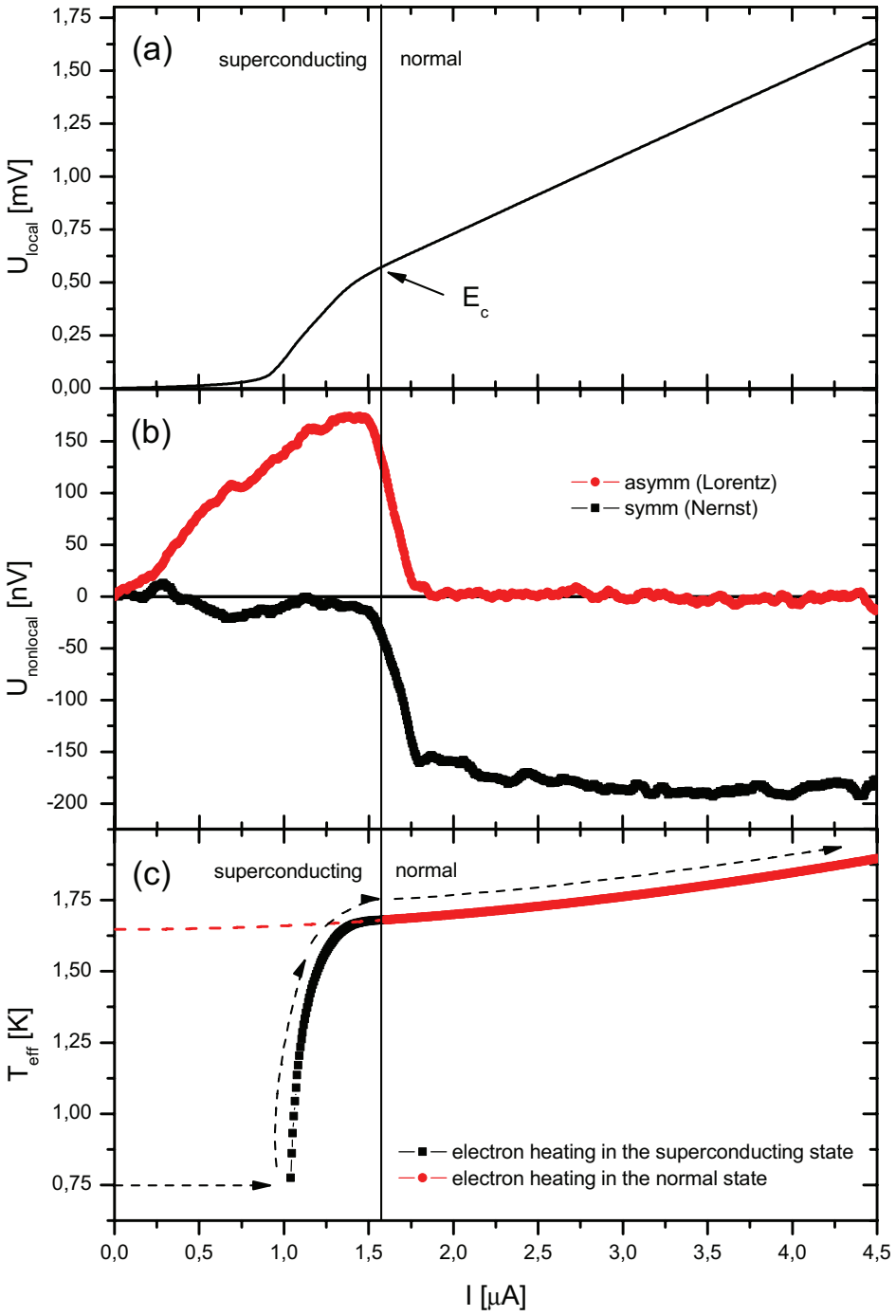

Figure 6.17: (a) Local $U(I)$ at $T = 0.75\,\mathrm{K}$ and $B = 3.00\,\mathrm{T}$, (b) Nonlocal $U(I)$, divided into the Lorentz part (asymmetric) and the Nernst part (symmetric) and (c) heating temperature $T_{eff}(I)$ as described by $T^*(I)$ $(I < I(E_c))$ and T_{eff} in the normal state $(I > I(E_c))$ as estimated from noise measurements.

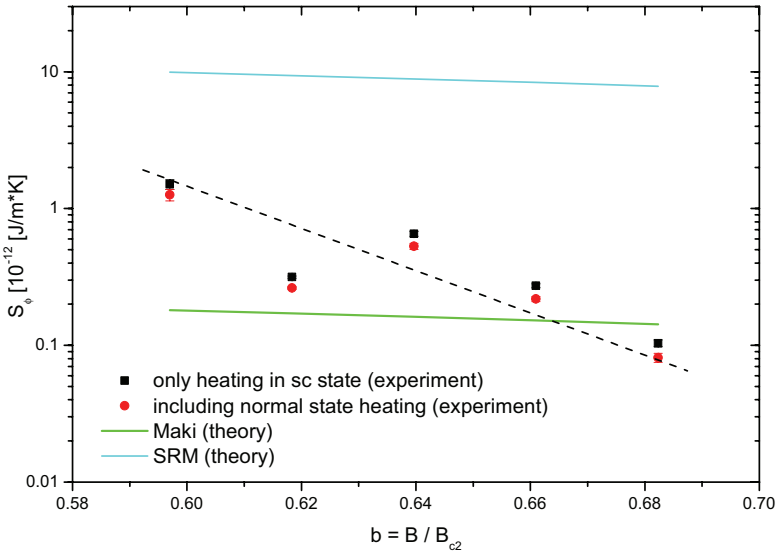

Figure 6.18: Corrected estimate of the transport entropy S_ϕ by using the enlarged temperature gradient due to additional heating in the normal state (red circles) together with the original estimate (black squares), which takes into account only the T^*-contribution in the superconducting state. Also shown are the two theoretical predictions using the theories of Maki (green) and SRM (cyan) respectively at $T = 0.75\,\mathrm{K}$. The dashed line is only a guide to the eye.

since there is a significant increase of its absolute value above E_c, i.e. after the crossover. The use of the high-current nonlocal voltage as the input for calculating the entropy is justified since for lower currents, the Lorentz part is not yet fully decayed to zero. Now taking into account the additional heating in the normal state, the corrected estimate for the transport entropy at $T = 0.75\,\mathrm{K}$ is shown in figure 6.18, which due to the small correction in ΔT also has only a small effect. The dashed line is just a guide to the eye. The error bars stem from uncertainties in the measured input values for R_{nl}, V_{nl} and ΔT, and are rather small. The systematic errors, such as the oversimplified model, obviously have the strongest influence on the observed stronger variation with magnetic field than the theories predict. The same is true for the other two experiments shown in figure 6.14. The values extracted from the experiment still lie in between the two theories. So here we conclude that the major contribution to the temperature gradient responsible for the Nernst signal comes from the electron heating model of the FFIs in the superconducting state, and that while there seems to be an additional component due to heating in the normal state, its contribution is of minor significance.

One more thing that one can do is the extraction of the magnetic field dependence of the nonlocal signal for different currents, which corresponds then to the previously done magnetic field sweeps in refs. [11, 12]. This is shown in figure 6.19 for both current directions and all of the recorded fields at $T = 0.75\,\mathrm{K}$. Despite some runaway points and noise, the plots clearly support the main finding: at low currents, the signal displays a peak due to the Lorentz force which is asymmetric in applied current, and at higher currents this evolves into the (negative) symmetric Nernst signal. With respect to the small and noisy signal and the limited resolution, the symmetry produced is remarkable. All points at high fields should be seen with some caution, since the $U(I)$-curves for $B \geq 4.0\,\mathrm{T}$, which is already close to or already above $B_{c2}(0.75\,\mathrm{K}) = 4.69\,\mathrm{T}$, generally suffer from significant scatter.

All in all, the low-temperature nonlocal data can be understood as an interplay of Lorentz force and thermal force, where the latter stems from an unusually high temperature gradient on the order of $1\,\mathrm{K}/\mu\mathrm{m}$.

6.2.2 High temperatures: Lorentz force vs. gap suppression

Now we turn to the nonlocal data obtained close to the transition temperature, where local measurements confirmed that we are dealing with the regime of vortex-core shrinking.

Again, while in principle more data at several temperatures would be available, we concentrate on $T = 2.50\,\mathrm{K}$, where the most typical features could be observed. Nonlocal voltage-current characteristics for this temperature are shown in figure 6.20 at magnetic fields $0.40\,\mathrm{T} < B < 0.60\,\mathrm{T}$, which corresponds to the region around the peak of the nonlocal signal observed in the AC magnetic field sweep test measurements (see figure 6.1).
Anticipating more insight from symmetrization as in the case of low temperatures, the graph also features plots of the symmetric and asymmetric parts. Even without symmetrization, there is clear evidence for a linear part around zero current, which can be attributed to the action of the Lorentz force and the 'conventional' TFTE. This is further confirmed in the plot of the asymmetric part, where dashed lines are drawn to highlight the linear section.
But for higher currents, the opposite of the low-temperature behavior is observed: the high-current region displays a positive symmetric signal, which, including a sign change of the nonlocal response for negative currents, corresponds to vortex motion towards the local, current-carrying wire irrespectively of the current direction.
Employing once again our knowledge of the nonlinear local $E(j)$, we conjecture the origin of this effect in the LO-regime, which again should be restricted to the local

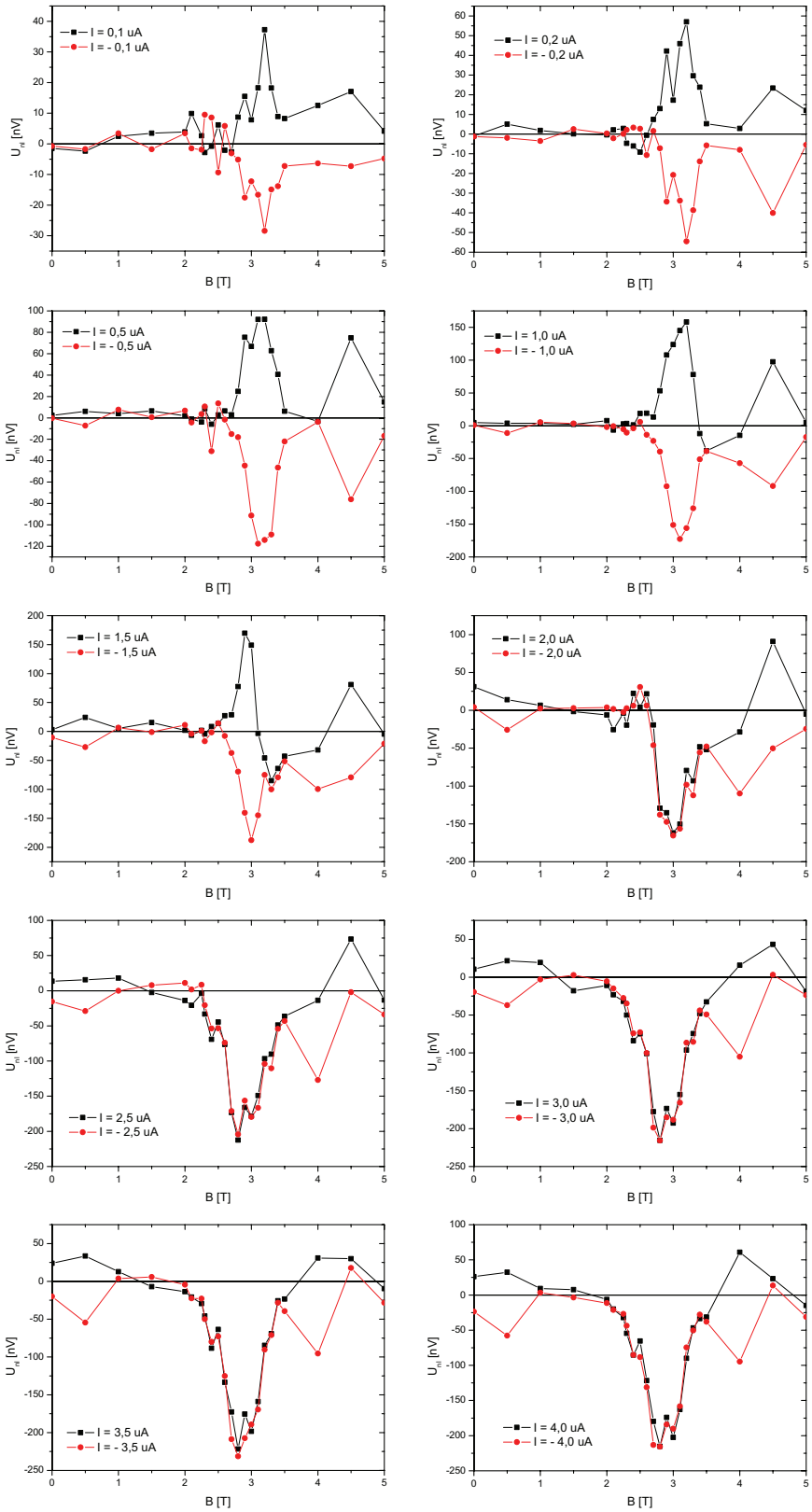

Figure 6.19: Reconstruction of the field dependence of the nonlocal signal at $T = 0.75\,\mathrm{K}$ *from the current sweeps.*

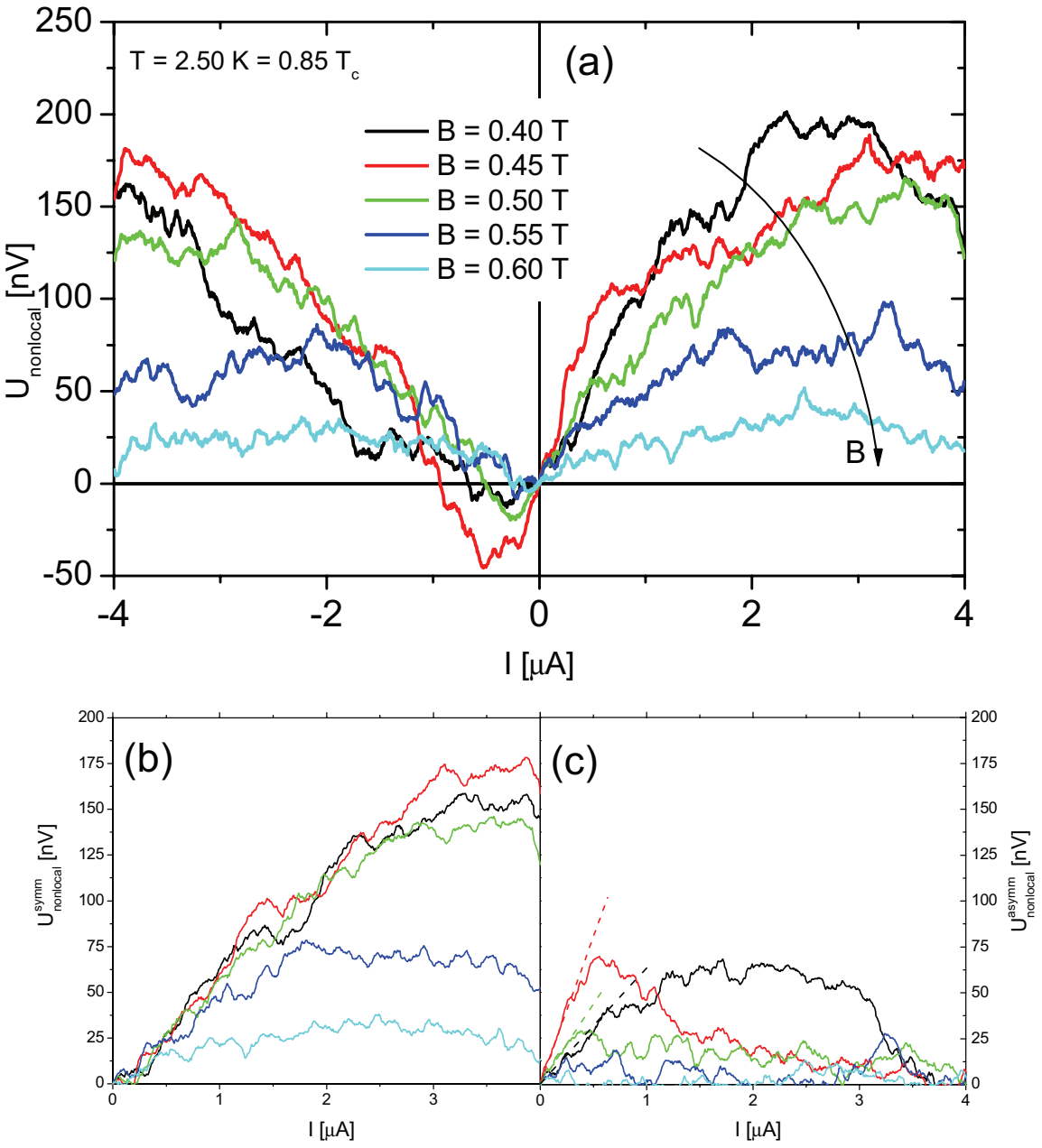

Figure 6.20: (a) Nonlocal $V(I)$-curves at $T = 2.50\,\mathrm{K}$ for magnetic fields around the highest efficiency, (b) symmetric and (c) asymmetric part. The dashed lines in (c) indicate R_{nl}, the nonlocal resistance around zero current.

wire. This builds the basis for the following qualitative reasoning: The locally confined vortex-core shrinking regime should lead to a suppression of the gap in the current-carrying wire. Inside the channel, the effect should be absent due to a negligible current density. Having such a local gap suppression, the vortices in the channel, where the gap is undisturbed, will feel a gap gradient, and thus a force towards the region where they cost less condensation energy. Since the gap suppression does happen irrespective of the direction of the applied current, this would unambiguously lead to vortex motion towards the local cross and a positive nonlocal voltage at high applied currents. Dr. Denis Vodolazov [93] has estimated this effect in the framework of time-dependent GL-theory: the free energy of the superconducting state

$$\mathcal{F} = -\frac{B_c^2}{2\mu_0}\int |\psi|^4\, dV \quad , \tag{6.16}$$

assuming that the field inside the superconductor is equal to the external magnetic field, B_c is the thermodynamic critical field and $|\psi|$ is the absolute value of the order parameter. If we assume further that the order parameter varies on a length scale of $L_E \sim \sqrt{D\tau_E} \gg \xi$, and that

$$\psi(x) = \psi_\infty - \Delta\psi\, \mathrm{e}^{-(x/L_E)^2} \tag{6.17}$$

with ψ_∞ as the undisturbed value of the order parameter far from the vortex, then

$$\frac{\partial}{\partial x}|\psi(x)|^4 = 8\frac{x}{L_E^2}\Delta\psi\, \mathrm{e}^{-(x/L_E)^2}\left(\psi_\infty - \Delta\psi\, \mathrm{e}^{-(x/L_E)^2}\right) \quad , \tag{6.18}$$

and thus the force on a single vortex due to the gradient in the order parameter is given by

$$F_{\nabla\psi} = -\frac{\partial\mathcal{F}}{\partial x} = \frac{4}{\mu_0}B_c^2\,\xi^2 d\frac{x}{L_E^2}\Delta\psi \mathrm{e}^{-(x/L_E)^2}\left(\psi_\infty - \Delta\psi \mathrm{e}^{-(x/L_E)^2})^3\right) \quad . \tag{6.19}$$

The term $\xi^2 d$ represents the volume of the vortex. The order parameter here is written in dimensionless units and both ψ_∞ and $\Delta\psi$ are less or about 1. The above equation is valid up to some numerical coefficient of about unity. The geometrical situation is sketched in figure 6.21: The current in the local wire causes a local suppression of the order parameter, which 'heals' on the length scale of L_E. In case of weak magnetic fields $B \ll B_{c2}$, one can estimate

$$\Delta\psi = 0.04\frac{B}{B_{c2}}\left(\frac{v_\phi}{v_i}\right)^2 = 0.04\frac{B}{B_{c2}}\left(\frac{E}{E_i}\right)^2 \quad , \tag{6.20}$$

using results obtained for the nonequilibrium quasiparticle distribution function by Larkin and Ovchinnikov [94], valid only if $\Delta\psi \ll \psi_\infty$. For fields on the order of B_{c2} only numerical results can be obtained, because in this case the order parameter profile near the

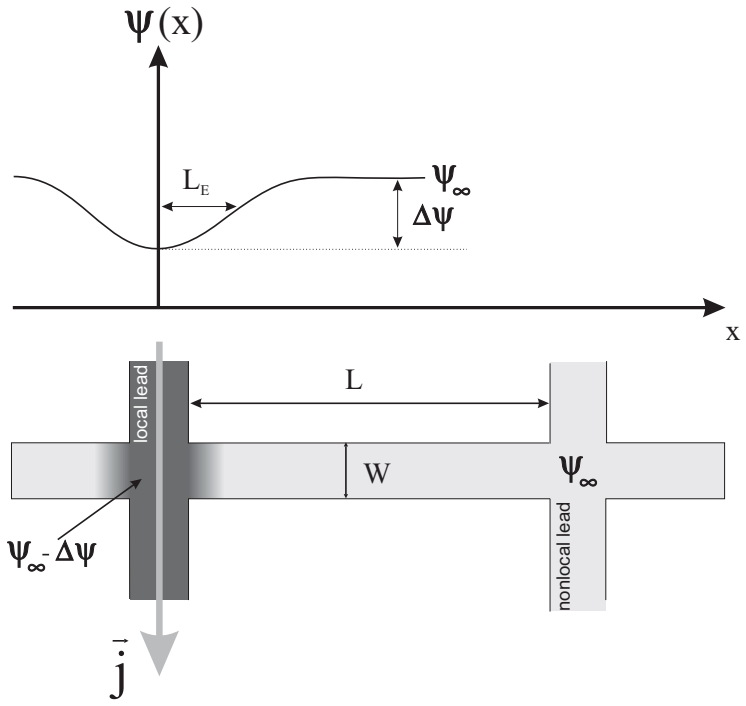

Figure 6.21: Schematic of the geometrical situation that leads to the spatial gradient of the order parameter.

vortex core depends on B (and ψ_∞ too). Numerical simulations indicate a saturation of $\Delta\psi$ as a function of v/v_c^2 [93]. This is shown in figure 6.22; so far, only numerical results for $(v/v_i)^2 < 3$ are available. Two things are worth noting about this plot: for higher vortex velocities, $\Delta\psi$ grows slower than suggested by equation 6.20, because the order parameter itself decreases with increasing v. Secondly, if we fix $(v/v_i)^2$, then we see that $\Delta\psi$ is nonmonotonic in B: at low fields, it increases with field, but then decays again. This is a consequence of the suppression of the gap by magnetic field [93].

Since we are still basically dealing with the same effect, namely the TFTE, as in case of the Lorentz force and the Nernst effect, yet with a third kind of driving mechanism, given by the gap gradient, we can once again repeat the analysis in terms of our pressure model, this time with the gradient in the order parameter as the driving force: Considering the geometry (channel length L, wire width W, sample thickness d, cross-sectional area $A = Wd$), at vortex density $n_\Phi = B/\Phi_0$, $n_\Phi W L_E$ vortices in the local wire encounter

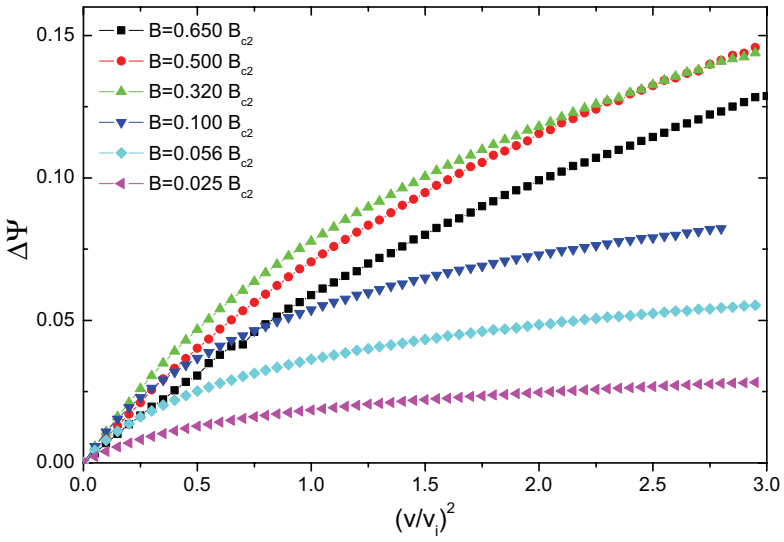

Figure 6.22: Dependence of the effective gap suppression $\Delta\psi$ on the normalized vortex velocity $(v/v_i)^2$, which essentially stands for the effective electric field (i.e. equivalently, $(E/E_i)^2$ could be used). In other words, this can also be regarded as the current dependence of the gap suppression. These results have been obtained by numerical simulations [93].

a force $F_{\nabla\psi}$ due to the gradient in ψ, thus applying a pressure of

$$p = \frac{n_\Phi W L_E F_{\nabla\psi}}{Wd} = \frac{L_E}{d} n_\Phi F_{\nabla\psi} \tag{6.21}$$

to the vortices in the channel. One can argue whether to say that the number of vortices encountering the force is given by $n_\Phi W L_E$, $n_\Phi W^2$ or $n_\Phi W \max(\mathrm{L_E}, \mathrm{W})$. Whichever it is can easily be changed in the final result; besides, $L_E \sim W$, see estimates below.

The corresponding pushing force per unit length $f_{push} = pA/d = pWd/d = pW = \frac{W}{d} n_\Phi L_E F_{\nabla\psi}$ is balanced by the force required to move $n_\Phi LW$ vortices in the channel against the frictional damping ηv_φ per vortex (where v_φ is the vortex velocity in the channel and η reflects the channel properties). The above yields

$$\frac{W}{d} n_\Phi L_E F_{\nabla\psi} = n_\Phi LW\eta v_\varphi \Leftrightarrow v_\varphi = \frac{L_E}{L\eta d} F_{\nabla\psi} \quad . \tag{6.22}$$

Using $V_{nl} = WBv_\varphi$, we arrive at

$$V_{nl} = WB\frac{L_E}{L\eta d} F_{\nabla\psi} = \frac{WB\Phi_0}{L\eta d}\frac{L_E}{\Phi_0} F_{\nabla\psi} = R_{nl}^{\mathrm{Lorentz}} \frac{L_E}{\Phi_0} F_{\nabla\psi} \quad . \tag{6.23}$$

Now we can estimate the nonlocal voltage by plugging in the numbers for $F_{\nabla\psi} = F_{\nabla\psi}(B_c(T), \xi(T), x, L_E, \psi_\infty, \Delta\psi)$ in eq. 6.19. And as mentioned above, one can still use W or $\max(L_E, W)$ instead of L_E, if required. For this, we need the following numbers as an input:

- From [16] (eq. (1)):

$$\xi^2(t) = \frac{e\Phi_0 D}{8k_B T_c(1-t)} \Longleftrightarrow D = \frac{8k_B T_c \xi^2(0)}{e\Phi_0} = 4.802 \cdot 10^{-5}\,\mathrm{m}^2/\mathrm{s} \tag{6.24}$$

- From the local $E(j)$-curves, using the LO-theory and the analysis for E_i [15]:

$$T = 2.50\,\mathrm{K}: \quad u_i = 205\,\mathrm{m/s} \tag{6.25}$$

- Following [16], this yields

$$\tau_{e,ph} = \frac{D}{\pi u_i^2}\sqrt{14\zeta(3)(1-t)} = 0.58\,\mathrm{ns} \tag{6.26}$$

  where $\zeta(3) = 1.20206$.

- This gives

$$L_E = \sqrt{D\tau_{e,ph}/\sqrt{1-t}} = 268\,\mathrm{nm} \tag{6.27}$$

  Note that the energy relaxation rate τ_E is not $\tau_{e,ph}$, it is larger by a factor $\sim 1/\sqrt{1-t}$, and this affects L_E (which is not $L_{e,ph}$ - see the paragraph above Eq.(12) in [16]).

- Additionally, we have

$$B_c(T = 2.5\,\mathrm{K}) = \frac{B_{c2}(T)}{\sqrt{2}\kappa} = \frac{1.0\,\mathrm{T}}{\sqrt{2}\cdot 74} = 10\,\mathrm{mT} \tag{6.28}$$

In order to obtain an estimate for the resulting force, we consider $F_{\nabla\psi}$ as a function of $\Delta\psi$ and x. Physically, the numerics indicate that at typical values of the current where we see the maximum nonlocal response, here taken to be the exemplary values of $T = 2.50\,\mathrm{K}$, $B = 0.45\,\mathrm{T}$ and $I = 3$ to $4\,\mu\mathrm{A}$ (see figure 6.20), we are dealing with $E \approx 5E_i$, or$(v/v_i)^2 = (E/E_i)^2 \approx 25$ correspondingly. A rough interpolation to the $b = 0.5$-curve of figure 6.22 for higher values of $(v/v_i)^2$ yields $\Delta\psi \approx 0.4$ - 0.5. A 3-dimensional plot of $F_{\nabla\psi}(\Delta\psi, x)$ is shown in figure 6.23. The maximum values of the force for the estimated maximal suppression at $\Delta\psi \approx 0.4$ - 0.5 happens in a very good approximation around $x = L_E$.

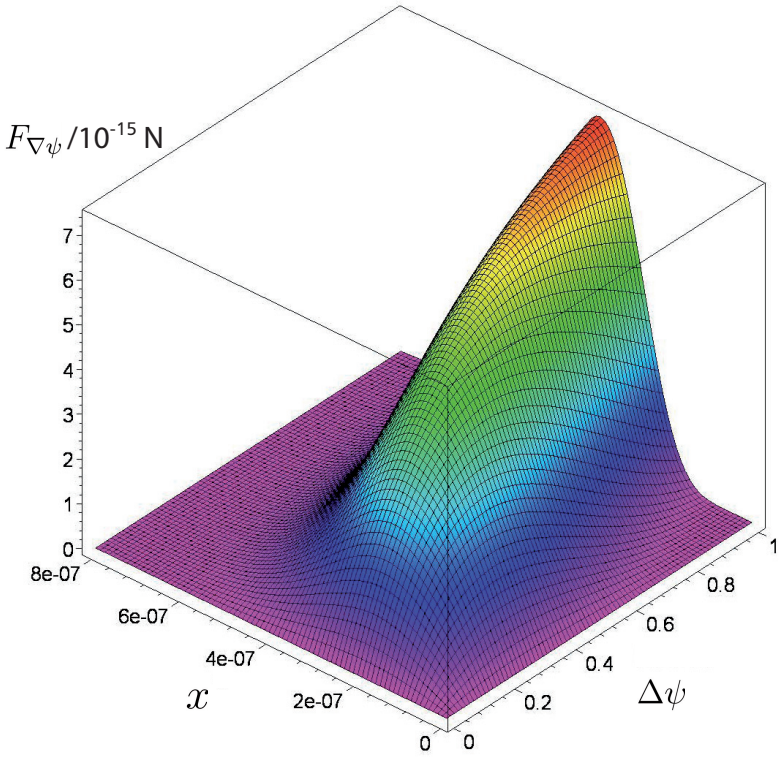

Figure 6.23: 3-dimensional plot of the force $F_{\nabla\psi}$ due to the gap suppression as a function of $\Delta\psi$ and x.

This yields as a rough estimate

$$F_{\nabla\psi} \approx 5 \cdot 10^{-15}\,\mathrm{N} \quad , \tag{6.29}$$

where $\xi(t = 2.5/2.94) = \xi(0)/\sqrt{1-t} = 18\,\mathrm{nm}$ for $T = 2.50\,\mathrm{K}$ with $\xi(0) = 7\,\mathrm{nm}$ (from GL-fits to $B_{c2}(T)$) have been used. Putting this into our pressure model, we get

$$V_{nl} = R_{nl}^{\mathrm{Lorentz}} \frac{L_E}{\Phi_0} F_{\nabla\psi} \approx 120\,\mathrm{nV} \tag{6.30}$$

(irrespective of the actual value of L_E, since when using $x \approx L_E$, the actual length scale of the gradient drops out as in case of the thermal force) where the value $R_{nl} = 0.18\,\Omega$ for $T = 2.50\,\mathrm{K}$, $B = 0.45\,\mathrm{T}$ from linear fits to $E_{nl}(j)$ around zero was used[1].
With respect to our very crude approach, the agreement with the measured maximum values of around $U_{nl} = 175$ to $200\,\mathrm{nV}$ is more than satisfying. A more accurate model

[1]One could also take the same fits for the asymmetric parts only, which yields $R_{nl} = 0.16\,\Omega$ from linear fits to $E_{nl}(j)$, giving only marginal corrections in terms of order of magnitude.

should of course take into account the full geometric dependence of the force as well as edge effects amongst other things. This will be the subject of further theoretical and numerical work on the topic [93].

Summarizing this part, we conclude that the nonlocal voltage for T close to T_c is well understood in terms of an interplay between the Lorentz force at low currents, and a force due to a local suppression of the superconducting gap on the order of $40\,\%$ at currents, temperatures and fields typically used in this study.
Finally, as in the previous section, we can again reproduce the magnetic field dependence of the nonlocal voltage by extracting values at constant current from different nonlocal $V(I)$-curves, which is shown in figure 6.24. One can easily identify the asymmetric response due to Lorentz force at low currents, and the symmetric signal at high currents due to the gap suppression force. The remaining slight asymmetries between the two polarities are no surprise due to the limited resolution of our voltage values and low averaging in terms of current values.

Comment on the confinement potential

As mentioned in the theory chapter, the origin of the lateral confinement required to keep the nonlocally driven vortices inside the channel is not completely clear up to date. Yet we strongly believe that surface pinning provides the origin of the vortex confinement over the whole length of the channel.
Assuming the presence of stripes of pinned vortices along the edges, one expects a difference in vortex mobility in the local and nonlocal measurements, since in the first case they move perpendicular to the channel, and in the second case parallel to it. While the strong pinning at low fields and currents observed in the local curves seemed to support this assumption at first sight, it turned out that this is only true for the lowest fields, in fact much less than $2\,\mathrm{T}$, where the nonlocal voltage is also zero, because the immobile vortices in the drive wire cannot push those in the channel. This confirms that at low magnetic fields, strong pinning sites are saturated before the interstitial flux lines are more or less free to move.
In a more quantitative comparison, we note that for an exemplary temperature of $T = 0.75\,\mathrm{K}$ and $B = 3.0\,\mathrm{T}$, we get $R_{local} \approx 25\,\Omega$, whereas $R_{nl} \approx 0.14\,\Omega$ only. While this already makes up for the current dependence when using resistance instead of voltage, another factor is of course the geometry: the voltage (used for calculating the resistance) in the local case stems from a contact distance 8 times as large as in the nonlocal case. At the same time, using our pressure model, we assume that (at least, neglecting the actual cross areas plus the tails at the top and bottom of the channel) all vortices inside the channel have to be moved by the vortices in the local upper cross against the frictional

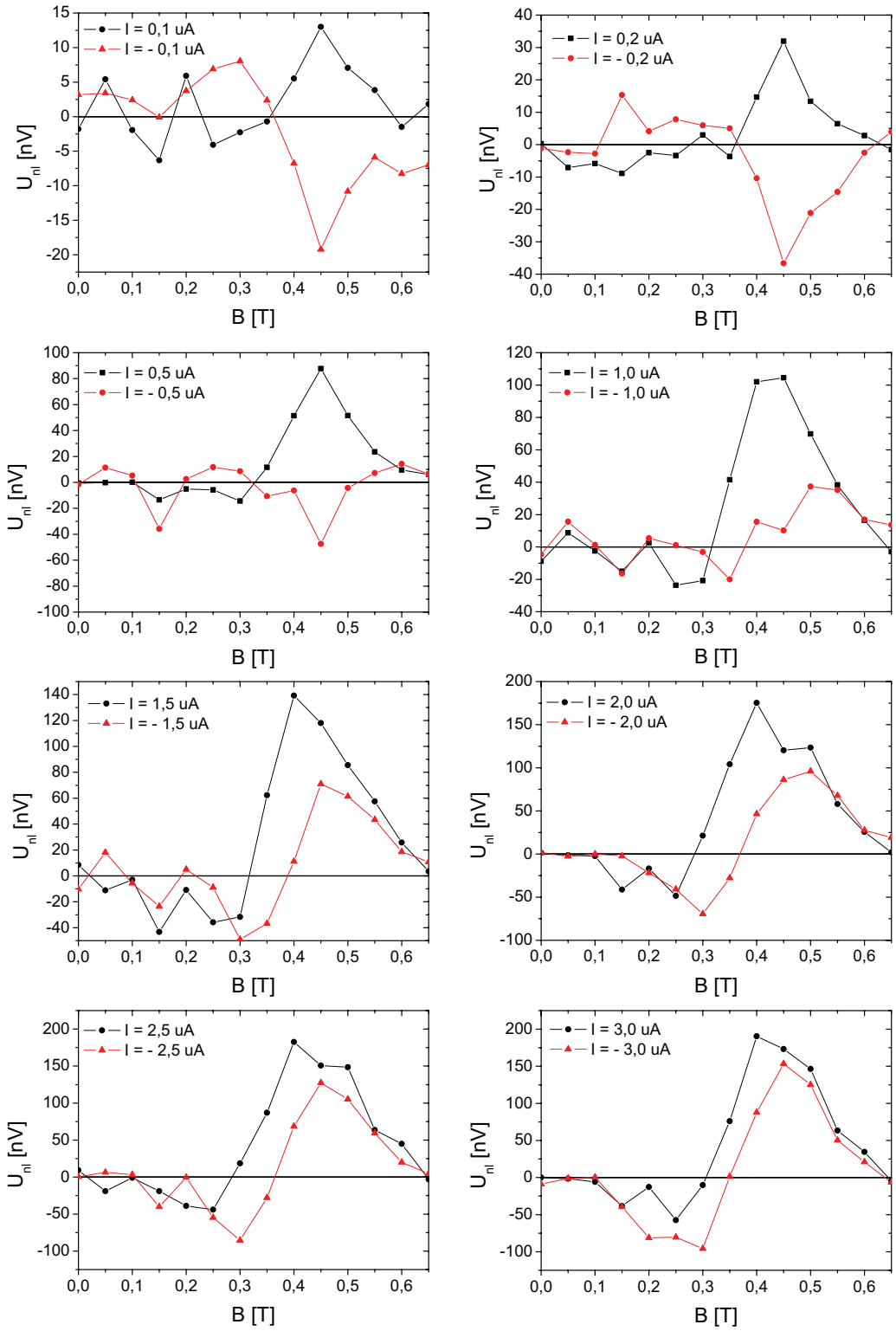

Figure 6.24: Reconstruction of the field dependence of the nonlocal signal at $T = 2.50\,\mathrm{K}$ *from the current sweeps.*

damping, since only the latter ones experience the Lorentz force. In the local case, each vortex has only to overcome its own damping force $-\eta v_\varphi$. Effectively, this yields another factor of 8 that the local resistance has to be larger even without different geometric pinning strengths.
This results in $R_{nl,corrected} \approx 9\,\Omega$, which is still smaller than $R_{local} = 25\,\Omega$. The remaining discrepancy can be attributed to the fact that our pressure model does neither account for the additional damping / friction due to the shear of the vortex river against the surface pinned flux lines nor for the more realistic exponential damping of this huge vortex number. That is, our pressure model still assumes force balance between the driving force and the total damping by all vortices inside the channel, which most likely hugely underestimates the actual frictional force. For our purposes, the above considerations is the best we can do in absence of a better knowledge about and a good description of the influence of pinning.

Chapter 7

Nonlocal response very close to T_C

Immediately below the transition temperature, our measurements hint at different mechanism being responsible for the nonlocal signals observed. In previous measurements, samples with half the thickness, i.e. $d = 20\,\mathrm{nm}$ have been used [79]. This lead both to lower pinning, and in return to considerably higher nonlocal signals on the order of $R_{nl} \sim 10\,\Omega$ and to substantial lowering and broadening of the superconducting transition in $R(T)$. This can be seen in part (b), right-hand scale of figure 7.1. In part (a), the nonlocal signals from magnetic field sweeps for different temperatures are shown, which have been offset for clarity by arbitrary amounts. The fields of the nonlocal peaks on both sides of $B = 0$ successively decrease, until at temperatures very close to $T_c = 2.52\,\mathrm{K}$, they start to overlap. This implies that there is a finite nonlocal signal even in absence of magnetic fields, i.e. without vortices due to an externally applied magnetic field. While this is already a first hint at the possibility of a Berezinskii-Kosterlitz-Thouless transition as described in section 2.5, a more systematic study was performed after careful demagnetization of the superconducting magnet system to minimize coercive fields due to trapped flux. The result is shown in figure 7.1 (b), left-hand scale. For temperatures lower than roughly $90\,\%$ of T_c, the nonlocal signal is basically zero with some finite offset value. But as the temperature approaches the transition, a nonlocal signal on the order of $30\,\Omega$ appears, which is even higher than the nonlocal signal at finite magnetic fields. The signal has a peak around $0.97 \cdot T_c$ and vanishes in the normal state. This is a strong indication that possibly the thermal excitation of vortex-antivortex pairs might be responsible. An applied driving current would inevitably dissociate the pairs, leading to a conventional Lorentz-force TFTE. In [95], Yazdani et al. observed a BKT-like melting of the disordered vortex lattice in thin films of a-MoGe, which is very similar to a-NbGe. They extracted a transition temperature $T_{BKT} \approx 0.975 \cdot T_c$, which coincides with the value observed in our study, although this simple transfer is of course just a very crude estimate.

The samples of the current study have a thickness of $d = 40\,\mathrm{nm}$ to avoid inhomogeneities

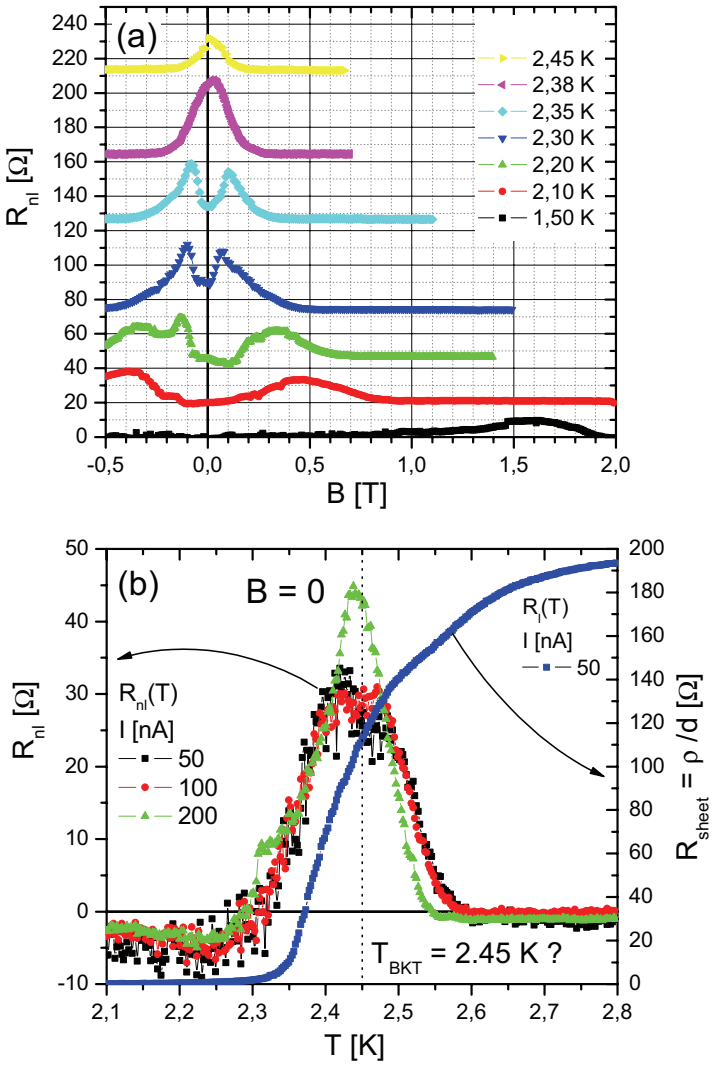

Figure 7.1: Data from [79]: (a) Nonlocal signal from magnetic field sweeps for different temperatures, offset for clarity. The fields of the nonlocal peaks on both sides of $B = 0$ successively decrease, until at temperatures very close to $T_c = 2.52\,\mathrm{K}$, they start to overlap. (b) Local and nonlocal resistance in absence of magnetic field (magnet demagnetized). Strikingly, there is also a finite nonlocal signal present in without field, which could indicate the presence of thermally excited vortex-antivortex pairs that are dissociated by the transport current and driven through the channel in the usual manner. Note that in this study, films of half the thickness, namely $d = 20\,\mathrm{nm}$ where used, which leads to a much higher nonlocal signal on the order of $10\,\Omega$, but at the same time to a low and considerably broadened transition temperature.

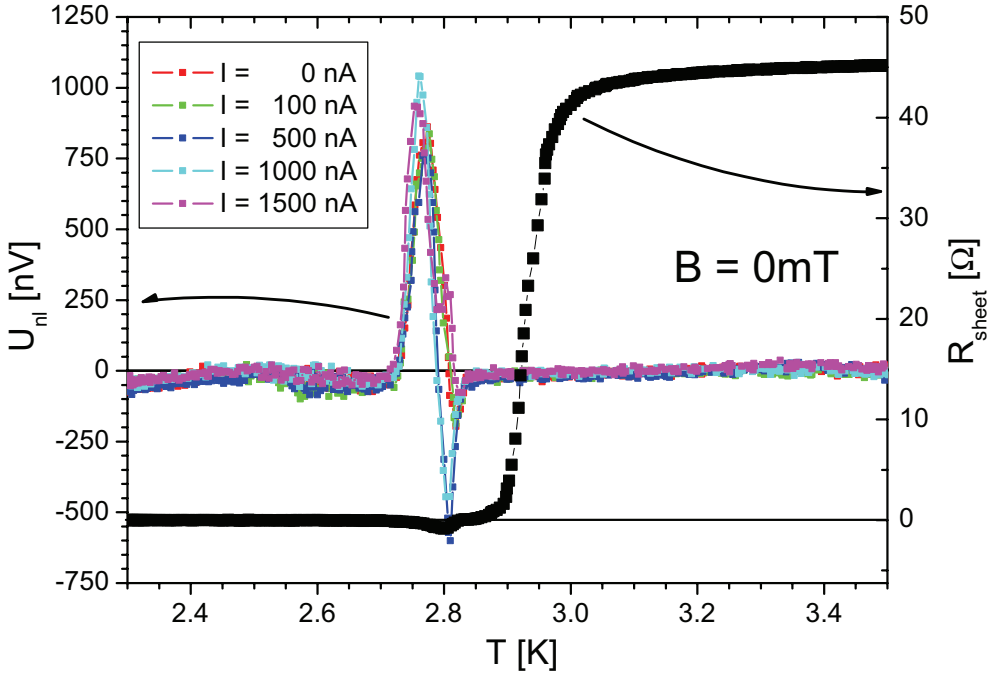

Figure 7.2: Local $R(T)$ at $I = 100\,\mathrm{nA}$ (right-hand scale) and the temperature dependence of the nonlocal signal for different applied currents in absence of an externally applied magnetic field (left-hand scale; magnet demagnetized). There is a huge nonlocal response, roughly five times larger than the maximum signal at finite magnetic fields, at first sight possibly due to vortex-antivortex pair dissociation. But the fact that almost no current dependence is observed and even more importantly that the signal persists even without applied current cannot be explained by a BKT-transition only. Additionally, both the local and the nonlocal signal display negative dips, whose origin cannot be explained.

and an even lower sheet resistance than the previously used samples with $d = 20\,\mathrm{nm}$. Nevertheless, similarly interesting features have been observed in measurements in close vicinity of $T_c = 2.94\,\mathrm{K}$.

Figure 7.2 shows both the local (right-hand scale) and nonlocal (left-hand scale) signal as a function of temperature. Interestingly, there is a not only finite, but roughly five times larger nonlocal signal even in the absence of magnetic field compared to the case with magnetic field. This could in principle come from the current induced dissociation of thermally excited vortex-antivortex pairs, but since the observed positive part of the voltage is rather independent of the applied current, and even unchanged without any applied transport current, this seems more than questionable. At the same time, both

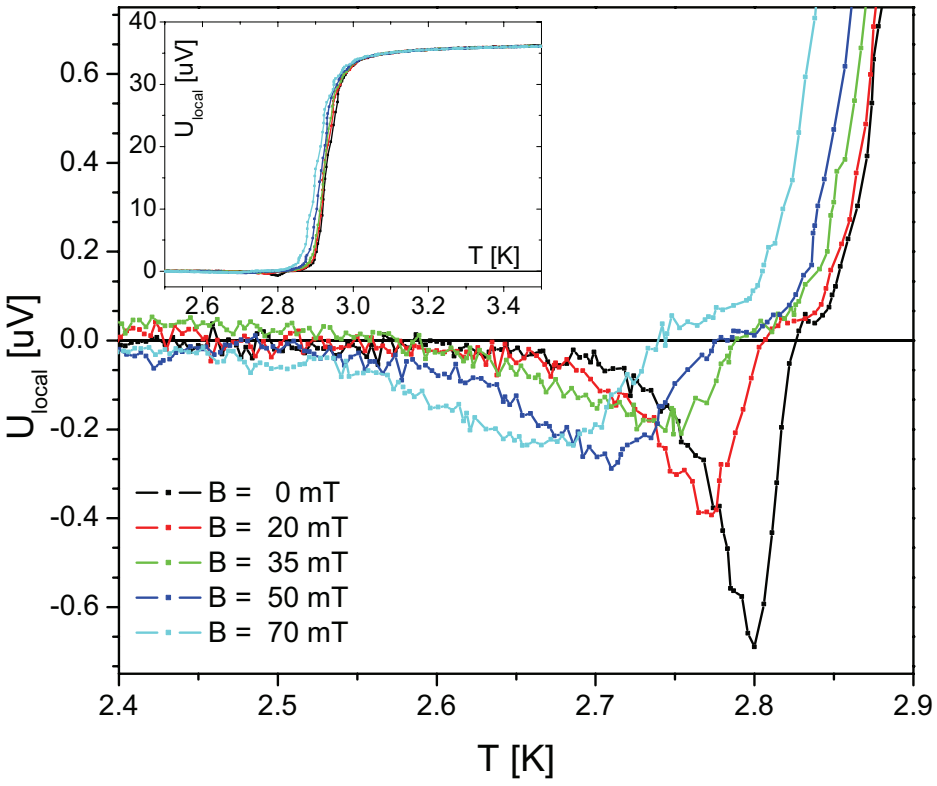

Figure 7.3: Temperature dependence of local voltage for different applied magnetic fields at a current of $I = 100\,\mathrm{nA}$. The inset shows the full curve, the main figure a zoom of the negative dips.

signals show a negative dip, which in fact shows some current dependence, yet is finite even for zero current. This corresponds to an absolute negative resistance in a small temperature window at $T \approx 2.80\,\mathrm{K}$, which is completely unexpected in this system. In contrast to our studies on the thinner samples, here no broadening of the $R(T)$-transition is observed, and the actual additional features in the nonlocal curves as well as the negative dip in the local one clearly happen below the transition, which seems to indicate rather strongly that these peculiar features cannot be explained by a BKT-transition, at least not completely. In figure 7.3, $U_{local}(T)$ for different magnetic fields is shown. Notice that the current is $I = 100\,\mathrm{nA}$, which is slightly higher than the current used for the $R(T)$-curve in chapter 5 to determine T_c. In the latter case no negative dips were observed. The minimum of the dip moves to smaller temperatures with increasing field, and although not strictly monotonically, it decreases at the same time.

The corresponding curves for the nonlocal voltage as a function of temperature (a) for

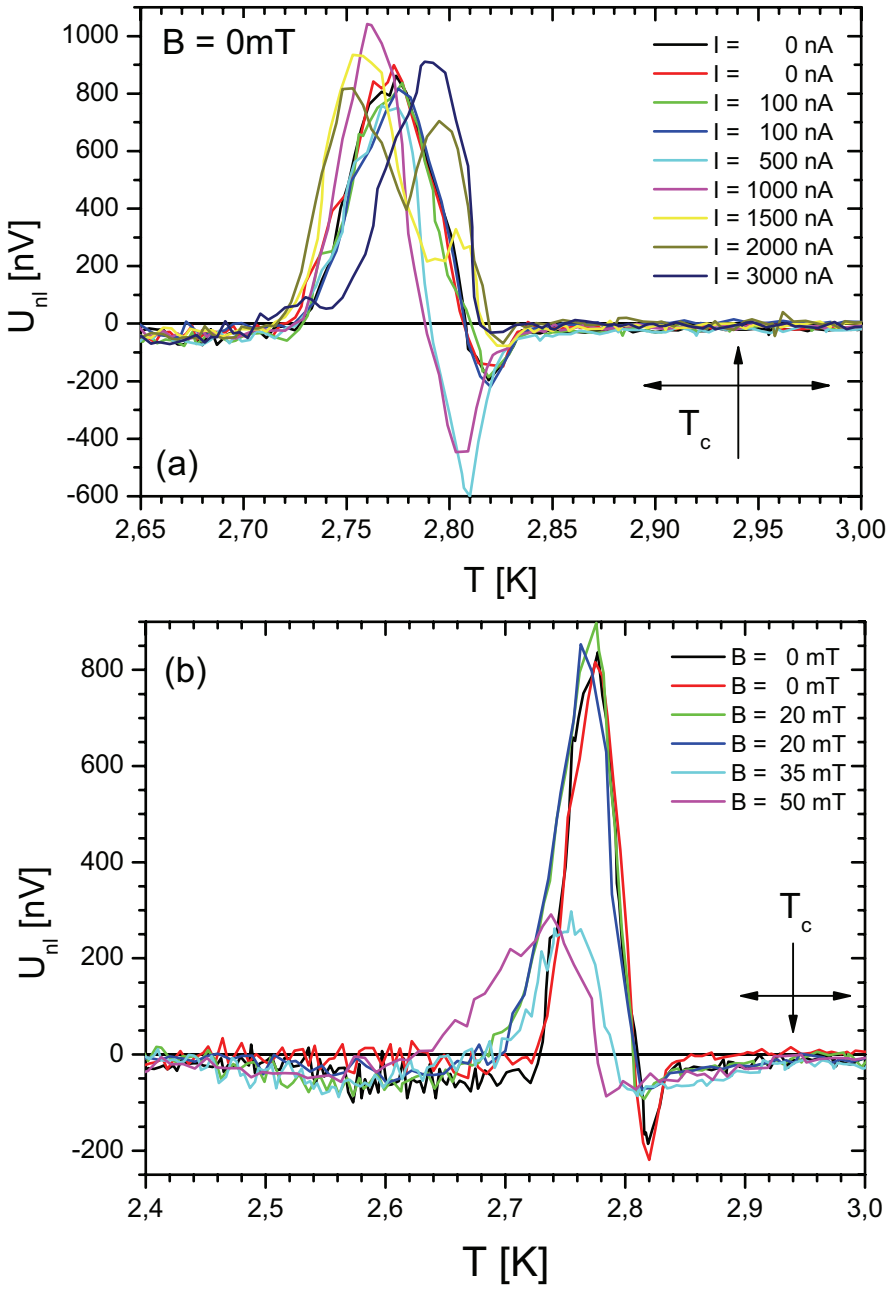

Figure 7.4: Nonlocal voltage in immediate vicinity of T_c as a function of temperature for (a) different applied currents without external field, and (b) for different magnetic fields at a current of $I = 100\,\mathrm{nA}$. Note that T_c, which together with the width of the transition is indicated by the arrows, is clearly above the negative voltage dips, thus hinting at a different mechanism than BKT.

different applied currents without fields and (b) for different fields at fixed $I = 100\,\mathrm{nA}$ are shown in figure 7.4. The curves for $I = 0$ and $100\,\mathrm{nA}$ are basically identical, whereas at currents of 500 and $1000\,\mathrm{nA}$ the negative dip is enhanced, before it decays at much higher currents. The curves for different magnetic fields show that for $B = 0$ and $20\,\mathrm{mT}$, the large positive nonlocal voltage is identical, whereas a clear negative resistance dip is only observed for zero magnetic field.
Apart from some deviations for stronger currents and higher fields, we note that the temperature above which the absolute negative resistance appears is rather independently given by roughly $T_{R<0} = 2.80\,\mathrm{K}$. This could mean that above this temperature, thermal fluctuations and thus vortex-antivortex pairs might play an important role in the creation of the voltage signal. The positive peaks on the other hand might be due to vortices that are created according to the sign of the self-field of the applied local current on both sides of the local wire and then driven through the channel, compare to figure 7.7. This would correspond to a positive nonlocal resistance and is thus in good qualitative agreement with the data.

In a second set of experiments, local and nonlocal voltage-current characteristics have been acquired in close vicinity of the transition temperature and without magnetic field as well as with small fields of several tens of mT. This is shown in figures 7.5 and 7.6. In both cases, a negative resistance appears for $T = 2.80$ and $2.82\,\mathrm{K}$, which can be suppressed by magnetic fields larger than $B = 35\,\mathrm{mT}$ in the local case and already at $B = 20\,\mathrm{mT}$ in the nonlocal case. This perfectly coincides with the critical temperature $T_{R<0} = 2.80\,\mathrm{K}$ for this effect seen in the temperature sweeps. The curves with a positive resistance are apparently hindered by pinning around zero current, since the nonlocal voltage appears only above a certain critical current value.[1]
Although we are lacking a clear and consistent picture of the above peculiar features, the findings are too persistent to be neglected: in all four different and independent measurements, $R(T)$, $R_{nl}(T)$, $U(I)$ and $U_{nl}(I)$, regions of absolute negative resistance have consistently been observed. Examples of this very unusual behavior have also been found in three-terminal devices of two-dimensional electron gases [96], where the effect can be seen as the analogue of Bernoulli's effect in a Fermi liquid, and tunnel junctions [97], where the effect can be caused by an excess population of quasiparticles in the electrode with the larger energy gap. More generally, Reimann et al. predicted theoretically that interacting Brownian particles in a symmetric periodic potential can undergo a noise-induced, nonequilibrium phase transition that leads to a ratchet response [98]. In contrast to conventional ratchet mechanisms, they showed that this can also yield a zero-bias negative conductance. More recently, current reversals in superconducting

[1] Note that all nonlocal curves have been shifted to zero for T above T_c in case of the temperature sweeps and to $U_{nl}(I = 0) = 0$ in case of the current sweeps.

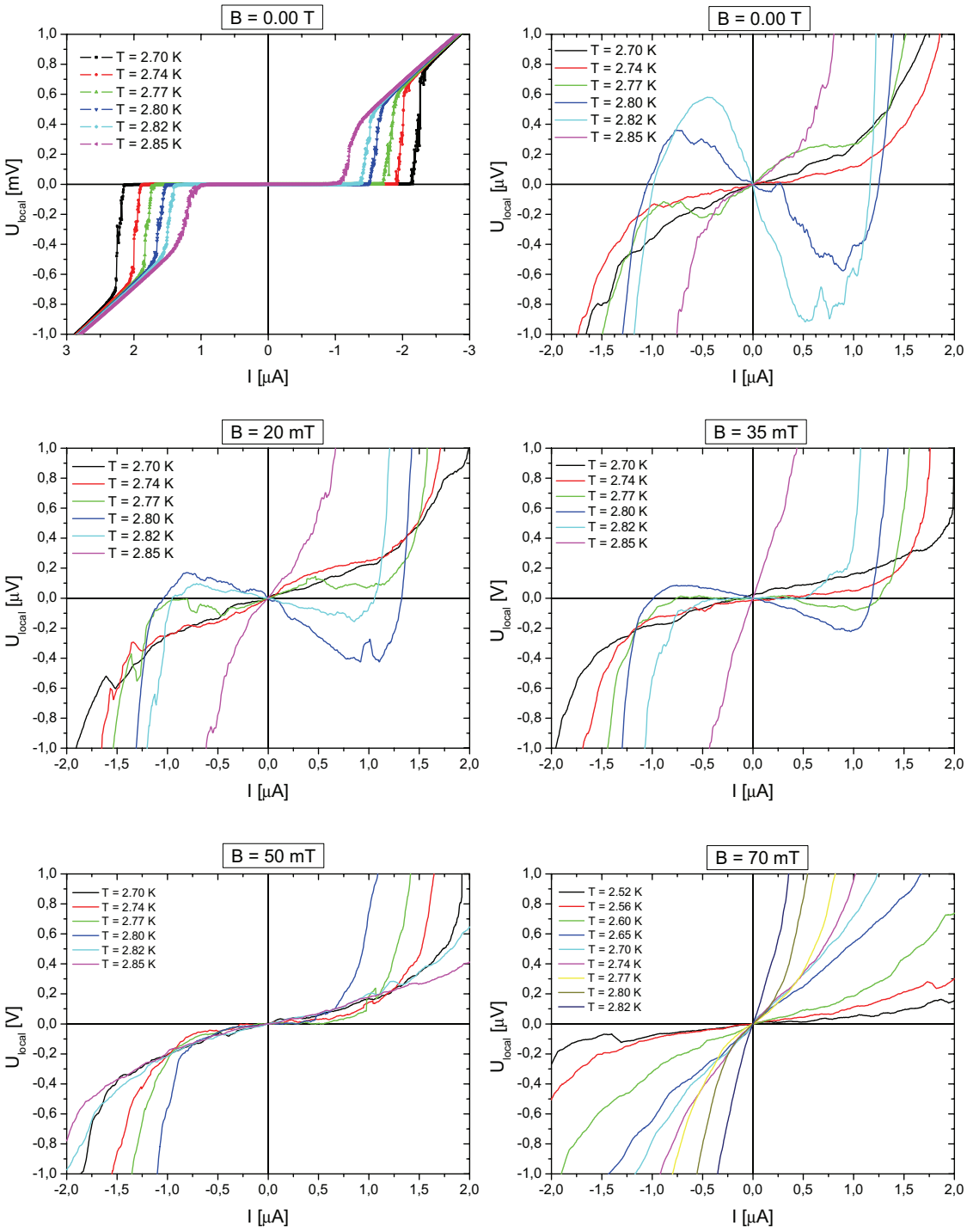

Figure 7.5: Local $V(I)$ for different temperatures, recorded at different magnetic fields in each panel. The graph in the upper left corner shows the full $V(I)$ at $B = 0$, all other panels zooms of the regions around zero current.

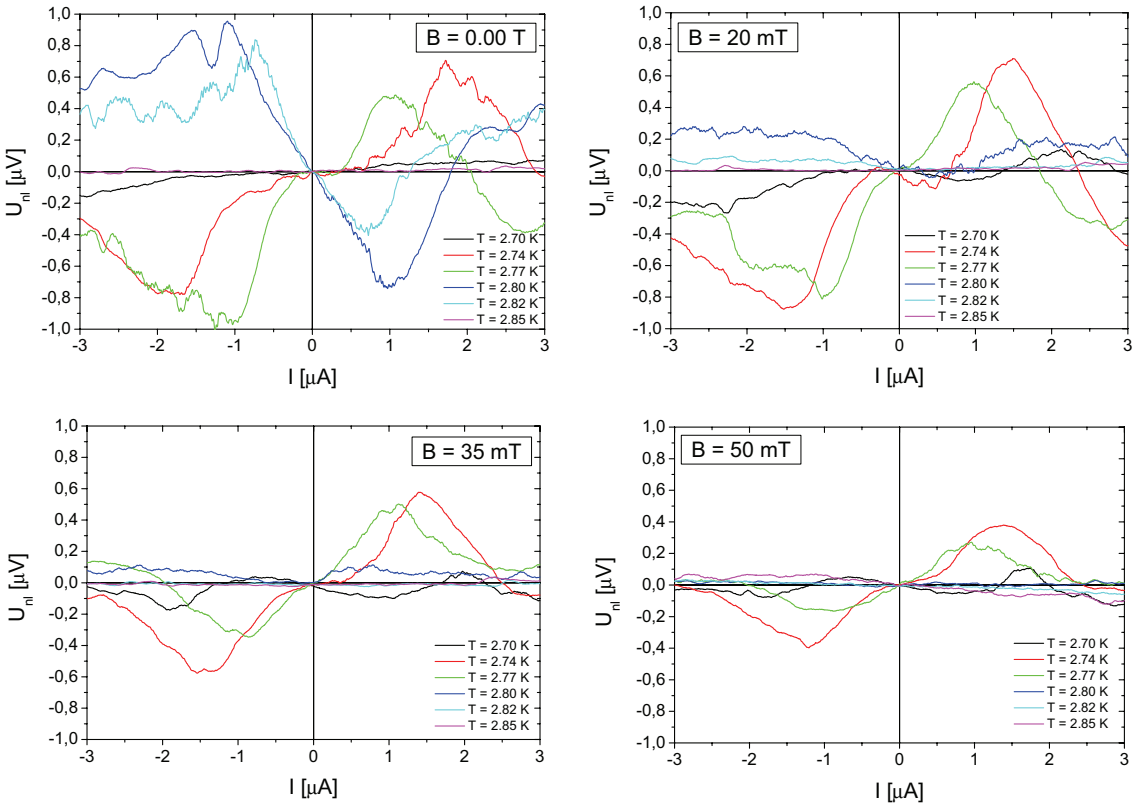

Figure 7.6: Nonlocal $V(I)$ for different temperatures, recorded at different magnetic fields in each panel.

ratchets with artificial asymmetric defects have been explained by the reconfiguration of the vortex lattice and collective motion of vortices [99]. So in principle, the absolute negative resistance observed in our measurements could originate from either an asymmetric pinning potential landscape in the material or a fluctuation induced phase transition of the type described in [98]. A definite answer however requires a deeper experimental and theoretical understanding of the described effects.

I would like to conclude the chapter by giving another, highly speculative attempt of an explanation for the negative voltage at least in case of the nonlocal signal:
For $I > 0$, corresponding to current flow from left to right in the local contacts, a measured positive voltage is in agreement with the action of the Lorentz force (and vice versa for $I < 0$): it will dissociate pairs of vortices $(\otimes)$[2] and antivortices $(\odot)$, sending the

[2]The convention used here stems from the fact that for $\vec{B} > 0$, the external magnetic field in

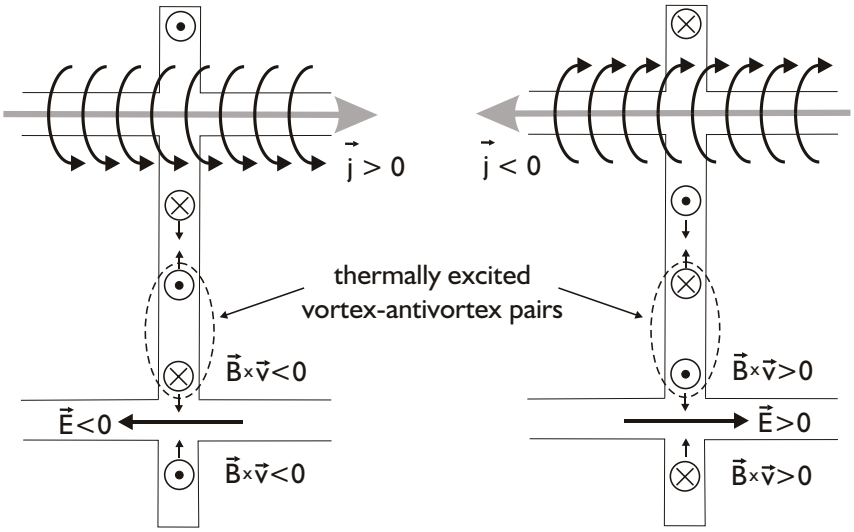

Figure 7.7: Schematic of the idea about origin of the 'negative resistance': The self-field of the current provides a current dependent asymmetry for the two current directions, that leads to preferential vortex generation of one specific helicity on both sides of the local channel. This could in principle yield a preferential 'recombination chain', with an electric field antiparallel to the applied current.

first species upwards, and the latter one downwards. To see a 'negative resistance', i.e. negative voltage for positive current (and vice versa), we need a force that changes sign with applied current. This could happen as follows: the self-field of the transport current in the local wire should lead to a preferential vortex creation below and antivortices above the local wire for $I > 0$, see figure 7.7. At finite currents, which inevitably weaken superconductivity close enough to T_c, the Lorentz force could be absent or at least small due to the local wire being 'almost' in the normal state. The remaining vortices below the local cross could then be sucked downwards to recombine with antivortices created thermally in the channel. Independently of the exact vortex-antivortex pair distribution, such a mechanism would always give the right sign for the observed voltage, since it does not matter whether vortices move downwards or antivortices move upwards: $\vec{E} = \vec{B} \times \vec{v_\phi}$. Handwaving as these arguments are, they still provide some sort of idea for the appearance of an asymmetrically negative resistance signal in the nonlocal case. The local case seems even less clear, since such simple geometric arguments cannot be constructed when vortices move perpendicular to the channel walls, while current flows along the channel. There, the finding seems completely counterintuitive.

our cryostat points upwards, but the sample is mounted upside-down.

Chapter 8

Outlook

So far, all measurements reported dealt with time-averaged signals, which stem from static methods. Another very intriguing possibility would be to monitor the vortex motion in time-resolved measurements.
First steps in that direction are briefly described in appendix A in order to avoid going all too far beyond the scope of this thesis. There, one of the simplest approaches towards this direction in the form of a time-dependent driving current was utilized, i.e. current pulses corresponding to Lorentz force ON and OFF. The findings regarding the current and field dependence of the TFTE nonlocal signal confirmed those of the static measurements well. Yet at the same time, the response of the lattice on the sub-ms time-scale was found to be still more or less instantaneous. Genuine time-resolved output would require much higher frequencies on the order of several tens of MHz, i.e. also a high cut-off frequency in the setup. Due to finite capacitances in form of the coaxial lines and filters, this constitutes a nontrivial problem.

Here, I would just like to briefly report on two possible extensions of the high-frequency measurements. The first one concerns the search for peaks in the spectrum corresponding to $f_{lattice} = v_\phi / a_\Delta$, where v_ϕ is the vortex velocity and $a_\Delta \sim \sqrt{\Phi_0 / B}$ the lattice constant (other configurations / orientations of the lattice with respect to the sample geometry imply more and different frequencies of course). Typical magnetic fields of around $1\,\mathrm{T}$ used in the case of our TFTE together with typical velocities on the order of $v_\phi = E/B = 100\,\mathrm{m/s}$ yield a frequency of the order of $f_{lattice} = 2\,\mathrm{GHz}$, which is way beyond accessibility for conventional setups. This means that one would need to (i) first of all really make sure that the resistance of the sample and the total capacitance of the setup are as small as possible, (ii) work as close to T_c as possible to minimize the effect of pinning and to allow for small magnetic fields, which would increase the lattice spacing and (iii) try to use a low vortex velocity by reducing the driving current to a minimum while still allowing for the nonlocal signal to develop. If all of this is accomplished, one

could get $f_{lattice}$ down to roughly $50\,\mathrm{MHz}$, which is more realistically measured. Still, this is a very tough experimental challenge.

The second possibility would require an extension of the sample geometry: Adding another wire, made of Al (or Ag or Nb) in close vicinity of the upper local cross as shown in figure 8.1 could in principle allow for the creation of single vortices instead of a whole lattice by a current pulse through this extra wire in absence of an external magnetic field. The current needed for the creation of a single vortex in the area of the upper cross can be estimated with the help of the Biot-Savart law: A current density $\vec{j}$ at location $\vec{r}\,'$ leads to a magnetic field at $\vec{r}$ according to

$$\vec{B}(\vec{r}) = \frac{\mu_0}{4\pi} \int_V \vec{j}(\vec{r}\,') \times \frac{\vec{r} - \vec{r}\,'}{\left|\vec{r} - \vec{r}\,'\right|^3} dV' \quad , \tag{8.1}$$

which neglects the finite cross-section of the current-carrying wire. To get a rough idea of the order of magnitude of the required current, we use the simplification

$$B(d) = \frac{\mu_0}{2\pi} \frac{I}{d} \quad , \tag{8.2}$$

which is strictly valid only for the case of an infinitely long and thin wire, and where d is the distance from the wire [100]. This yields

$$I = \frac{2\pi}{\mu_0} B d \approx \frac{2\pi}{\mu_0} \frac{\Phi_0 d}{W^2} = 166 \cdot 10^3 \, \frac{\mathrm{A}}{\mathrm{m}} \cdot d \quad . \tag{8.3}$$

Here, $\Phi_0 = BW^2$ was assumed, which is roughly the minimum field / flux required, neglecting surface barriers and pinning. Now it of course depends on the properties and dimensions of the material chosen for the extra wire whether or not the current pulse will be sufficient to create at least one vortex in the cross region. Realistically, the wire can be as close as $d \sim 200\,\mathrm{nm}$, which would require a current of $I \approx 30\,\mathrm{mA}$. In the case of Nb, which has $T_c \approx 9\,\mathrm{K}$, $B_{c2}(0) \approx 0.2\,\mathrm{T}$ and thus a critical field of about $B_c(T = 2.0\,\mathrm{K}) = 0.19\,\mathrm{T}$, the critical current estimated via Ampère's law at the same temperature for a circular wire of a radius $r = 125\,\mathrm{nm}$ yields roughly $I_c = 120\,\mathrm{mA}$ [101]. So, in principle, this is a tough but not completely unfeasible task.

Then in a time-of-flight experiment one could try to measure the time delay between the input current pulse and the output nonlocal voltage, carefully avoiding crosstalk between the measurement lines, which has been minimized by the implementation of singly filtered coaxial lines in the new sample holder design, see appendix D. The main advantage of this approach is that usually, the motion of a whole lattice of vortices is investigated, whereas here, real single vortex motion without the interactions amongst the lattice constituents should be accessible. Ultimately, this could allow for the first

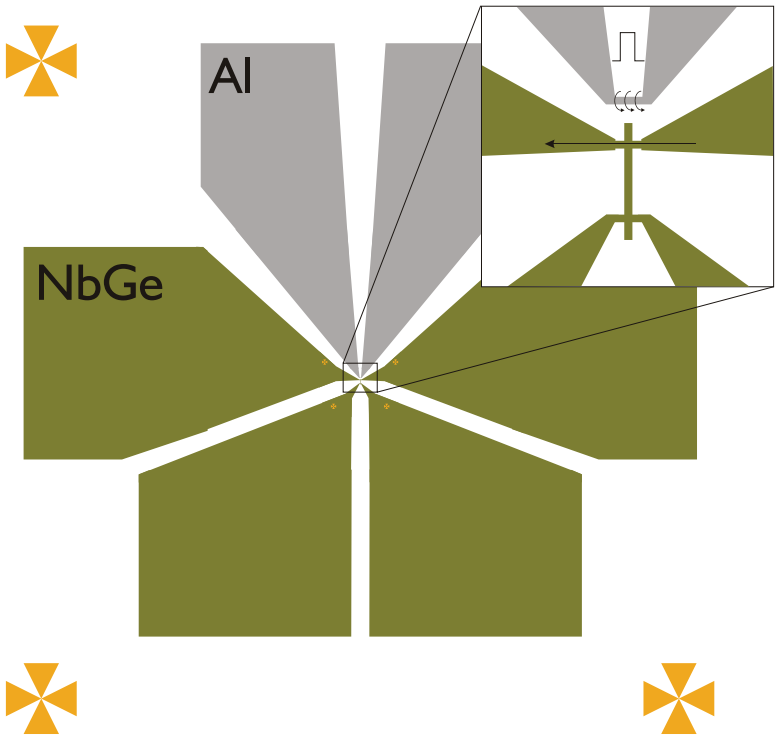

Figure 8.1: Suggestion for sample design of new pulse measurements as drawn in the electron-beam lithography software (left main figure) and a zoom of the inner structure (upper right). The TFTE structure and the size remains unchanged and is made of NbGe, but an additional wire made from Al (or Ag or Nb) is added to allow for vortex generation in the upper cross of the NbGe-structure via a current pulse in the Al wire. The vortex (or more realistically the vortex bunch) thus created will driven down the channel by the Lorentz force due to an additional static constant current flowing through the upper local wire. This should allow for time-of-flight experiments, and as a result, ultimately for a determination of the vortex mass.

experimental *determination of the inertial mass* m_ϕ *of a moving vortex* via the equation of motion

$$m_\phi \ddot{x}_\phi(t) = -\eta \dot{x}_\phi(t) \quad , \tag{8.4}$$

where $\ddot{x}_\phi(t)$ is the time-dependent deceleration and $\dot{x}_\phi(t) = v_\phi(t)$ the vortex velocity. Obviously, this corresponds to an exponentially damped motion, starting from the initial velocity $v_{\phi,0}(t = 0) = j\Phi_0$, which stems from the Lorentz force acting on the vortex in the local cross. As soon as it enters the channel, the motion is only subject to the

viscous damping force. A solution of eq. 8.4 is given by

$$\dot{x}_\phi(t) = v_{\phi,0} \exp\left(-\frac{\eta}{m_\phi} t\right) \quad . \tag{8.5}$$

The boundary conditions are $\dot{x}_\phi(t=0) = v_{\phi,0}$ and $\dot{x}_\phi(t=\tau) = v_\phi(\tau) = UW/\Phi_0$, since the measured voltage $U = \Phi_0 \cdot v_\phi(\tau)/W$, where τ is the time of flight, i.e. the time it takes the vortex to travel from the local to the nonlocal cross. Here we replaced the vortex velocity during the traveling of the flux line over the square area of the lower nonlocal cross by its average value after time τ. Solving for the mass, we arrive at

$$\frac{UW}{\Phi_0} = v_{\phi,0} \exp\left(-\frac{\eta}{m_\phi}\tau\right) \quad \Longrightarrow \quad m_\phi = -\frac{\eta\tau}{\ln\frac{UW}{v_{\phi,0}\Phi_0}} = \eta\tau \left(\ln\frac{v_{\phi,0}}{v_\phi(\tau)}\right)^{-1} \quad . \tag{8.6}$$

The above calculation is of course to be considered as a rough estimate of the equations of motion and resulting mass. Without measurements, an actual value for the resulting mass is hard to estimate, since it crucially depends on the actual decreased vortex velocity and the time of flight, both of which are completely unknown. In our first measurements at finite magnetic field and thus finite vortex density everywhere (see appendix A), the nonlocal signal could follow the excitation in form of the current pulse instantaneously. The pulse lengths used so far where on the order of $1\,\mathrm{ms}$, with a rise time of $10\,\mu\mathrm{s}$, so that it seems that the time of flight τ should be smaller than $1\,\mu\mathrm{s}$.

As a final remark, I should add that there has been a number of experiments and theoretical considerations on ballistic vortices in Josephson junction arrays (see e.g. [102,103] and for a broader overview and more references [104]). The main difference is that Josephson vortices have no normal core and thus move with very low damping. Amorphous NbGe has considerably lower damping than for example Nb, but theories predict that the mean free path (the distance vortices can travel before coming to rest due to the exponential damping) should be roughly 1 million times smaller for conventional superconductors than for the Josephson junction arrays [102]. The indication of a finite number of strong pinning sites in a-NbGe poses another problem. Overall, it thus seems that the above experiment has little chance to succeed, yet maybe one can think of improvements on sample geometry, material[1] and setup to try the impossible nevertheless.

[1] Films of a-NbGe with a thickness of 20 nm used in our previous studies for example showed nonlocal resistances on the order of $10\,\Omega$, which is 100 times larger than the signals observed in most of the current work presented here. This indicates again much smaller pinning and thus a higher vortex mobility.

Chapter 9

Conclusion

This thesis focused around the investigation of the current dependence of the Transversal Flux Transformer Effect (TFTE) by detailed measurements of nonlocal, high-sensitivity DC voltage-current characteristics.

The material chosen for the studies was amorphous $Nb_{0.7}Ge_{0.3}$, a conventional high-κ, low pinning type-II superconductor in the dirty limit. The geometric dimensions of the TFTE device have been fixed to close-to-maximum efficiency values of width and length of the channel connecting the local and nonlocal parts of the sample (as found in previous studies [11, 12]). The mesoscopic samples have been produced by magnetron sputtered thin films of NbGe, which were etched into the desired shape by using a negative resist standard electron beam lithography. The superconducting parameters found from measurements of $R(T)$ and $R(B)$ all lie in the expected range, indicating a homogeneous sample of good quality.
First, the sample was characterized extensively via local voltage-current characteristics taken at different temperatures and magnetic fields over the whole B-T-phase plane. The measurements confirmed the previously [15, 16] found clear distinction between two different mechanisms responsible for the nonlinear IV-curves, including strong flux flow instabilities (FFI) at low magnetic fields. At temperatures far below the transition temperature T_c, the electric field generated by the vortex motion leads to a suppression of the upper critical field, and thus to an effectively elevated electron temperature T^* above the bath temperature T_0, in good agreement with other experiments and theory. At temperatures close to T_c, the observed FFI are caused by the well-known mechanism of vortex-core shrinking, which leads to a decrease of the vortex motion viscosity and thus higher dissipation through faster vortex motion. Although some deviations from both previous measurements on microbridges of smaller thickness and thus lower pinning, which are better suited for this purpose, and the original Larkin-Ovchinnikov (LO) theory were observed, the overall findings still support the picture of the vortex-core shrinking

regime as the main cause behind the observed nonlinearities.

In previous studies, the nonlocal voltage generated in the TFTE was measured in magnetic field sweeps, and found to be directly proportional to the applied current, thus motivating the use of nonlocal resistance as $R_{nl} = U_{nl}/I$ as a measure of the efficiency of the effect. This can be easily interpreted and explained by a simple pressure model with the Lorentz force on the vortices due to the applied transport current as the driving mechanism, which provides for the efficient force transfer across the channel towards the remote contacts, where the nonlocal voltage is generated. Indications of deviations from this ideal behavior at high applied currents built the initial motivation and starting point of this study. In a similar fashion as for the local curves, nonlocal $U(I)$-characteristics were acquired over most of the B-T plane, too. Concentrating on the two limiting cases that allow for a clear explanation of the local curves, also the nonlocal curves revealed clearly two distinctly different regimes. While for both, temperatures close to and well below T_c, the low-current regime around $I = 0$ shows a linear response due to the Lorentz force acting on the vortices in the local wire, the nonlocal signal dramatically changes as the current is increased: For temperatures far below the transition temperature, a sudden reversal of the signal is observed, which corresponds to an abrupt sign change in the direction of vortex motion, or more precisely towards the nonlocal contacts irrespective of the direction of applied current. This is in stark contrast to the Lorentz force signal, which is expected to be asymmetric in current. Using the results of the local measurements, which yield a steep increase in the effective electron temperature around a critical electric field, the observed reversal could be nicely identified with a sharp onset of the Nernst effect due to a temperature gradient evolving between the local, out-of-equilibrium and the nonlocal, undisturbed parts of the sample. The extracted estimate for the temperature gradient yields an enormous value on the order of $1\,\mathrm{K}/\mu\mathrm{m}$, which is several orders of magnitude higher than usual numbers reported in Nernst effect measurements. Using a similar pressure model as in the case of the Lorentz force as the driving mechanism, the transport entropy associated with the thermal diffusion of the flux lines could be estimated, in good agreement with other experiments and reasonable agreement with the theory of Maki [48]. The remaining discrepancy can be attributed to the simplicity of the modeling approach and the uncertainty of the exact length scale of the temperature gradient. Additional noise measurements were carried out to estimate the expected excess heating effect in the normal state above the critical electric field. The result is that while substantial heating in the mesoscopic wires inevitably will occur at higher current densities, the effect is small in the current range relevant for the observed interplay between Lorentz force and Nernst effect.

At temperatures close to T_c, a similar, but opposite effect is observed: The nonlocal signal at high transport currents corresponds to vortex motion towards the local wire irrespective of current direction. This indicates that due to the high electric fields generated by the

vortex motion in the local wire, a spatially confined suppression of the order parameter occurs. This gap gradient between the out-of-equilibrium local wire and the undisturbed nonlocal parts of the sample leads to a current-symmetric nonlocal signal for high enough currents of opposite sign with respect to the Nernst effect. Estimates of the effective gap suppression yield values of around $40\,\%$, and the corresponding force is in good agreement with our measured values of the nonlocal voltage.
The main results is that the observed behavior in both regimes, the interplay of Lorentz force and Nernst effect on the one hand, and of the Lorentz force and a local gap suppression on the other hand, is well accounted for qualitatively by simple models.

Additionally, at temperatures in immediate vicinity of the transition temperature, signs of a Berezinskii-Kosterlitz-Thouless transition have been observed on thinner films used in previous measurements [79], although the sheet resistance is far below the critical value. The thicker samples predominantly used for this study show peculiar features slightly below T_c: in absence of magnetic field, both local and nonlocal DC voltage current characteristics clearly display absolute negative resistance in a small interval around zero current and a small temperature range immediately below T_c . At the same time, a negative voltage is also observed in both local and nonlocal measurements of $R(T)$. The temperatures at which this occurs are consistently found to be around 0.95-$0.96\,T_c$, which is clearly below the narrow superconducting transition region. Upon application of small external magnetic fields on the order of $B = 50\,\mathrm{mT}$, the effect can be suppressed. The origin of these completely unexpected features is not clear.

First steps towards time-resolved measurements of vortex motion by using current pulses to produce ON and OFF cycles of the driving force have been successful, showing good agreement with the static data. The ultimate goal of determining the inertial mass of a moving vortex is outlined in a suggestion for future investigations, yet these measurements require to overcome severe experimental difficulties to be realized.

Appendix A

Response to current pulses

In usual transport measurements, the voltage due to vortex motion stems from a time-averaged signal from many flux lines. While Clem theoretically calculated the actual shape of voltage pulses in the time domain due to individual vortices already in the early 1970's [105, 30, 106], down to the present day there exists little experimental data on the time-resolved signals. Despite the technical progress that has been made regarding both highly sensitive as well as very fast measurement equipment over the last 20 years, the experimental task still proves to be a very difficult one.

In this chapter, I will briefly summarize our own attempts to measure time-resolved signals of vortex motion dissipation using the TFTE geometry. But before doing so, let me introduce the measuring technique:

A.1 Box-car averaging

When the signals one wants to measure are very small, a very promising approach is the so-called box-car averaging, which I will briefly describe in this section.

The most simple case for investigating real-time dynamics of vortex motion is using current pulses to switch the driving force ON and OFF. The response is captured with a digital storage oscilloscope. Unfortunately, this type of measurement is not trivial to perform: the nonlocal signal is quite small (on the order of 50 nV), so it needs to be amplified, before one can look at it on an oscilloscope (maximum sensitivity: $50\ m\text{V}/12bit = 50mV/4096 = 12\mu V$). We used a two-stage amplifier, consisting of an *Arstec LI-75A* (gain 100, input noise level $1.4nV/\sqrt{Hz}$ at $1kHz$) and a *Stanford Research Systems SR560* (gain 1-50.000, in our case 5.000, input noise level $4nV/\sqrt{Hz}$ at $1kHz$) in series. This means that at a bandwidth of $1MHz$, after careful grounding

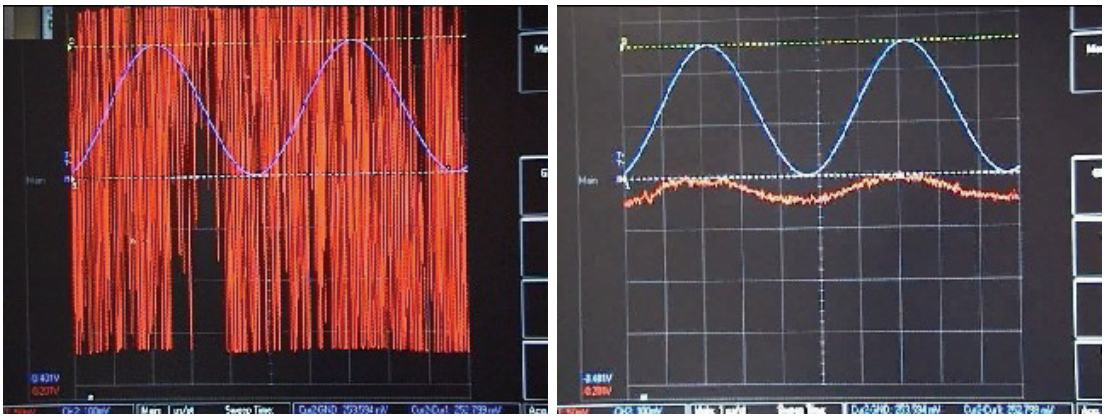

Figure A.1: Left picture*: Input signal (blue) and amplified output signal (gain 500 000, red).* Right picture*: Input signal (blue) and averaged output signal (200 000 averages, red)*

and wiring, we expect at least a noise level ΔU of

$$\Delta U = 1.4nV \times \sqrt{1MHz} \times 500000 = 700mV \ , \tag{A.1}$$

which results in a signal-to-noise ratio of $(500000 \times 50nV)/700mV = 1/30$. Additionally, the absolut value of the noise level requires to use a smaller sensitivity, $1.6V/4096 = 390\mu V$, which is then only $1/64$ of the amplified signal, or in other words, the signal is just a bit more than $1/10$ of a division on the display. One way to further improve this is averaging, since the noise is random, and thus will cancel out over time. The rate at which this happens is $1/\sqrt{N}$, where N is the number of averages. This means that in order to improve the signal-to-noise ratio to $10/1$, one would need a factor of 300, equal to 90000 averages. So the measurements are very time-consuming, especially since $U_{nl} = U_{nl}(B, T, I)$, i.e. the parameter space is rather large, even in the standard AC / DC case, before time also enters as an extra parameter in time-resolved measurements.

Figure A.1 shows an impressive example of the power of averaging to improve the signal-to-noise ratio: On the left, the oscilloscope display shows the input signal (blue, sine wave), and the output signal of the amplifiers, which is already 500 000 times larger than the original signal. Clearly, all one can see is still completely random noise. By using the internal averaging routine of the digital storage oscilloscope (*Accura 100* from *Nicolet*), the signal-to-noise ratio can be improved considerably (see right graph). The 200 000 averages taken in this example took about 30 minutes.

A.2 Magnetic field dependence

So now for the actual experimental data, which stem from very basic, 'first-step' test measurements in the time domain. Unfortunately, the sample available by the time of measurements in this case was not of the best quality: besides a low transition temperature around $T_c = 2.40\,\mathrm{K}$, the nonlocal signal observed was even smaller than usual. As mentioned in section 3.2, the design was optimized for the high-frequency measurements in terms of contact resistance and number of leads, to maximize the cut-off frequency of the whole setup: the 2-point resistances of the local (and nonlocal) leads was roughly $1\,\mathrm{k}\Omega$, which together with an estimated total capacitance $C \approx 500\,\mathrm{pF}$ due to the rf-filters (Cu-powder) and coaxial lines yields $f_{cut-off} = 1/(2\pi RC) \approx 300\,\mathrm{kHz}$. Note that the resistance value of course refers to the normal state resistance of the sample.

As already mentioned, one of the simplest implementation of a time-dependent signal is using square pulses as the current input, which creates 'Lorentz force pulses' (i.e. driving force ON and OFF), that should lead to a similar nonlocal response. The first measurements presented here were taken at two different temperatures, $t = T/Tc = 0.81$ and $t = 0.42$. The main interest was in reproducing the field and current dependence of the nonlocal signal. Figure A.2 (a) shows a static lock-in measurement ($f = 37Hz$), where the signal was measured as a function of external field at an applied current density of $j = 14\,\mathrm{MA/m^2}$. It shows the usual low-current, Lorentz force dominated behavior: as soon as the driving force is large enough to convey the motion all the way to the nonlocal contacts, the signal starts to rise with increasing field and reaches a maximum before it gradually vanishes close to the upper critical field.

Part (b) on the right hand side of the same figure shows the time-resolved pulse measurement for different magnetic fields around the observed peak in the static data. The current pulse (right scale) has a period of $4.2194\,\mathrm{ms}$, a length of $1.3\,\mathrm{ms}$, and an amplitude of $250\,\mathrm{nA}$. The rise time of the pulse edge was chosen to be $10\,\mu\mathrm{s}$ to reduce parasitic inductance peaks on the signal. The signals shown stem from a two-stage amplification of $100 \times 5\,000 = 500\,000$, and each curve consists of $180\,000$ averages, except $B = 0.85\,\mathrm{T}$, $0.90\,\mathrm{T}$ and $0.95\,\mathrm{T}$, where $150\,000$, $90\,000$ and $60\,000$ averages were used respectively. Additionally, an adjacent averaging filter with 25 points was applied, before the signal at $B = 0.3\,\mathrm{T}$, which basically was zero (as expected, compare to figure A.2 (a)) was substracted from all other curves. The reason for the latter was that all curves showed a small peak and dip at the beginning of the pulse, that is most likely not connected to vortex motion. Several tests hint at an instantaneous reply of the vortex lattice to the pulse, at least at these rather low frequencies (the approximate speed of a vortex is roughly $1\,\mathrm{m/s} = 1\,\mu\mathrm{m}/\mu\mathrm{s}$, corresponding to 1MHz rather than 1kHz).

Averages from the pulses over the pulse period have been transfused to (a) (with the

same colors as in (b)), showing a good reproduction of the peak with almost twice the amplitude of the signal in the static case. The reasons for these enlarged signals are not clear. Maybe the sudden onset of the driving force via a pulse is more effective in depinning the vortex lattice.

Summing up this part, the B-dependence of the signal is well resolved in these simple tests and roughly reproduces the static field sweep results at both temperatures. (The data at $T = 1.00\,\mathrm{K}$ shows analogous results and has been omitted here and in the next section for brevity.)

A.3 Current dependence

The second interest was to investigate the current dependence in the time domain, which is shown for several different currents in figure A.3. The inset of panel (a) shows the result of the static measurement, in this case from a numerically integrated dV/dI lock-in

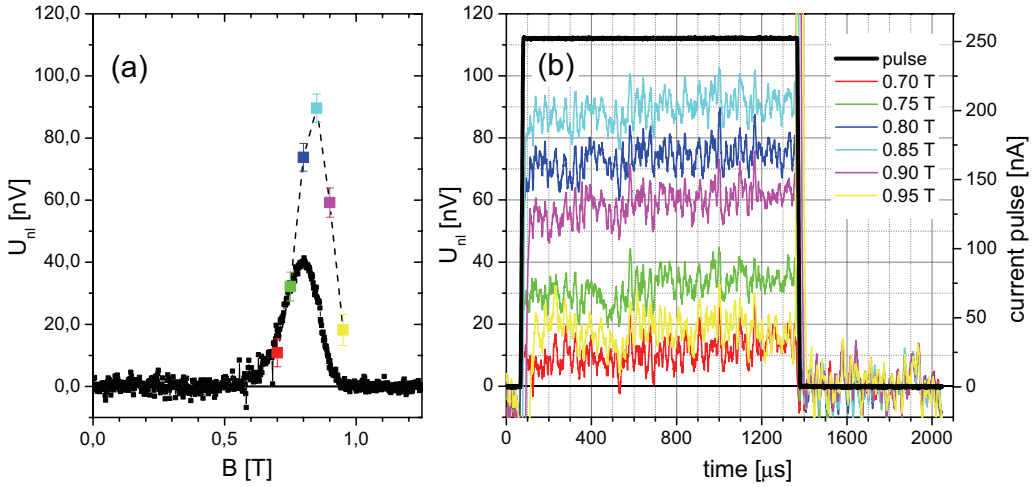

Figure A.2: Nonlocal signal at $T = 1.95\,\mathrm{K}$ (or $t = 0.81$) (a) from static lock-in measurement (AC) and (b) from pulse measurements at different magnetic fields. The averaged result of the time-resolved measurements has been copied into (a), where apart from having roughly twice the amplitude, the peak in the B-sweep is well reproduced.

signal. It features the usual low-current Lorentz response, and some less clear symmetric part for high currents. Although this most likely is also connected to a nonequilibrium effect, possibly the gap suppression and the corresponding force as described in section 6.2.2, the AC method together with the bad sample quality do not build a very solid ground for a profound analysis. Here we just note that when anticipating no or less effect of nonequilibrium in the pulse measurements, the data extracted from the time-resolved curves by averaging over the pulse period shows a more than remarkable, near perfect agreement with the asymmetric part of the static signal. This more or less 'proves' and justifies the assumption.

All in all, the above two findings on the current and field dependence of the nonlocal signal in the TFTE geometry constitute are very basic, yet also successful step towards explorations in the time domain. An outlook on more sophisticated experiments has already been given in chapter 8.

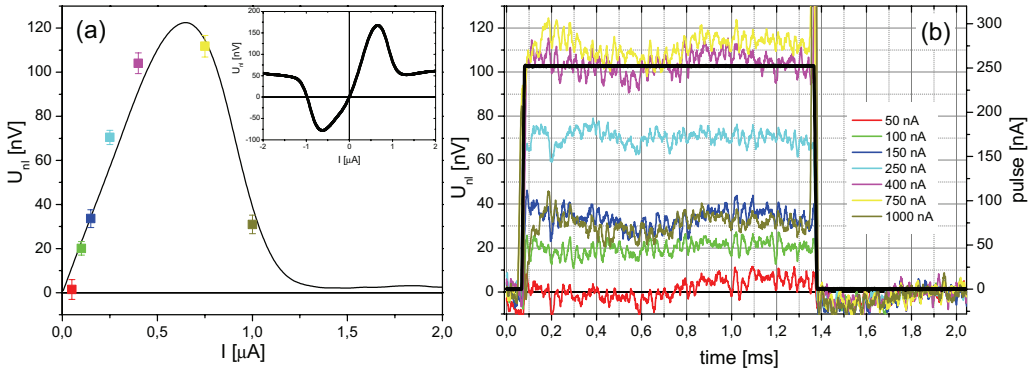

Figure A.3: Nonlocal signal at $T = 1.95\,\mathrm{K}$ (or $t = 0.81$) (a) from static differential lock-in measurement (AC) of dV/dI, which has been integrated numerically and (b) from pulse measurements at different current pulse amplitudes. In the inset of (a), the full nonlocal voltage is shown, revealing Lorentz force behavior for low currents as usual, and also a symmetric signal for high currents. Anticipating no or smaller nonequilibrium effects in the pulse measurements, the main plot only shows the asymmetric part: the agreement between the static and time-resolved measurements is astonishingly good.

Appendix B

Origin of the thermal force

In this chapter, I will give a derivation of how to calculate the thermal force leading to the Nernst effect explicitly from thermodynamic arguments.

In section 2.2.2, we saw how a temperature gradient can lead to a transverse voltage due to the thermal force $-S_\phi \mathrm{grad}\, T$. The origin of this term is by no means trivial, but can be derived in a straightforward manner from nonequilibrium thermodynamics (see e.g. [107]). Unfortunately, the latter topic is usually not covered very extensively (or sometimes not at all), neither by undergraduate nor graduate level lectures, so I decided to give the main part of the derivation in this appendix.

The central point of theories on irreversible thermodynamics is given by Onsager's theorem [108], which needs some explanation of basic principles. A great number of irreversible processes in physics as well as chemistry can be described by phenomenological equations that relate gradients of intensive variables (generalized as 'thermodynamic forces', such as a temperature or a concentration gradient) and fluxes of the associated extensive variables:

$$J_i = \sum_{k=1}^{n} L_{ik} X_k \quad , \tag{B.1}$$

where X_k denotes a thermodynamic force, J_i a flux of an extensive quantity (like heat or diffusion currents) and the L_{ik} are phenomenological coefficients: L_{ii} could be for example the thermal or electrical conductivity, whereas L_{ik} $(i \neq k)$ describes cross-coupling effects between currents of different quantities. Without going into the much more elaborate details of the theory itself, we just note the result of Onsager's considerations on statistical mechanics and microscopic reversibility (i.e. the equations of motion of microscopic particles are invariant under time reversal): he found that the matrix of the

phenomenological coefficients L_{ik} is symmetric:

$$L_{ik} = L_{ki} \quad , \tag{B.2}$$

or, in case of an externally applied magnetic field,

$$L_{ik}(\vec{B}) = L_{ki}(-\vec{B}) \quad . \tag{B.3}$$

The last equation reflects the special symmetry of the (electrodynamic) Lorentz force[1], which is given by a (cross-)product of particle velocity and magnetic field. This requires a change of sign for both quantities, if one wants to make sure that the particles reverse their trajectories under time reversal. We will make use of these so-called Onsager relations at a later stage in the following derivation of the thermal force in case of the Nernst effect.

We start off with considering the geometry of the Nernst effect shown in figure B.1 (a), where a temperature gradient in $-x$-direction causes a voltage drop in $+y$-direction in presence of a magnetic field in $+z$-direction.
The corresponding Nernst coefficient ν is defined by

$$-\frac{\partial V}{\partial y} = -\nu B \frac{\partial T}{\partial x} \quad . \tag{B.4}$$

The resulting voltage is induced by vortex motion, and thus also obeys $\vec{E} = \vec{v_\phi} \times \vec{B}/c$, or, in other words

$$\frac{\partial V}{\partial y} = v_\phi^x B/c \quad \Longrightarrow \quad v_\phi^x = -c\nu \frac{\partial T}{\partial x} \quad . \tag{B.5}$$

Since we are dealing with a-NbGe, pinning and Magnus force can be neglected, and the equation of motion reads

$$f_{\mathrm{thermal}} - \eta v_\phi^x = 0 \quad \Longleftrightarrow \quad f_{\mathrm{thermal}} = -\eta\nu c \frac{\partial T}{\partial x} \quad . \tag{B.6}$$

Next, we look at the opposite effect: the build-up of a temperature gradient (in y-direction, see B.1 (b)) due to an electrical current (in x-direction) in presence of a magnetic field (in z-direction) is called Ettingshausen effect, its coefficient ϵ being defined as

$$\epsilon = \frac{1}{B\Lambda} \frac{j_Q^y}{j_{\mathrm{electric}}^x} \quad . \tag{B.7}$$

[1]Here, the conventional Lorentz force $F_{\mathrm{L}} = q\vec{v} \times \vec{B}$ is meant, in contrast to previous chapters, where we considered the force on vortices due to supercurrents.

Here, Λ is the heat conductivity (not be confused with the penetration depth) and j_Q^y and j^x_{electric} are the heat and electrical current densities in y- and x-direction respectively. Obviously,

$$j_Q^y = T j^y_{\text{entropy}} = T n_\phi S_\phi v_\phi^y \quad , \tag{B.8}$$

where j^y_{entropy} is the entropy current, $n_\phi = B/\Phi_0$ the density of vortices, S_ϕ the entropy

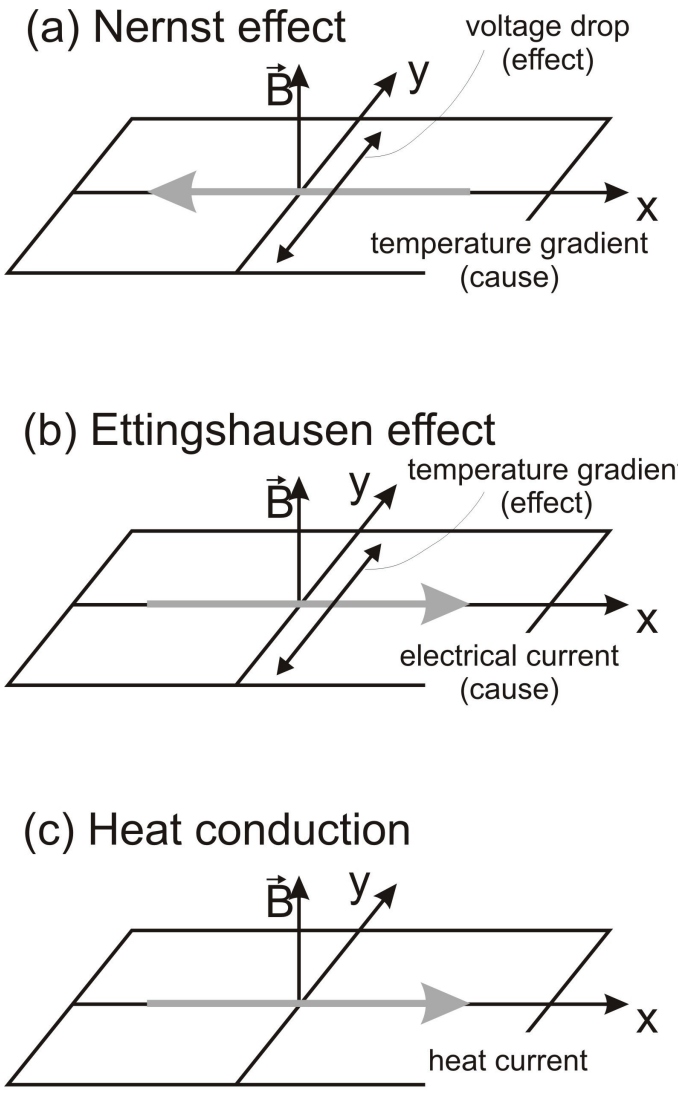

Figure B.1: Geometric situations for the effects under consideration: (a) Nernst effect, (b) Ettingshausen effect and (c) heat conduction

per vortex line and v_ϕ the vortex velocity. In this case, the Lorentz force $f_L = \frac{1}{c} j^x_{\text{electric}} \Phi_0$ drives the vortices, and accordingly, the equation of motions becomes

$$\frac{1}{c} j^x_{\text{electric}} \Phi_0 = \eta v^y_\phi \quad \Longleftrightarrow \quad j^x_{\text{electric}} = c\eta v^y_\phi / \Phi_0 \quad . \tag{B.9}$$

Inserting the last relation together with $B = n_\phi \Phi_0$ into B.7, we get

$$\epsilon = \frac{T S_\phi}{c \Lambda \eta} \quad . \tag{B.10}$$

This can be solved for η and put into B.6, yielding

$$f_{\text{thermal}} = -\frac{T S_\phi}{\epsilon \Lambda} \nu \frac{\partial T}{\partial x} \quad . \tag{B.11}$$

It remains to show that

$$T\nu = \epsilon \Lambda \quad , \tag{B.12}$$

to finally reach the result $f_{\text{thermal}} = -S_\phi \text{grad} T$.

This can be done as follows: As mentioned at the beginning of this chapter, phenomenological equations relating forces and fluxes can be used to describe many thermodynamic effects. In our case, we are dealing with simultaneous flux flow (or a particle current, represented by j_n) and heat flow (or flow of entropy, denoted by j_s), and according to equation B.1, we thus end up with the following system of equations for the x and y components of the currents involved:

$$\begin{aligned}
j^x_n &= L_{11}(-\frac{\partial \tilde{\mu}}{\partial x}) + L_{12}(-\frac{\partial T}{\partial x}) + L_{13}(-\frac{\partial \tilde{\mu}}{\partial y}) + L_{14}(-\frac{\partial T}{\partial y}) && \text{(B.13)} \\
j^x_s &= L_{21}(-\frac{\partial \tilde{\mu}}{\partial x}) + L_{22}(-\frac{\partial T}{\partial x}) + L_{23}(-\frac{\partial \tilde{\mu}}{\partial y}) + L_{24}(-\frac{\partial T}{\partial y}) && \text{(B.14)} \\
j^y_n &= L_{31}(-\frac{\partial \tilde{\mu}}{\partial x}) + L_{32}(-\frac{\partial T}{\partial x}) + L_{33}(-\frac{\partial \tilde{\mu}}{\partial y}) + L_{34}(-\frac{\partial T}{\partial y}) && \text{(B.15)} \\
j^y_s &= L_{41}(-\frac{\partial \tilde{\mu}}{\partial x}) + L_{42}(-\frac{\partial T}{\partial x}) + L_{43}(-\frac{\partial \tilde{\mu}}{\partial y}) + L_{44}(-\frac{\partial T}{\partial y}) && \text{(B.16)}
\end{aligned}$$

Note that $-e j_n = j_{\text{electric}}$ would give a usual electrical current ($e = 1.6021 \times 10^{-19}$ As), and $\tilde{\mu} = \mu - e\phi$ is the electrochemical potential, while μ and ϕ are the chemical and electric potentials respectively. If we take our system to be isotropic, the number of

coefficients reduces as follows:

$$\begin{pmatrix} L_{11} & L_{12} & L_{13} & L_{14} \\ L_{21} & L_{22} & L_{23} & L_{24} \\ L_{31} & L_{32} & L_{33} & L_{34} \\ L_{41} & L_{42} & L_{43} & L_{44} \end{pmatrix} = \begin{pmatrix} L_{11} & L_{12} & L_{13} & L_{14} \\ L_{21} & L_{22} & L_{23} & L_{24} \\ -L_{13} & -L_{14} & L_{11} & L_{12} \\ -L_{23} & -L_{24} & L_{21} & L_{22} \end{pmatrix} \quad , \tag{B.17}$$

where L_{11}, L_{12}, L_{21} and L_{22} are even and L_{13}, L_{14}, L_{23} and L_{24} are odd functions with respect to B respectively. Additionally, the Onsager relations tell us that $L_{12} = L_{21}$ and $L_{23} = L_{14}$.

A more rigorous derivation of B.13-B.16 and justification of the rather subtle details of irreversible thermodynamics can be found for example in refs. [109, 31].
We will now solve the above (already simplified) system of equations for the Nernst and the Ettingshausen coefficient and the thermal conductivity. Considering the Nernst effect once again (see figure B.1(a)), we are dealing with the following situation:

- $-\partial\tilde{\mu}/\partial y = -\nu Be(-\partial T/\partial x)$: definition of Nernst coefficient
- $j_n^x = 0$: no electrical current in x-direction
- $j_n^y = 0$: no electrical current in y-direction
- $\partial T/\partial y = 0$: no temperature-gradient in y-direction .

Using the Onsager relations, our system of equations yields

$$\begin{aligned} 0 &= -L_{11}(-\frac{\partial\tilde{\mu}}{\partial x}) - (L_{12} - L_{13}\nu Be)\frac{\partial T}{\partial x} && \text{(B.18)} \\ j_s^x &= -L_{21}(-\frac{\partial\tilde{\mu}}{\partial x}) - (L_{22} - L_{14}\nu Be)\frac{\partial T}{\partial x} && \text{(B.19)} \\ 0 &= +L_{13}(-\frac{\partial\tilde{\mu}}{\partial x}) + (L_{14} + L_{11}\nu Be)\frac{\partial T}{\partial x} && \text{(B.20)} \\ j_s^y &= +L_{14}(-\frac{\partial\tilde{\mu}}{\partial x}) + (L_{24} + L_{12}\nu Be)\frac{\partial T}{\partial x} \quad . && \text{(B.21)} \end{aligned}$$

Using B.20, we obtain

$$\frac{\partial\tilde{\mu}}{\partial x} = -\frac{1}{L_{13}}(L_{11}\nu Be + L_{14})\frac{\partial T}{\partial x} \quad , \tag{B.22}$$

which we can plug into B.18:

$$0 = \left[\frac{L_{11}}{L_{13}}(L_{11}\nu Be + L_{14}) - (L_{12} - L_{13}\nu Be)\right]\frac{\partial T}{\partial x} \quad . \tag{B.23}$$

For this equation to be generally true, the term in square brackets must be zero, or, if we solve it for ν:

$$\nu = \frac{1}{eB}\frac{L_{12}L_{13} - L_{11}L_{14}}{L_{11}^2 + L_{13}^2} \quad . \tag{B.24}$$

Next, we return to the Ettingshausen geometry (see figure B.1(b)), where we have

- $-\partial T/\partial y = -\epsilon B e j_n^x$: definition of Ettingshausen coefficient
- $j_n^y = 0$: no electrical current in y-direction
- $j_s^y = 0$: no entropy flow in y-direction
- $\partial T/\partial x = 0$: no temperature-gradient in x-direction .

Again, using this information together with the Onsager relations with our system of phenomenological equations, we get

$$\begin{aligned}
0 &= -L_{11}(-\frac{\partial\tilde{\mu}}{\partial x}) - L_{13}\frac{\partial\tilde{\mu}}{\partial y} - (L_{14} + \frac{1}{\epsilon B e})\frac{\partial T}{\partial y} && \text{(B.25)}\\
j_s^x &= -L_{21}(-\frac{\partial\tilde{\mu}}{\partial x}) - L_{14}\frac{\partial\tilde{\mu}}{\partial y} - L_{24}\frac{\partial T}{\partial y} && \text{(B.26)}\\
0 &= +L_{13}(-\frac{\partial\tilde{\mu}}{\partial x}) - L_{11}\frac{\partial\tilde{\mu}}{\partial y} - L_{12}\frac{\partial T}{\partial y} && \text{(B.27)}\\
0 &= +L_{14}(-\frac{\partial\tilde{\mu}}{\partial x}) - L_{12}\frac{\partial\tilde{\mu}}{\partial y} - L_{22}\frac{\partial T}{\partial y} \quad . && \text{(B.28)}
\end{aligned}$$

To eliminate $\partial\tilde{\mu}/\partial y$, we take $L_{14}\times$ B.27 - $L_{13}\times$ B.28:

$$0 = (L_{13}L_{12} - L_{14}11)\frac{\partial\tilde{\mu}}{\partial y} + (L_{13}L_{22} - L_{14}L_{12})\frac{\partial T}{\partial y} \quad , \tag{B.29}$$

or

$$\frac{\partial\tilde{\mu}}{\partial y} = \frac{-L_{13}L_{22} + L_{14}L_{12}}{L_{13}L_{12} - L_{14}L_{11}}\frac{\partial T}{\partial y} \quad . \tag{B.30}$$

Analogously, we take $L_{12}\times$ B.27 - $L_{11}\times$ B.28 to eliminate $\partial\tilde{\mu}/\partial x$:

$$0 = (L_{12}L_{13} - L_{11}L_{14})\frac{\partial\tilde{\mu}}{\partial x} + (L_{11}L_{22} - L_{12}^2)\frac{\partial T}{\partial y} \quad , \tag{B.31}$$

or

$$\frac{\partial\tilde{\mu}}{\partial x} = \frac{L_{11}L_{22} - L_{12}^2}{L_{11}L_{14} - L_{12}L_{13}}\frac{\partial T}{\partial y} \quad . \tag{B.32}$$

Plugging eqs. B.30 and B.32 into B.25, we have

$$0 = \left[-L_{11} \frac{L_{11}L_{22} - L_{12}^2}{L_{11}L_{14} - L_{12}L_{13}} - L_{13} \frac{-L_{13}L_{22} + L_{14}L_{12}}{L_{13}L_{12} - L_{14}L_{11}} - L_{14} - \frac{1}{\epsilon Be} \right] \frac{\partial T}{\partial y} \quad . \tag{B.33}$$

Again, this can only be true in general if the term in square brackets is zero or

$$\frac{1}{\epsilon} = (eB) \frac{L_{11}^2 L_{22} - L_{11}L_{12}^2 + L_{13}^2 L_{22} - L_{13}L_{14}L_{12} - L_{13}L_{12}L_{14} + L_{11}L_{14}^2}{L_{12}L_{13} - L_{11}L_{14}} \quad . \tag{B.34}$$

This can be rewritten using a determinant:

$$\epsilon = \frac{L_{12}L_{13} - L_{11}L_{14}}{\begin{vmatrix} L_{11} & L_{12} & L_{13} \\ L_{12} & L_{22} & L_{14} \\ -L_{13} & -L_{14} & L_{11} \end{vmatrix}} \frac{1}{eB} \tag{B.35}$$

Finally, we consider the case of heat conduction (see figure B.1(c)), which means

- $j^x_{heat} = T j^x_s = -\Lambda \partial T / \partial x$: heat current in x-direction
- $j^x_n = 0$: no electrical current in x-direction
- $j^y_n = 0$: no electrical current in y-direction
- $\partial T / \partial y = 0$: no temperature-gradient in y-direction .

Thus, we have

$$\begin{aligned} 0 &= -L_{11}(-\frac{\partial \tilde{\mu}}{\partial x}) - L_{12}\frac{\partial T}{\partial x} - L_{13}\frac{\partial \tilde{\mu}}{\partial y} && \text{(B.36)} \\ 0 &= L_{12}(-\frac{\partial \tilde{\mu}}{\partial x}) - (L_{22} - \frac{\Lambda}{T})\frac{\partial T}{\partial x} - L_{14}\frac{\partial \tilde{\mu}}{\partial y} && \text{(B.37)} \\ 0 &= L_{13}(-\frac{\partial \tilde{\mu}}{\partial x}) + L_{14}\frac{\partial T}{\partial x} - L_{11}\frac{\partial \tilde{\mu}}{\partial y} && \text{(B.38)} \\ j^y_s &= L_{14}(-\frac{\partial \tilde{\mu}}{\partial x}) + L_{24}\frac{\partial T}{\partial x} - L_{12}\frac{\partial \tilde{\mu}}{\partial y} \quad . && \text{(B.39)} \end{aligned}$$

Once more, we eliminate $\partial \tilde{\mu} / \partial y$ via $L_{13}\times$ B.36 + $L_{11}\times$ B.38:

$$\frac{\partial \tilde{\mu}}{\partial y} = -\frac{L_{13}L_{12} - L_{11}L_{14}}{L_{13}^2 + L_{11}^2}\frac{\partial T}{\partial x} \tag{B.40}$$

In the exact same manner, we take $L_{11}\times$ B.36 - $L_{13}\times$ B.38 to get

$$\frac{\partial\tilde{\mu}}{\partial x} = -\frac{L_{11}L_{12} + L_{13}L_{14}}{L_{11}^2 + L_{13}^2}\frac{\partial T}{\partial x} \tag{B.41}$$

Using eqs. B.40 and B.41 in B.37 yields

$$0 = \left[L_{12}\frac{L_{11}L_{12} + L_{13}L_{14}}{L_{11}^2 + L_{13}^2} - L_{22} + \frac{\Lambda}{T} + L_{14}\frac{L_{13}L_{12} - L11L_{14}}{L_{11}^2 + L_{13}^2}\right]\frac{\partial T}{\partial x} \quad , \tag{B.42}$$

which also again will only hold in general if the term in square brackets is zero. We finally arrive at

$$\Lambda = T\frac{L_{22}L_{11}^2 + L_{22}L_{13}^2 - L_{11}L_{12}^2 - 2L_{12}L_{13}L_{14} + L_{11}L_{14}^2}{L_{11}^2 + L_{13}^2} \tag{B.43}$$

and thus have derived expressions for all three coefficients (ν, ϵ and Λ), which we combine (B.43$\times$B.35/B.24) to obtain

$$\frac{\Lambda\epsilon}{\nu} = \frac{T}{L_{11}^2 + L_{13}^2}\frac{1}{eB}\frac{L_{12}L_{13} - L_{11}L_{14}}{(L_{12}L_{13} - L_{11}L_{14})/(eB)}(L_{11}^2 + L_{13}^2) = T \tag{B.44}$$

or

$$\nu T = \Lambda\epsilon \quad . \tag{B.45}$$

This is the Bridgman relation of irreversible thermodynamics which tells us that the thermal force is given by $f_{\mathrm{thermal}} = -S_\phi \mathrm{grad}T$.

Appendix C

Sample preparation: Recipe

- Substrate: $\mathrm{Si}/\mathrm{SiO}_2$
- Cut into 8x8 mm chips
- Standard cleaning procedure
- Deposit 40 nm (20 nm) film of a-$Nb_{0.7}Ge_{0.3}$ by magnetron sputtering
- Standard cleaning procedure
- 1^{st} EBL: writing markers for repositioning
  - spin PMMA 950k, 4%
  - 7 min. prebake @ 150 °C
  - LEO-EBL of Au markers: $280\,\mu\mathrm{C}$, Ap = 60, $I = 1100\,\mathrm{pA}$, pixel spacing 30 nm
  - development: MIBK:Prop=1:3, t=1:35 min.
  - Prop, t=1 min.
- Univex for Au-markers: Pre-sputter + 5 nm Ti + 80-100 nm Au
- Lift-off: 10 min. Acetone @ 60°C + syringe
- Cut 4x4mm pieces and clean
- 2^{nd} EBL: writing the real structure in one step (8 times per chip)
  CAUTION: keep sample in black box & under yellow light until after development to avoid accidental exposure; resist is UV sensitive!
  - ARN7500.18: 6000 rpm, acc=5, t=60 s (ca. 300nm)

  - 1 min. prebake @ 90°C
  - LEO-EBL of NbGe-structures: 60 μC, 3 alignment steps for inner structure retain alignment for leads + pads, Ap=30, I=130 pA
  - 2 min. postbake @ 90°C
  - development: AR300-47, t=85 s
  - 5-10 s $\mathrm{H_2O}$
  - blow dry CAUTIOUSLY (otherwise resist might be flaking away)

- RIE: etching step
  - 15 s DESCUM
  - 35 s + 35 s (Ar+$\mathrm{SF_6}$)

- Check $\mathrm{R_{substrate}}$ (Etched completely or short-circuit?)
- Clean off resist by use of Acetone @ 90°C + ultrasonic bath + upside down, 10 min.
- Take pictures (SEM)
- Glue sample into chip carrier
- Bonding: Al wire (25 $\mu\mathrm{m}$), standard settings, no heating of tool or stage

Appendix D

Sample holder

Some of the measurements presented in previous chapters have only been possible due to a newly built sample holder with special filtering of the coaxial lines. For this reason, and due to the fact that planning, building and assembling of the sample holder took almost all of my first year as a grad student, I will present here an overview of the features of our custom made parts of the insert.

The ^{3}He-system used is a standard *HelioxVL* insert from *Oxford Instruments* down to the 300 mK pot. Everything below the latter point (which was also custom made before) has been replaced by a newly designed holder with five major improvements:

- 8 coaxial measurement lines, each filtered separately in its own Cu-powder filter
- possibility of in-situ rotation of sample by 90° (switch from out-of-plane field to in-plane field)
- more ordered, parallel wiring
- additional Cernox thermometer next to sample
- better thermal contact (use of Ag & special-purpose Cu)

The lower part of the inset is shown in figure D.1. As already mentioned in chapter 4, the single-filtering of the coaxial lines reduces the cross-talk between the lines to a minimum. The rotation of the sample by 90° is shown in figure D.2. Due to the transmission ratio of roughly 3.7, this corresponds to approximately 330° at the top of the insert via a rotary feedthrough. The precision that can be reached is roughly 1°-2° at the bottom. The connection between the fixed and rotating parts of the sample holder is provided via two flexible Kapton foils with stripes of Cu, each featuring 10 lines and put together with their back sides, see images. An additional Cernox thermometer was

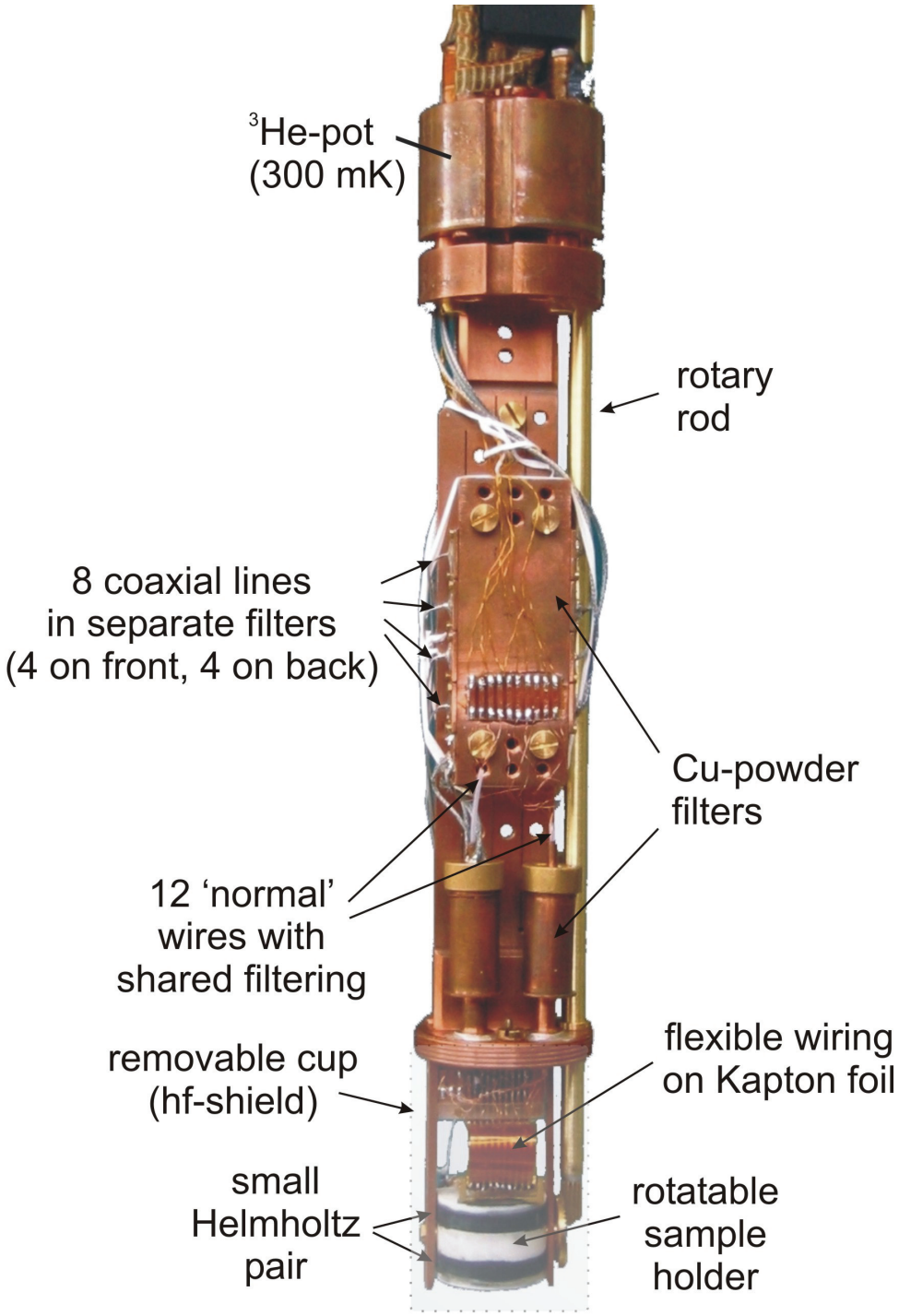

Figure D.1: Photograph of the bottom part of the insert with details of the filtering and measurements lines. Everything shown below the ^{3}He-pot has been rebuilt and custom-made during this thesis.

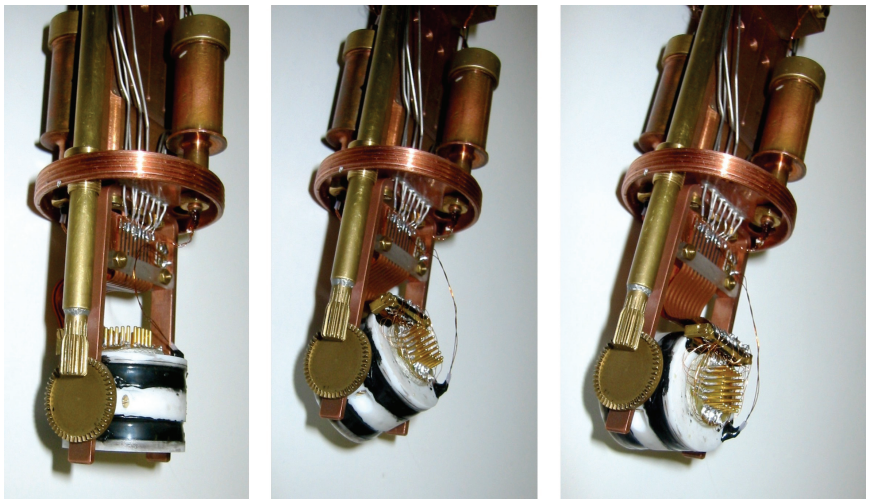

Figure D.2: The new design allows for rotation by 90° at base temperature.

mounted on the Cu-fork immediately next to the white Macor sample holder for better low temperature control / read-out. With this thermometer in place, it was found that both at temperatures below $500\,\mathrm{mK}$ and above $4.2\,\mathrm{K}$, the sample temperature deviates from the temperature of the ^{3}He-pot by up to 10%.

Figure D.3 shows the performance of a Cu-powder filter in the frequency response: below the MHz-regime, no damping is observed, whereas above roughly $1\,\mathrm{GHz}$, it stays well below $-40dBm$. This is sufficient for most purposes and provides excellent shielding of for example noise due to cell phone radiation.

Details of the production and the performance of these filters can be found in [81, 82]. Here I would just like to shortly mention how the wire that goes inside the filter is wound: In order to maximize the wire length while minimizing its inductance, alternating layers of clockwise and counter-clockwise windings of the geometry shown in figure D.4 are accumulated, yielding the shown result. This final wire structure is then put into a hollow Cu-cylinder, filled with Cu-powder (grain size $\sim 50\,\mu\mathrm{m}$), and sealed with GE varnish, which holds in place a Cu-disc as top cover for electrical shielding. The filters produced for our sample holder showed inductance values between 15 and $20\,\mu\mathrm{H}$ and capacitances of around $50\,\mathrm{pF}$ at a wire length of $1.5\,\mathrm{m}$ (diameter $80\,\mu\mathrm{m}$, resistance $R \approx 6\,\Omega$).

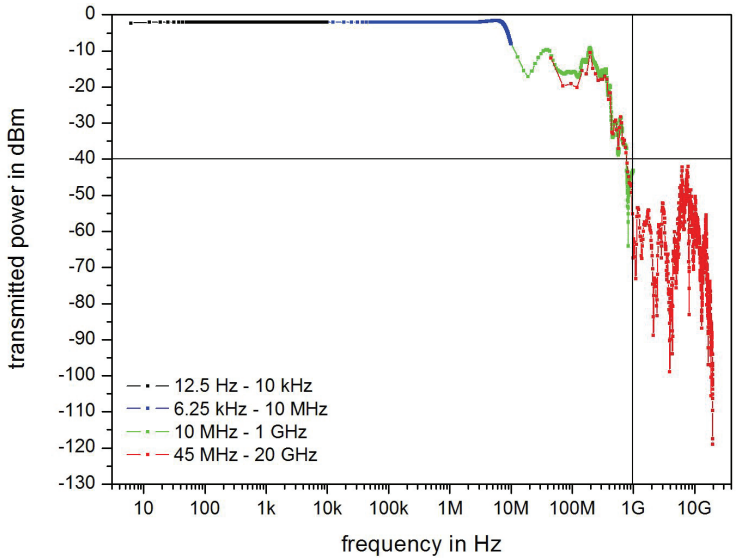

Figure D.3: Performance of Cu-powder filters as mounted in the system. As a rule of thumb, the damping above 1 GHz *is at least* 40 dBm.

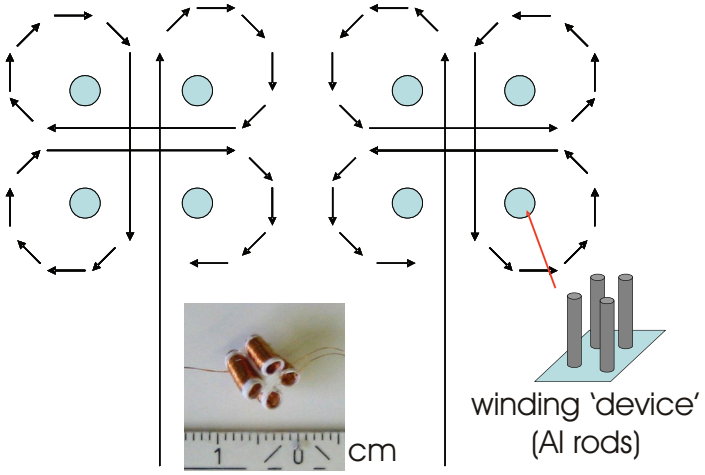

Figure D.4: Winding scheme of the wire used for the Cu-powder filters: In order to minimze the inductance of the 'coil' and at the same time maximizing the wire length in a given volume, alternating 'layers' of clockwise and counter-clockwise windings of the shown geometry around Al rods are produced. The final result is shown in the small image in the center at the bottom.

Bibliography

[1] H. Kammerlingh-Onnes. Proc. Roy. Acad. Amsterdam, 11:168 (1908).

[2] H. Kammerlingh-Onnes. Comm. Leiden, 120b (1911).

[3] A. A. Abrikosov. 'On the magnetic properties of superconductors of the second type.' JETP Lett., 5:1174 (1957).

[4] I. Giaever. 'Magnetic Coupling Between Two Adjacent Type-II Superconductors.' Phys. Rev. Lett., 15 (21):825 (1965).

[5] H. Safar, E. Rodriguez, F. de la Cruz, P. L. Gammel, L. F. Schneemeyer and D. J. Bishop. 'Observation of two-dimensional vortices in $Bi_2Sr_2CaCu_2O_x$.' Phys. Rev. B, 46 (21):14238 (1992).

[6] D. A. Huse and S. N. Majumdar. 'Nonlocal resistivity in the vortex liquid regime of type-II superconductors.' Phys. Rev. Lett., 71 (15):2473 (1993).

[7] H. Safar, P. L. Gammel, D. A. Huse, S. N. Majumdar, L. F. Schneemeyer, D. J. Bishop, D. López, G. Nieva and F. de la Cruz. 'Observation of a nonlocal conductivity in the mixed state of $YBa_2Cu_3O_{7-\delta}$: Experimental evidence for a vortex line liquid.' Phys. Rev. Lett., 72 (8):1272 (1994).

[8] C.-Y. Mou, R. Wortis, A. T. Dorsey and D. A. Huse. 'Nonlocal conductivity in type-ii superconductors.' Phys. Rev. B, 51 (10):6575 (1995).

[9] R. Wortis and D. A. Huse. 'Nonlocal conductivity in the vortex-liquid regime of a two-dimensional superconductor.' Phys. Rev. B, 54 (17):12413 (1996).

[10] D. López, W. K. Kwok, H. Safar, R. J. Olsson, A. M. Petrean, L. Paulius and G. W. Crabtree. 'Spatially resolved dynamic correlation in the vortex state of high temperature superconductors.' Phys. Rev. Lett., 82 (6):1277 (1999).

[11] I. V. Grigorieva, A. K. Geim, S. V. Dubonos, K. S. Novoselov, D. Y. Vodolazov, F. M. Peeters, P. H. Kes and M. Hesselberth. 'Long-range nonlocal flow of vortices in narrow superconducting channels.' Phys. Rev. Lett., 92 (23):237001 (2004).

[12] A. Helzel, I. Kokanović, D. Babić, L. V. Litvin, F. Rohlfing, F. Otto, C. Sürgers and C. Strunk. 'Nonlocal vortex motion in mesoscopic amorphous $Nb_{0.7}Ge_{0.3}$ structures.' Phys. Rev. B, 74 (22):220510 (2006).

[13] A. Helzel. *Vortexdynamik in amorphem NbGe* (Universität Regensburg, Diplomarbeit, 2006).

[14] A. I. Larkin and Y. N. Ovchinnikov. 'Vortex motion in superconductors.' In 'Nonequilibrium Superconductivity,' (D. N. Lengenberg and A. I. Larkin, eds.), 493 (North Holland, Amsterdam, 1986).

[15] D. Babić, J. Bentner, C. Sürgers and C. Strunk. 'Flux-flow instabilities in amorphous $Nb_{0.7}Ge_{0.3}$ microbridges.' Phys. Rev. B, 69 (9):092510 (2004).

[16] D. Babić. 'Amorphous Nb-Ge thin films as a model system for experiments on fundamental properties of vortex transport.' In 'New Frontiers in Superconductivity Research,' (B. S. Martins, ed.), 107–143 (Nova Science Publishers, Hauppauge NY, 2006).

[17] M. Tinkham. *Introduction to superconductivity* (McGraw-Hill, New York, 1975).

[18] W. Buckel and R. Kleiner. *Supraleitung: Grundlagen und Anwendungen* (Wiley-VCH, Weinheim, 2004).

[19] R. Huebener. *Magnetic Flux Structures in Superconductors* (Springer, New York, 2001).

[20] F. London and H. London. 'The electromagnetic equations of the supraconductor.' Proc. Roy. Soc. A, 149 (866):71 (1935).

[21] C. J. Gorter and H. Casimir. 'On supraconductivity I.' Physica, 1:306 (1934).

[22] A. B. Pippard. 'An experimental and theoretical study of the relation between magnetic field and current in a superconductor.' Proc. Roy. Soc. A, 216 (1127):547 (1953).

[23] B. S. Deaver and W. M. Fairbank. 'Experimental evidence for quantized flux in superconducting cylinders.' Phys. Rev. Lett., 7 (2):43 (1961).

[24] R. Doll and M. Näbauer. 'Experimental proof of magnetic flux quantization in a superconducting ring.' Phys. Rev. Lett., 7 (2):51 (1961).

[25] W. A. Little and R. D. Parks. 'Observation of quantum periodicity in the transition temperature of a superconducting cylinder.' Phys. Rev. Lett., 9 (1):9 (1962).

[26] L. P. Gor'kov. 'Microscopic derivation of the Ginzburg-Landau equations in the theory of superconductivity.' JETP Lett., 9:1364 (1959).

[27] J. Bardeen, L. N. Cooper and J. R. Schrieffer. 'Theory of superconductivity.' Phys. Rev., 108 (5):1175 (1957).

[28] M. Füchsle. *Mikro-Hall-Magnetometrie an SNS-Heterostrukturen* (Universität Regensburg, Diplomarbeit, 2006).

[29] A. Sergeev, M. Reizer and V. Mitin. 'Thermomagnetic effects in vortex liquid: Which carriers transfer thermal energy?' arXiv.org:0807.0450 (2008).

[30] J. Clem. 'Flux-flow noise in superconductors.' Phys. Rep., 75 (1):1 (1981).

[31] A. M. Campbell and J. E. Evetts. 'Flux vortices and transport currents in type II superconductors.' Adv. Phys., 50 (8):1249 (2001).

[32] R. P. Huebener. 'Dynamics of magnetic flux structures in superconductors.' Physics Reports, 13 (4):143 (1974).

[33] R. P. Huebener and A. Seher. 'Nernst Effect and Flux Flow in Superconductors. II. Lead Films.' Phys. Rev., 181 (2):710 (1969).

[34] V. A. Rowe and R. P. Huebener. 'Nernst Effect and Flux Flow in Superconductors. III. Films of Tin and Indium.' Phys. Rev., 185 (2):666 (1969).

[35] F. A. Otter and P. R. Solomon. 'Thermal Forces on Vortices and Entropy Transport by Vortex Flow in Type-II Superconductors.' Phys. Rev. Lett., 16 (16):681 (1966).

[36] P. R. Solomon and F. A. Otter. 'Thermomagnetic effects in superconductors.' Phys. Rev., 164 (2):608 (1967).

[37] J. Lowell, J. S. Munoz and J. B. Sousa. 'Thermally induced voltages in the mixed state of type II superconductors.' Phys. Lett. A, 24 (7):376 (1967).

[38] J. Lowell, J. S. Munoz and J. B. Sousa. 'Transport Properties of Dirty Type-II Superconductors in High Magnetic Fields.' Phys. Rev., 183 (2):497 (1969).

[39] R. P. Huebener and A. Seher. 'Nernst Effect and Flux Flow in Superconductors. I. Niobium.' Phys. Rev., 181 (2):701 (1969).

[40] M. Zeh, H.-C. Ri, F. Kober, R. P. Huebener, A. V. Ustinov, J. Mannhart, R. Gross and A. Gupta. 'Nernst effect in superconducting Y-Ba-Cu-O.' Phys. Rev. Lett., 64 (26):3195 (1990).

[41] S. J. Hagen, C. J. Lobb, R. L. Greene, M. G. Forrester and J. Talvacchio. 'Flux-flow Nernst effect in epitaxial $YBa_2Cu_3O_7$.' Phys. Rev. B, 42 (10):6777 (1990).

[42] H. Lengfellner, A. Schnellbögl, J. Betz, W. Prettl and K. F. Renk. 'Nernst effect by laser-pulse heating in Tl-Ba-Ca-Cu-O superconducting thin films.' Phys. Rev. B, 42 (10):6264 (1990).

[43] H. Lengfellner and A. Schnellbögl. 'Nernst effect in high-T_c superconductors.' Physica C, 174:373 (1991).

[44] F. Kober, H.-C. Ri, R. Gross, D. Koelle, R. P. Huebener and A. Gupta. 'Transport entropy in $YBa_2Cu_3O_7$: A comparison between epitaxial and polycrystalline thin films.' Phys. Rev. B, 44 (21):11951 (1991).

[45] H.-C. Ri, F. Kober, A. Beck, L. Alff, R. Gross and R. P. Huebener. 'Thermal diffusion of quasiparticles and vortices in the mixed state of high-temperature superconductors.' Phys. Rev. B, 47 (18):12312 (1993).

[46] H.-C. Ri, R. Gross, F. Gollnik, A. Beck, R. P. Huebener, P. Wagner and H. Adrian. 'Nernst, Seebeck, and Hall effects in the mixed state of $YBa_2Cu_3O_{7-\delta}$ and $Bi_2Sr_2CaCu_2O_{8+x}$ thin films: A comparative study.' Phys. Rev. B, 50 (5):3312 (1994).

[47] Z. A. Xu, N. P. Ong, Y. Wang, T. Kakeshita and S. Uchida. 'Vortex-like excitations and the onset of superconducting phase fluctuation in underdoped $La_{2-x}Sr_xCuO_4$.' Nature, 406:486 (2000).

[48] K. Maki. 'Motion of the Vortex Lattice in a Dirty Type II Superconductor.' J. Low Temp. Phys., 1 (1):45 (1969).

[49] C. Caroli and K. Maki. 'Motion of the Vortex Structure in Type-II Superconductors in High Magnetic Field.' Phys. Rev., 164 (2):591 (1967).

[50] C.-R. Hu. 'Heat-current operator and transport entropy of vortices in type-II superconductors.' Phys. Rev. B, 13 (11):4780 (1976).

[51] C.-R. Hu. 'Transport entropy of vortices in superconductors with paramagnetic impurities.' Phys. Rev. B, 14 (11):4834 (1976).

[52] N. B. Kopnin. 'Thermodynamics of vortex motion in type II superconductors.' J. Low Temp. Phys., 93 (1-2):117 (1993).

[53] M. J. Stephen and J. Bardeen. 'Viscosity of Type-II Superconductors.' Phys. Rev. Lett., 14 (4):112 (1965).

[54] M. Tinkham. 'Viscous Flow of Flux in Type-II Superconductors.' Phys. Rev. Lett., 13 (26):804 (1964).

[55] M. N. Kunchur. 'Unstable flux flow due to heated electrons in superconducting films.' Phys. Rev. Lett., 89 (13):137005 (2002).

[56] L. E. Musienko, I. M. Dmitrenko and V. G. Volotskaya. JETP Lett., 31:567 (1980).

[57] W. Klein, R. P. Huebener, S. Gauss and J. Parisi. 'Nonlinearity in the flux-flow behavior of thin-film superconductors.' J. Low Temp. Phys., 61 (5-6):413 (1985).

[58] A. Bezuglyj and V. Shklovskij. 'Effect of self-heating on flux flow instability in a superconductor near T_c.' Physica C, 202:234 (1992).

[59] M. Kanskar, M. N. Wybourne and K. Johnson. 'Energy loss from hot electrons in a metal film.' Phys. Rev. B, 47 (20):13769 (1993).

[60] A. L. Fetter and P. C. Hohenberg. 'Theory of type-II superconductors.' In 'Superconductivity,' (R. D. Parks, ed.), 817–923 (Marcel Dekker, New York, 1969).

[61] L. J. van der Pauw. 'A Method of Measuring the Resistivity and Hall Coefficient on Lamellae and Arbitrary Shape.' Philips Tech. Rev., 20:220 (1958).

[62] T. Matsuda, K. Harada, H. Kasai, O. Kamimura and A. Tonomura. 'Observation of Dynamic Interaction of Vortices with Pinning Centers by Lorentz Microscopy.' Science, 271 (5254):1393 (1996).

[63] J. M. Kosterlitz and D. J. Thouless. 'Ordering, metastability and phase transitions in two-dimensional systems.' Journal of Physics C: Solid State Physics, 6 (7):1181 (1973).

[64] M. R. Beasley, J. E. Mooij and T. P. Orlando. 'Possibility of Vortex-Antivortex Pair Dissociation in Two-Dimensional Superconductors.' Phys. Rev. Lett., 42 (17):1165 (1979).

[65] D. S. Fisher. 'Flux-lattice melting in thin-film superconductors.' Phys. Rev. B, 22 (3):1190 (1980).

[66] B. I. Halperin and D. R. Nelson. 'Resistive Transition in Superconducting Films.' J. Low Temp. Phys., 36 (5/6):599 (1979).

[67] A. P. Young. 'Melting and the vector Coulomb gas in two dimensions.' Phys. Rev. B, 19 (4):1855 (1979).

[68] V. L. Berezinskii. 'Violation of long range order in one-dimensional and two-dimensional systems with a continuous symmetry group. I. Classical systems.' JETP Letters, 32:493 (1971).

[69] V. L. Berezinskii. 'Destruction of long-range order in one-dimensional and two-dimensional systems with a continuous symmetry group. II. Quantum systems.' JETP Letters, 34:610 (1971).

[70] U. Gasser, G. Maret and P. Keim. 'Das Schmelzen zweidimensionaler Kristalle. Phasenübergänge durch topologische Defekte.' Physik in unserer Zeit, 39 (1):36 (2008).

[71] K. Epstein, A. M. Goldman and A. M. Kadin. 'Renormalization effects near the vortex-unbinding transition of two-dimensional superconductors.' Phys. Rev. B, 26 (7):3950 (1982).

[72] A. M. Kadin, K. Epstein and A. M. Goldman. 'Renormalization and the Kosterlitz-Thouless transition in a two-dimensional superconductor.' Phys. Rev. B, 27 (11):6691 (1983).

[73] D. J. Resnick, J. C. Garland, J. T. Boyd, S. Shoemaker and R. S. Newrock. 'Kosterlitz-thouless transition in proximity-coupled superconducting arrays.' Phys. Rev. Lett., 47 (21):1542 (1981).

[74] V. M. Svistunov, A. I. D'jachenko and V. Y. Tarenkov. 'Resistive vortices and two-dimensional transition in aluminum films.' J. Low Temp. Phys., 57:619 (1984).

[75] J. Mooij. 'Two-dimensional transition in superconducting films.' In 'Percolation, Localization and Superconductivity,' (A. M. Goldman and S. A. Wolf, eds.), 325–370 (Plenum Press, New York, 1984).

[76] K. E. Gray, J. Brorson and P. A. Bancelt. 'Resistance Measurements and Vortex Fluctuations in Two-Dimensional Superconducting Films.' J. Low Temp. Phys, 59 (5+6):529 (1985).

[77] P. Berghuis, A. L. F. van der Slot and P. H. Kes. 'Dislocation-mediated vortex-lattice melting in thin films of a-Nb_3Ge.' Phys. Rev. Lett., 65 (20):2583 (1990).

[78] E. H. Brandt. 'On the shear modulus of the flux line lattice.' Phys. Stat. Solidi B, 77 (2):551 (1976).

[79] M. Frisch. *Nichtlokaler Vortex-Transport in NbGe* (Universität Regensburg, Diplomarbeit, 2006).

[80] P. H. Kes and C. C. Tsuei. 'Two-dimensional collective flux pinning, defects, and structural relaxation in amorphous superconducting films.' Phys. Rev. B, 28 (9):5126 (1983).

[81] J. M. Martinis, M. H. Devoret and J. Clarke. 'Experimental tests for the quantum behavior of a macroscopic degree of freedom: The phase difference across a Josephson junction.' Phys. Rev. B, 35 (10):4682 (1987).

[82] K. Bladh, D. Gunnarsson, E. Hürfeld, S. Devi, C. Kristoffersson, B. S. lander, S. Pehrson, T. Claeson, P. Delsing and M. Taslakov. 'Comparison of cryogenic filters for use in single electronics experiments.' Review of Scientific Instruments, 74 (3):1323 (2003).

[83] A. V. Samoilov, M. Konczykowski, N. C. Yeh, S. Berry and C. C. Tsuei. 'Electric-Field-Induced Electronic Instability in Amorphous Mo_3Si Superconducting Films.' Phys. Rev. Lett., 75 (22):4118 (1995).

[84] N. R. Werthamer, E. Helfand and P. C. Hohenberg. 'Temperature and Purity Dependence of the Superconducting Critical Field, H_{c2}. III. Electron Spin and Spin-Orbit Effects.' Phys. Rev., 147 (1):295 (1966).

[85] L. Coffey, K. A. Muttalib and K. Levin. 'Theory of upper critical fields in highly disordered superconductors: Localization effects.' Phys. Rev. Lett., 52 (9):783 (1984).

[86] P. Berghuis and P. H. Kes. 'Two-dimensional collective pinning and vortex-lattice melting in a-$Nb_{1-x}Ge_x$ films.' Phys. Rev. B, 47 (1):262 (1993).

[87] D. Babić. private communication (2008).

[88] D. Babić, J. Bentner, C. Sürgers and C. Strunk. '1/f flux flow noise due to a coexistence of qualitatively different vortex states.' Physical Review B (Condensed Matter and Materials Physics), 76 (13):134515 (2007).

[89] F. Vidal. 'Low-Frequency ac Measurements of the Entropy Flux Associated with the Moving Vortex Lines in a Low-κ Type-II Superconductor.' Phys. Rev. B, 8 (5):1982 (1973).

[90] C. Strunk, M. Henny, C. Schönenberger, G. Neuttiens and C. Van Haesendonck. 'Size Dependent Thermopower in Mesoscopic AuFe Wires.' Phys. Rev. Lett., 81 (14):2982 (1998).

[91] M. Henny, S. Oberholzer, C. Strunk and C. Schönenberger. '1/3-shot-noise suppression in diffusive nanowires.' Phys. Rev. B, 59 (4):2871 (1999).

[92] D. Babić, T. Nussbaumer, C. Strunk, C. Schönenberger and C. Sürgers. 'Vortex motion noise in micrometer-sized thin films of the amorphous $Nb_{0.7}Ge_{0.3}$ weak-pinning superconductor.' Phys. Rev. B, 66 (1):014537 (2002).

[93] D. Vodolazov. private communication, unpublished (2008).

[94] A. I. Larkin and Y. N. Ovchinnikov. Sov. Phys. JETP, 51:960 (1976).

[95] A. Yazdani, W. R. White, M. R. Hahn, M. Gabay, M. R. Beasley and A. Kapitulnik. 'Observation of Kosterlitz-Thouless-type melting of the disordered vortex lattice in thin films of a-MoGe.' Phys. Rev. Lett., 70 (4):505 (1993).

[96] I. I. Kaya and K. Eberl. 'Absolute negative resistance induced by directional electron-electron scattering in a two-dimensional electron gas.' Physical Review Letters, 98 (18):186801 (2007).

[97] M. Gerschenzon and M. Falei. 'Absolute negative resistance of a tunnel junction contact between superconductors with a nonequilibrium quasiparticle distribution function.' JETP Letters, 44 (11):682 (1986).

[98] P. Reimann, R. Kawai, C. V. den Broeck and P. Hänggi. 'Coupled brownian motors: Anomalous hysteresis and zero-bias negative conductance.' EPL (Europhysics Letters), 45 (5):545 (1999).

[99] L. Dinis, E. M. González, J. V. Anguita, J. M. R. Parrondo and J. L. Vicent. 'Lattice effects and current reversal in superconducting ratchets.' New Journal of Physics, 9 (10):366 (2007).

[100] http://de.wikipedia.org/wiki/Biot-Savart-Gesetz (2008).

[101] C. R. Nave. http://hyperphysics.phy-astr.gsu.edu/Hbase/hframe.html (2008).

[102] T. P. Orlando, J. E. Mooij and H. S. J. van der Zant. 'Phenomenological model of vortex dynamics in arrays of josephson junctions.' Phys. Rev. B, 43 (13):10218 (1991).

[103] H. S. J. van der Zant, F. C. Fritschy, T. P. Orlando and J. E. Mooij. 'Ballistic vortices in josephson-junction arrays.' EPL (Europhysics Letters), 18 (4):343 (1992).

[104] R. Fazio and H. van der Zant. 'Quantum phase transitions and vortex dynamics in superconducting networks.' Physics Reports, 355 (4):235 (2001).

[105] J. R. Clem. 'Theory of flux-flow noise voltage in superconductors.' Phys. Rev. B, 1 (5):2140 (1970).

[106] J. Clem. 'Time-dependent voltage generated by flux motion across a superconducting strip.' J. Low Temp. Phys., 42 (3-4):363 (1981).

[107] S. de Groot. *Thermodynamik irreversibler Prozesse* (Bibliographisches Institut, Mannheim, 1960).

[108] L. Onsager. 'Reciprocal Relations in Irreversible Processes. I.' Phys. Rev., 37 (4):405 (1931).

[109] J. Evetts, A. Campbell and D. Dew-Hughes. 'Forces on flux vortices in an arbitrary configuration.' J. Phys. C, 1 (3):715 (1968).

Acknowledgement

All of this would never have been accomplished without the help of many people. In particular, I would like to thank

- My advisor, Prof. Dr. Christoph Strunk (Regensburg), who let me work on a very interesting subject, and kept me motivated even in hard times. He was supportive at any point of the project and took the time to discuss things even when in fact he almost had none to do so.

- Prof. Dr. Rudolf Gross (WMI Garching), who agreed to act as a referee for my thesis without hesitation and showed great interest in the topic.

- Dr. Ante Bilušić (Regensburg, Split), who was involved in most of the experimental work for almost two years. Amongst the many things that I learned from him are most notably patience and endurance.

- Dr. Dinko Babić (Zagreb), who is one of the leading experts on vortex dynamics in low pinning materials, and has never stopped to help me in analyzing my data. Besides, he always gave invaluable tips for how to measure things.

- Dr. Denis Vodolazov (Nizhny Novgorod), who developed the theoretical model for the force due to the gap gradient, and helped us greatly in understanding all of the nonlocal data.

- Dr. Christoph Sürgers (Karlsruhe), who has been fabricating the NbGe samples of superb quality for several years.

- Dr. Ondrej Vavra (Regensburg) for the idea to use a negative e-beam resist, and his assistance with the successful implementation of the new recipe.

- Andreas Helzel (Regensburg) and Martin Frisch (Regensburg), who I had the pleasure to work with and who both got great results during their diploma theses on the same subject.

- Prof. Dr. Weiss (Regensburg), who let me use his clean room facilities and other infrastructure at the chair.
- Emiliano for the brilliant idea of performing additional noise measurements. I still consider you a very good friend. (And of course I thank you for many vivid discussions about physics and life in general.)
- Ben, Tom, Markus, Matthias and Andi for carefully reading my manuscript.
- Wilfried, Ondrej and Matthias for sharing the office with me, where besides many helpful technical discussions one could always have a good laugh.
- Dominik, David, Franziska, Leonid, Sung-Ho, Elsa, Lorenz L., Lorenz H., Wolfgang and Marcus for being (or having been) more than good colleagues.
- The former group members Johannes, Andreas and Bernhard for many useful hints.
- Our technicians Martin Furthmeier, Thomas Haller and Michael Weigl as well as the cleanroom engineers Cornelia Deinhart and Uli Gürster for assistance on many technical details.
- Our secretaries Claudia Rahm and Elke Haushalter, who make sure that everyday life runs like clockwork at our chair.
- Christian Haimerl, Thomas Solleder, Karl Weigert and Lothar Rother from the He-station, who always succeeded in wresting enough Helium from our ancient liquefier to have our cryostats working.
- The mechanical and electronics workshop for brilliant pieces of work that helped me finish my job.
- The whole chair of Prof. Weiss for help and the nice atmosphere.
- The Graduiertenkolleg 638 for financial support.
- My close friends Mark, Andi R., Björn, Andi D. and Wanni for excusing my lack of leisure time to hang out with them and for not forgetting about me during these times.
- My brother Stephan and his wife Conny, and my whole family for keeping me grounded.
- My parents for their constant and never-ending support during all of my life.
- My girl-friend Susanne for being my biggest support and my best friend at the same time: You mean the world to me!